

QUANTUM LIQUIDS AND QUANTUM CRYSTALS

Phase separation curve of dilute ${}^3\text{He}$ – ${}^4\text{He}$ hcp solid solutions

A. N. Gan'shin, V. N. Grigor'ev, V. A. Maïdanov, N. F. Omelaenko, A. A. Penzev, E. Ya. Rudavskii,* and A. S. Rybalko

B. Verkin Institute for Low Temperature Physics and Engineering, National Academy of Sciences of Ukraine, pr. Lenina 47, 61164 Kharkov, Ukraine

(Submitted April 11, 2000; revised June 7, 2000)

Fiz. Nizk. Temp. **26**, 1175–1181 (December 2000)

A method is proposed for constructing the separation phase diagram of ${}^3\text{He}$ – ${}^4\text{He}$ solid solutions on the basis of precision measurement of the pressure jump due to phase separation at constant volume. The technique is implemented on high-quantity samples of the solid solutions, making it possible to obtain reliable and reproducible experimental data with no appreciable manifestation of hysteresis effects. The line of phase separation constructed from the experimental data is compared with the results of various theoretical approaches describing phase separation in solid solutions of helium isotopic mixtures. It is found that good agreement with experiment is observed only for the Edwards–Balibar model, which is an extension of the theory of regular solutions to take into account the differences of the crystal structures (hcp and bcc) of the phases existing in the system. © 2000 American Institute of Physics. [S1063-777X(00)00112-2]

1. INTRODUCTION

The first information about the line of phase separation of ${}^3\text{He}$ – ${}^4\text{He}$ solid solutions was obtained back in 1962, simultaneously with the observation of this first-order phase transition in measurements of the specific heat.¹ The phase separation temperature T_{ps} was determined from the anomaly in the temperature dependence of the specific heat during a rapid first cooling of the samples, and it was shown that the values obtained can be described in the model of regular solutions, according to which

$$T_{ps} = \frac{2T_c(1-2x)}{\ln(1/x-1)}, \quad (1)$$

where x is the concentration of the mixture, and T_c is the critical temperature, which corresponds to the maximum of the separation curve and depends on the pressure P ; a processing of the data of Ref. 1 gave the value 0.38 K at $P = 34.1$ bar. As compared with the theory of ideal solutions, the model of regular solutions additionally takes into account the excess thermodynamic functions; in particular, the excess free energy has a simple quadratic dependence on the concentration:

$$g_e = A(P)x(1-x), \quad (2)$$

where the coefficient A is independent of temperature and is a function of the pressure in the crystal. In this approximation the line of phase separation is symmetric about the concentration $x = 0.5$.

Another approach to the theoretical description of the line of phase separation was proposed by Mullin.² It is based on the application of the Nosanov variational quantum theory,³ which was developed for pure isotopes of solid he-

lium, to their isotopic mixture. In that approach the excess free energy of a mixture is a more complicated function of concentration than in (2):

$$g_e = A(P)x(1-x)(1+\varepsilon x). \quad (3)$$

The eccentricity ε appears in expression (3) on account of the peculiarities of helium quantum crystals: the large difference of the molar volumes of ${}^3\text{He}$ and ${}^4\text{He}$, which is due to the appreciable difference of the amplitudes of the zero-point motion. This circumstance gives rise to an asymmetry of the line of phase separation. No analytical expression describing the phase diagram was given in Ref. 2.

The asymmetry of the phase diagram predicted in Ref. 2 was confirmed experimentally in Ref. 4 in the concentration region $x < 0.3$, for which no data was given in Ref. 1. Here the values of T_{ps} were determined as the inflection point on the temperature dependence of the change in pressure in the crystal due to phase separation as the sample was cooled. The asymmetry of the line of phase separation was subsequently confirmed for other concentrations as well, in Ref. 5 from measurements of the thermal conductivity of the crystal and in Ref. 6 from pressure measurements.

However, it was later established by careful x-ray studies^{7,8} that the eccentricity in (3) is extremely small, having a value $\varepsilon \approx 0 \pm 0.01$, and the asymmetry observed previously in the experiments of Refs. 4–6 was attributed to the presence of hysteresis in the determination of T_{ps} , the non-equilibrium nature of the samples, and the influence of the bcc–hcp transition.

This last circumstance was investigated in detail by Edwards and Balibar,⁹ who did a numerical calculation of the separation phase diagram on the assumption that $\varepsilon = 0$ but with allowance for the different crystallographic struc-

tures of pure ^3He and ^4He (bcc and hcp, respectively) at low pressures. The results of the calculation explained the observed asymmetry of the phase diagram, agreed well with the existing experimental data, and have been subsequently confirmed by new experiments in the left-hand part of the phase diagram.^{10,11}

In the present paper we again address the question of the equilibrium phase diagram for the phase separation of ^3He – ^4He solid solutions, for the following reasons:

1. Considerable progress has been achieved recently in the growth of high-quality crystals of two-phase ^3He – ^4He solid solutions, making for reliable and reproducible results in the study of the kinetics of the phase transition.¹² Therefore it is advisable to study the thermodynamic properties of the system on the same samples.

2. Here we propose a new method of constructing the phase diagram, based on precision measurement of the pressure in the crystal.

3. The pressure and concentration of the mixture studied were chosen such that the initial sample had a hcp structure, while the phases formed after separation had different structures — a concentrated bcc phase and a dilute hcp phase. This circumstance makes it possible to elucidate the influence of the different crystal structures of the separated phases on the phase diagram and to compare the results with those obtained in the framework of the Edwards–Balibar approach and the Mullin model.

2. SALIENT FEATURES OF THE EXPERIMENT

We investigated a mixture with an initial ^3He concentration in the gas phase $x_0 = 2.05\%$, from which a crystalline sample was grown by the capillary-blocking method, so that all of the experiments were done at constant volume. The sample was a disk 9 mm in diameter and 1.5 mm thick, and the pressure in the crystal prior to the start of phase separation was 35.98 bar. The thermal relaxation time of the sample under the conditions of this experiment was estimated¹² to be short, several tens of seconds, so it was not necessary to use a sinter heat exchanger in the measurement cell.

Phase separation was registered by measuring the pressure in the crystal by means of a capacitive sensor, which provided a resolution in the pressure measurements of ± 8 Pa.^{12,13} The excess pressure due to the phase transition depends on the concentration of the initial mixture² and is given by

$$\Delta P = \frac{0.4x(1-x)}{V_\chi}, \quad (4)$$

where V and χ are the molar volume and compressibility of the solid solution. Unlike Refs. 4 and 6, where the phase diagram was also constructed on the basis of pressure measurements, in the present study the phase separation temperature was determined not from the kink on the temperature dependence of the pressure but from the pressure jump ΔP (see the next Section), a procedure that improved the accuracy and reliability of the measurements and made it possible, using a single sample, to obtain information about the separation phase diagram over the whole range of concentrations less than x_0 .

To prepare high-quality samples, the grown crystal was annealed near the melting temperature and then subjected to repeated temperature cycling below the phase separation temperature (this process is described in detail in Ref. 12). Analysis of the experimental data showed that after several cycles of growth and dissolution of the bcc inclusions in the hcp matrix, the quality of the crystal improved substantially, as is evidenced by the practically total absence of hysteresis effects (the values of the phase separation temperatures of the initial sample on cooling and heating agreed to within 10 mK), the decrease of the pressure in the sample, the small and reproducible values obtained for the time constants for the growth and dissolution of the inclusions, and the proportionality of ΔP to the corresponding change in the concentration of the solution in accordance with Eq. (4). The ΔP measurements were made under stepped cooling and heating of the crystal, during which, as was shown in Ref. 12, the time dependence of ΔP within each step can be approximated by an exponential function. The primary experimental data pertaining to the characteristic values of ΔP are presented in Fig. 19 of Ref. 12.

3. METHOD OF CONSTRUCTING THE PHASE DIAGRAM

A relation between the experimentally measurable pressure jump ΔP upon phase separation and the corresponding concentration of the solution (at some fixed temperature) can be obtained from the conservation laws. If the solid solution under study occupied a volume v_0 prior to the phase transition, and after phase separation formed a concentrated phase of volume v_c and a dilute phase of volume v_d , then the volume conservation law gives

$$v_0 = v_c + v_d. \quad (5)$$

The law of conservation of the amounts of ^3He and ^4He can be written in the form of a lever rule:

$$\frac{v_c}{v_d} = \frac{x_0 - x_d}{x_c - x_0}, \quad (6)$$

$$v_c + v_d = v_0, \quad (7)$$

where χ_0 , x_d , and x_c are the concentrations of the initial, dilute, and concentrated phases, respectively, and where the numbers of moles of the substance contained in each of these phases, ν_0 , ν_d , and ν_c , are expressed in terms of the corresponding molar volumes V_0 , V_d , and V_c as

$$\nu_0 = \frac{v_0}{V_0}, \quad \nu_d = \frac{v_d}{V_d}, \quad \nu_c = \frac{v_c}{V_c}. \quad (8)$$

If the pressure in the solution is P and becomes $P + \Delta P$ after phase separation, then to a first approximation we can write

$$V_0(P + \Delta P) \approx V_0(P) + \frac{\partial V_0}{\partial P} \Delta P = V_0(1 - \chi \Delta P), \quad (9)$$

where $\chi = -(1/V_0)(\partial V_0/\partial P)$ is the compressibility of the crystal. After substituting expression (9) into (5) with (6)–(8) taken into account, we obtain

$$\Delta P = \frac{1}{\chi} - \frac{x_0(V_c - V_d) + (x_c V_d - x_d V_c)}{\chi V_0(x_c - x_d)}. \quad (10)$$

We now use the known relation between the molar volumes of a solution and the pure components,²

$$\begin{aligned}
 V_0 &= x_0 V_3 + (1 - x_0) V_4 - \alpha x_0 (1 - x_0); \\
 V_c &= x_c V_3 + (1 - x_c) V_4 - \alpha x_c (1 - x_c); \\
 V_d &= x_d V_3 + (1 - x_d) V_4 - \alpha x_d (1 - x_d),
 \end{aligned}
 \tag{11}$$

where the parameter $\alpha = 0.4 \text{ cm}^3/\text{mole}$. Then, substituting (11) into (10) and taking into account that at a fixed temperature $x_c + x_d = 1$, we get

$$\Delta P = \frac{\alpha(x_0 - x_c)(x_0 - x_d)}{\chi V_0}.
 \tag{12}$$

The maximum pressure jump ΔP_{max} will be observed, according to (12), as the solid solution is cooled from the phase separation temperature T_{ps} to $T = 0$. In this case $x_c = 1$ and $x_d = 0$, and

$$\Delta P_{\text{max}} = \frac{\alpha}{\chi V_0} (x_0 - 1) x_0.
 \tag{13}$$

If we denote the pressure jump corresponding to a temperature T in the phase separation region as $\Delta P(T)$, then the relative change of the pressure has the form

$$\frac{\Delta P}{\Delta P_{\text{max}}} = \frac{(x_0 - x_c)}{(x_0 - 1)} \frac{(x_0 - x_d)}{x_0} \approx \frac{x_0 - x_d}{x_0},
 \tag{14}$$

i.e., in deriving (14) we have made use of the assumption that $x_c \approx 1$ at sufficiently low temperatures. Thus formula (14) can be used to describe the left branch of the line of phase separation in terms of the experimentally observed pressure jumps:

$$x_d(T) = x_0 \frac{\Delta P_{\text{max}} - \Delta P(T)}{\Delta P_{\text{max}}}.
 \tag{15}$$

The values of $\Delta P(T)$ were measured as the sample was cooled in the two-phase region in small temperature steps (10–15 mK) down to the lowest temperature used, at which the formation and growth of the new phase was practically complete. An analysis showed that the pressure jump corresponding to the change in temperature from the onset of phase separation to $\sim 80\text{--}90 \text{ mK}$ can be taken as equal to ΔP_{max} .

Analogous measurements of ΔP were also done during a stepped heating of the two-phase crystal, making it possible to compare the corresponding points on the phase diagram obtained during cooling and heating of the sample. Figure 1 shows the typical variation of the pressure during one step, as the inclusions grow and dissolve. Although the time constants characterizing the two processes are very different,¹² the pressure change ΔP of the two-phase crystal, as can be seen in Fig. 1, turns out to be practically identical on cooling and heating.

This means that the quality of the crystals was such that hysteresis effects are essentially absent. Since the working formula (15) for constructing the phase diagram has only one temperature-dependent parameter, $\Delta P(T)$, the points obtained during heating and cooling have turned out to be close to each other. According to estimates, the absolute error in

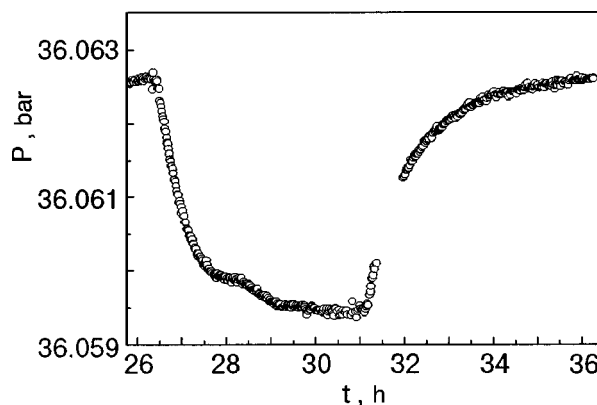


FIG. 1. Typical kinetics of the change in pressure in the sample over the course of a single temperature step. The two-phase crystal is initially heated from 81 mK (^3He concentration $x = 0.001\%$) to 108 mK ($x = 0.02\%$ ^3He) and then cooled from 108 to 81 mK.

the determination of the concentration was not more than $\pm 10^3\%$ at low ^3He concentrations, and $\pm 10^{-2}\%$ at high concentrations.

4. LINE OF PHASE SEPARATION. COMPARISON WITH THEORY

The values obtained for the equilibrium concentrations of the dilute phase on the line of phase separation are presented as a function of the temperature of the crystal in Fig. 2 and Table I. It is seen from Fig. 2 that the experimental data obtained on cooling and heating agree with each other within the experimental error limits at temperatures below $\approx 150 \text{ mK}$, which, as we have said, attests to the absence of hysteresis effects.

At temperatures above $\approx 150 \text{ mK}$ the difference between the data obtained on cooling and heating is greater than the errors in the determination of the concentration and measurement of the temperature. As is seen in Fig. 2, the points obtained on cooling lie systematically lower than the points

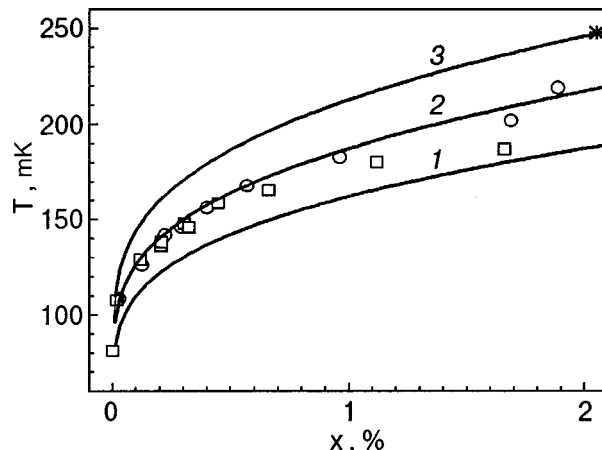


FIG. 2. Left branch of the line of phase separation of $^3\text{He}\text{--}^4\text{He}$ solid solutions (molar volume $20.27 \text{ cm}^3/\text{mole}$). Experimental points: on cooling of the crystal (\square), on heating (\circ), on overheating of the crystal in the single-phase region (*). The solid curves are calculated according to: 1 — the standard theory of regular solutions (Eq. (1)); 2 — the Edwards–Balibar theory⁹ (Eq. (19)); 3 — the Mullin theory.²

TABLE I. Concentration and phase separation temperature of dilute solid solutions of ^3He in ^4He at a molar volume of $20.27 \text{ cm}^3/\text{mole}$.

Temperature, mK	Concentration, % ^3He
Cooling	
187.0	1.66
180.3	1.42
165.4	0.66
158.5	0.45
147.8	0.31
136.1	0.21
145.8	0.324
137.9	0.208
128.8	0.119
107.7	0.018
81.1	0.001
Heating	
108.4	0.028
126.2	0.125
141.8	0.224
145.8	0.29
156.3	0.40
167.7	0.57
182.9	0.96
201.9	1.69
218.9	1.88
247.8	2.05

obtained on heating. This circumstance is a consequence of the growing role of hysteresis effects as the temperature approaches the phase transition.

The absence of hysteresis effects at low temperatures can apparently be attributed to an increase in the rate of relaxation to equilibrium as the temperature (concentration) is lowered, on account of the increase in the diffusion coefficient of the ^3He quasiparticles, the value of which in dilute solid solutions of ^3He in ^4He is governed by impurity-impurity scattering and is inversely proportional to the concentration.¹⁴

We also note that our results agree with the analogous data obtained in a previous study¹⁰ of the line of phase separation by the NMR method, within the experimental error limits stated in Ref. 10.

The experimental data presented can be compared with various models describing the phase diagrams of solutions. Curve 1 in Fig. 2 shows the phase separation temperature T_{ps} calculated in the theory of regular solutions, according to formula (1). As we mentioned in the Introduction, in such an approach the phase diagram should be symmetric about $x=0.5$ and, as follows from Fig. 2, is in poor agreement with the experimental results.

The use of the model of regular solutions to describe solid solutions of helium isotopes, as was proposed by Edwards and Balibar,⁹ requires the introduction of corrections to take into account the difference of the crystal structures of the phases (here hcp and bcc). Then the excess free energy g_e as given by expression (2) should be supplemented with another term to take into account the differences in the structure of the crystal: for solid solutions having the hcp structure

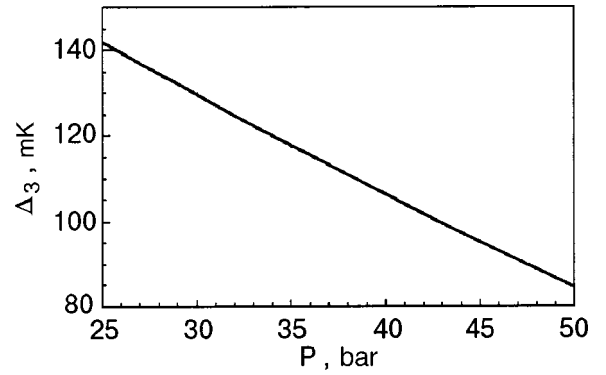


FIG. 3. Difference between the free energies of the metastable hcp and stable bcc phases of ^3He as a function of pressure.

$$g_e^h = A^h x(1-x) + x\Delta_3, \quad (16)$$

and for solid solutions with the bcc structure

$$g_e^b = A^b x(1-x) + (1-x)\Delta_4. \quad (17)$$

The parameters Δ_3 and Δ_4 in (16) and (17) describe the difference between the free energies of the metastable and stable pure phases:

$$\begin{aligned} \Delta_3(P, T) &= g_3^h(P, T) - g_3^b(P, T), \\ \Delta_4(P, T) &= g_4^b(P, T) - g_4^h(P, T). \end{aligned} \quad (18)$$

As was shown in Ref. 9, taking into account the differences of the crystal structures of the phases formed in the phase separation of ^3He - ^4He solid solutions leads to an increase of T_{ps} as compared to the value given by (1). In particular, at small x the expression for the phase separation temperature now becomes

$$T_{ps} = \frac{A^h(1-2x) + \Delta_3}{\ln(1/x-1)}. \quad (19)$$

The parameters Δ_3 and Δ_4 in Ref. 9 are expressed in terms of the corresponding molar volumes and pressures. In particular, if the phonons and nuclear spins are neglected, we obtain the following expression for Δ_3 :

$$\frac{\partial \Delta_3}{\partial P} = V_3^h - V_3^b = \delta V_3, \quad (20)$$

which gives

$$\Delta_3 = \int_{P_3^0}^P \delta V_3 dP' = (P - P_3^0) \left[\delta V_3^0 + \frac{1}{2} \beta (P - P_3^0) \right], \quad (21)$$

where $\beta = 1.24 \times 10^{-3} \text{ cm}^3/(\text{mole} \cdot \text{atm})$, and the parameters P_3^0 and δV_3^0 were obtained from the experimental data¹⁵ for pure ^3He by extrapolation to $T=0$: $\delta V_3^0 = -0.09 \text{ cm}^3/\text{mole}$ at $P_3^0 = 102.9 \text{ bar}$. The values obtained for Δ_3 are plotted as a function of pressure in Fig. 3.

The other parameter of the theory appearing in Eq. (19), A^h , was determined in Ref. 9: $A^h = 0.76 \text{ K}$. Then the phase separation line constructed in the framework of the theory of regular solutions with allowance for the difference in crystal structures is shown by the curve 2 in Fig. 2. It is seen that this approach gives a good description of the experimental data both for cooling and for heating at temperatures below 150 mK, where there are no hysteresis effects.

At temperatures above 150 mK, however, the points obtained on heating are in better agreement with the calculated curve, apparently because of the more rapid establishment of equilibrium in that case. In this regard we note that the last experimental point, corresponding to the maximum concentration (represented by an asterisk in Fig. 2), is known to be elevated in temperature because an appreciable rate of dissolution of the ^3He inclusions in the immediate vicinity of the phase separation temperature of the initial solution could be obtained only with a comparatively large overheating of the sample.

The comparison of the experimental results with the different theories would not be complete without considering the asymmetric model of Mullin.² Reference 2 shows only the result of a numerical calculation, according to which this line is asymmetric and has a maximum shifted below the concentration $x=0.5$. The left branch of this line, corresponding to dilute solutions of ^3He in ^4He , is shown in Fig. 2 by curve 3, which lies substantially above the experimental planes.

5. CONCLUSION

We have shown that the method of measuring the pressure jump due to phase separation of ^3He – ^4He solid solutions at constant volume is very convenient for constructing the phase diagram of the process. This method has an advantage over the existing method based on detection of the kink on the temperature dependence of the pressure in that, besides being more accurate, it enables one to construct the line of phase separation in the whole region $x < x_0$. The technique of obtaining uniform high-quality samples of solid solutions of helium isotopes through the use of several cycles of cooling and heating in the phase separation region makes it possible to achieve highly reproducible experimental data without appreciable hysteresis effects.

We have found that the experimental phase separation

curve differs considerably from the curve calculated in the usual theory of regular solutions, with only the excess thermodynamic functions taken into account.

The asymmetric model of Mullin, which takes into account only the difference in the molar volumes of the pure components also gives poor agreement with the experimental data. We have shown that the experimental results are described well only in the Edwards–Balibar approach, in which the theory of regular solutions is supplemented by allowance for the fact that the phases arising on separation have different crystal structures.

*E-mail: rudavskii@ilt.kharkov.ua

¹D. O. Edwards, A. S. McWilliams, and J. G. Daunt, *Phys. Rev. Lett.* **9**, 195 (1962).

²W. J. Mullin, *Phys. Rev. Lett.* **20**, 254 (1968).

³L. H. Nosanov, *Phys. Rev.* **146**, 120 (1966).

⁴M. F. Panczyk, R. A. Scribner, J. R. Gonano, and E. D. Adams, *Phys. Rev. Lett.* **21**, 594 (1968).

⁵A. E. Burgess and M. J. Crooks, *Phys. Lett. A* **39**, 183 (1972).

⁶I. Iwasa and H. Suzuki, in *Proceedings LT-17, Amsterdam (1984)*, p. 531.

⁷S. W. Ehrlich and R. O. Simmons, *J. Low Temp. Phys.* **68**, 125 (1987).

⁸B. A. Fraas and R. O. Simmons, *Phys. Rev. B* **36**, 97 (1987).

⁹D. O. Edwards and S. Balibar, *Phys. Rev. B* **39**, 4083 (1989).

¹⁰V. A. Shvarts, N. P. Mikhin, É. Ya. Rudavskii, Yu. A. Tokar', A. M. Usenko, and V. A. Mikheev, *Fiz. Nizk. Temp.* **20**, 7 (1994) [*Low Temp. Phys.* **20**, 505 (1994)].

¹¹S. C. J. Kingsley, Ph. D. Thesis, University of London (1997).

¹²A. N. Gan'shin, V. N. Grigor'ev, V. A. Maïdanov, N. F. Omelaenko, A. A. Penzev, É. Ya. Rudavskii, A. S. Rybalko, and Yu. A. Tokar', *Fiz. Nizk. Temp.* **25**, 796 (1999) [*Low Temp. Phys.* **25**, 592 (1999); **25**, 928 (1999)].

¹³A. N. Gan'shin, V. A. Maïdanov, N. F. Omelaenko, A. A. Penzev, É. Ya. Rudavskii, and A. S. Rybalko, *Fiz. Nizk. Temp.* **24**, 815 (1998) [*Low Temp. Phys.* **24**, 840 (1998)].

¹⁴V. N. Grigor'ev, *Fiz. Nizk. Temp.* **23**, 5 (1997) [*Low Temp. Phys.* **23**, 3 (1997)].

¹⁵G. S. Straty and E. D. Adams, *Phys. Rev.* **150**, 123 (1966).

Translated by Steve Torstveit

LOW-TEMPERATURE MAGNETISM

Structure genesis and magnetic orderings in compounds of the ThCr_2Si_2 type

B. R. Gadjiev*

I. M. Frank Neutron Physics Laboratory, Joint Institute for Nuclear Research, 14190 Dubna, Moscow District, Russia

(Submitted April 11, 2000; revised July 10, 2000)

Fiz. Nizk. Temp. **26**, 1182–1190 (December 2000)

It is shown in a phenomenological approach that the symmetry space group $I4/mmm$ of the paramagnetic phase in compounds of the ThCr_2Si_2 type arises as a result of a structural phase transition from a close-packed paraphase with space group $Im\bar{3}m$. It is found that the real magnetic orderings in compounds of the ThCr_2Si_2 type is described by transition parameters belonging to a single direction, along the line joining the points of maximum symmetry in the Brillouin zone of the $I4/mmm$ group. It is shown that the variations of the modulus of the wave vector are a consequence of a change in the dopant concentration. The spatial dependence of the order parameter in the incommensurate phases is obtained for the corresponding universality classes. © 2000 American Institute of Physics. [S1063-777X(00)00212-7]

INTRODUCTION

Neutron-diffraction studies of the structures of compounds with variable composition have shown that, in spite of the fact that the symmetry space group of the crystal remains unchanged over a rather wide temperature interval, the magnetic ordering in the crystals undergoes a sequence of phase transitions of the paramagnetic–incommensurate–commensurate type.^{1–4} The neutron-diffraction results show^{3,4} that in crystals with variable composition, the wave vector of the magnetic structure varies as the dopant concentration x is varied over the interval $0 \leq x \leq 1$. As a rule, the wave vector of the magnetic structure varies along a definite direction in the Brillouin zone corresponding to the space group of the structure, and a change in the magnitude of the wave vector occurs between the highest-symmetry points of the Brillouin zone. This circumstance indicates that the symmetry group of the wave vector is lowered.^{3,4}

These isostructural compounds are treated in terms of the concept of a paraphase, according to which the phase that exists in reality is represented as being the result of a slight distortion of a hypothetical high-symmetry structure (the paraphase).^{5,6} Neutron-diffraction studies of the structures of the compounds UPd_2Si_2 , UPd_2Ge_2 , URh_2Si_2 , and URh_2Ge_2 show that these crystals have a structure that is common to intermetallic compounds of the ThCr_2Si_2 type.¹ In the paramagnetic phase these structures have space group $I4/mmm$. It is known that the magnetic ordering in these isostructural compounds is due to the uranium atoms, and in UPd_2Si_2 and UPd_2Ge_2 crystals an incommensurate phase appears. It has been shown experimentally that UPd_2Si_2 , UPd_2Ge_2 , and URb_2Si_2 have antiferromagnetic ordering below temperatures of 150, 140, and 137 K, respectively, with the wave vectors of the magnetization lying along the c axis of the tetragonal body-centered lattice. The wave vectors of the modulation in the compounds UPd_2Si_2 and UPd_2Ge_2 are $\mathbf{q} = (0, 0, 0.662 \pm 0.010)c^*$ and $\mathbf{q} = (0, 0, 0.748 \pm 0.010)c^*$,

and at $T = 40$ K the former compound (UPd_2Si_2) undergoes a magnetic phase transition to a commensurate phase with wave vector $\mathbf{q} = (0, 0, 1)c^*$. In these structures the modulation is one-dimensional (of the longitudinal spin wave (LSW) type).¹ Later neutron-dislocation studies revealed a sequence of modulated magnetically ordered phases in UPd_2Ge_2 at temperatures below $T_N \approx 135$ K, and at 80 K the wave vector of the modulation has the commensurate value $\mathbf{q} = (0, 0, k_s = 3/4)$.^{2,3} It has been shown^{3,4} that the substitution of Fe for only 2% of the Pd radically alters the magnetic structure of UPd_2Ge_2 without altering its space group. Thus, while the magnetic structure of the undoped compound at $T < 50$ K is a phase with quadratic modulation, the compound $\text{U}(\text{Pd}_{0.98}\text{Fe}_{0.02})_2\text{Ge}_2$ has a “simple” antiferromagnetic phase below 65 K. The concentration dependence of the temperatures of the phase transitions from the paramagnetic to the incommensurate phase (T_N) and from the incommensurate to the commensurate phase (T_C) was studied in Ref. 7. It was shown that increasing the dopant concentration has practically no effect on $T_N(x)$, whereas $T_C = T_C(x)$ increases, reaching ~ 110 K. In addition, as x increases, the magnitude of the modulation wave vector changes, the change in \mathbf{q} occurring along a definite direction of the Brillouin zone.

In a theoretical description of the magnetic phase transitions in crystals with variable composition one can use the analogy with the Landau theory of phase transitions for ferroelectric semiconductors.⁸ In that case, essentially, the coefficients of the thermodynamic potential acquire a dependence on the dopant concentration. Analysis shows^{4,9} that the magnitude of the modulation wave vector and the temperature existence region of the incommensurate phase become functions of the dopant concentration. For example, as x increases, the temperature interval in which the incommensurate phase exists becomes narrower and ultimately vanishes. In addition, \mathbf{q} goes to zero with increasing concentration x .

This means that an order–order transition should be observed on the x – T diagram, viz., a ferromagnetic–antiferromagnetic transition.

The analysis given above makes it possible to understand the genesis of the structures and magnetic phase transitions in crystals with variable composition. This paper is devoted to a concrete analysis of the sequence of magnetic phase transitions of the paramagnetic–incommensurate–commensurate type and of the possible changes of the phase diagram of the structure as the dopant concentration is increased.

SEQUENCE OF MAGNETIC PHASE TRANSITIONS IN TETRAGONAL STRUCTURES

In the theory of phase transitions the necessity of representing some structures as being derived from higher-symmetry structures is due, as a rule, to the following two circumstances.⁶ First, if a reversible transition between phases with degenerate and derivative structures is actually observed, then it is necessary to establish the order parameter in order to determine the free energy functional, with which one can calculate the anomalies of the thermodynamic functions. Second, in those cases when only one phase, whose structure can be represented as being derived from a degenerate structure, is actually observed, a study of the symmetry properties of the order parameter relating the degenerate and derivative structures enables one to understand a number of physical properties which would otherwise seem accidental.

From the standpoint of the genesis of the structures of crystals with variable composition, it should be noted that in the general case the symmetry of complex compounds whose structure is derived from a close-packed structure having one of the space groups D_{6h}^4 , O_h^5 , or O_h^9 for the paraphase, is in reality lower than the symmetry of the analogous structures made up of identical spheres.⁶ In a theoretical treatment one can always introduce a purely geometric characteristic — an order parameter — that describes some particular lowering of the symmetry. We stress that by definition the order parameter is a purely crystallographic concept that enables one to describe the symmetry difference between the probability density of the charge or current distribution in the degenerate and derivative structures.

As we know,⁸ it is assumed in a symmetry analysis of magnetic structures that any magnetic structure can be regarded as being the result of a magnetic phase transition from some initial phase. Consequently, the Landau theory of phase transitions^{4,8} can be used in a symmetry analysis of magnetic structures. In particular, the Landau theory enables one to predict the general features of the phase diagram on the concentration–temperature plane for structures with variable composition.

Let the points Γ and H of the Brillouin zone have the highest structural symmetry Γ_0 . This means that the group of wave vectors Γ and H is the space group G_0 . Let the wave vector \mathbf{q} define the line joining the Γ and H points. In this case the symmetry group G_q of the wave vector \mathbf{q} is lower than the symmetry of the Γ and H points and is a subgroup of G_0 . It is clear that the points of the direction \mathbf{q} are internal points of the Brillouin zone. Thus the dimension of the irreducible representation of the symmetry space group G_0 cor-

responding to the points of \mathbf{q} is greater than or equal to the dimension of the irreducible representations of the group G_0 corresponding to the Γ and H points. The irreducible representations of the group G_0 corresponding to the internal points of the Brillouin zone do not satisfy the Lifshitz condition.¹⁰ Since a Landau analysis is based on knowledge of the free energy functional, which is made up of a complete rational basis of invariants and determines the universality class, the change of the wave vector \mathbf{q} due to the change in dopant concentration causes a change in the universality class. As applied to real structures with variable composition, this last statement means that for different values of the dopant concentration the magnetic orderings in the structure can be substantially different.⁴

Thus a study of the symmetry properties of the order parameter relating the degenerate and derivative structures makes it possible to understand a number of physical properties that would otherwise seem accidental.

The phases of symmetry $I4/mmm$ and $P4/mmm$ corresponding to real tetragonal structures can arise as a result of a phase transition from a paraphase with symmetry space group $Im3m$.⁵ Here the transition from the paraphase to the corresponding superstructure is described by an order parameter that transforms according to the irreducible representation of the group $Im3m$ belonging to the point $\mathbf{k}_8 = (0, 0, 2\pi/na)$ (a is the lattice parameter of the cubic cell of the paraphase, and n is the ratio of the volumes of the unit cells of the tetragonal structure and paraphase). The star of the vector \mathbf{k}_8 contains six rays, and the corresponding order parameter transforms according to a six-dimensional irreducible representation $\tau_1(\mathbf{k}_8)$ induced by a totally symmetric small representation of the group of the wave vector $G_{\mathbf{k}_8} = 4mm$. The phases of symmetry $I4/mmm$ and $P4/mmm$ arise for odd and even values $n \geq 3$, when only two rays of \mathbf{k}_8 are active (e.g., $\mathbf{k}_8^{(1)}$ and $-\mathbf{k}_8^{(1)}$), i.e., only two, conjugate components of the order parameter are nonzero.

We stress that the vector \mathbf{k}_8 characterizes a line Δ which begins at the Brillouin zone center Γ and ends at the vertex H .¹¹ The groups of the wave vectors corresponding to the Γ and H points are the same, $Im3m$. Thus the Γ and H points have the highest structural symmetry, $Im3m$, and on the line Δ the symmetry is lowered to $4mm$. Since the line Δ is internal to the Brillouin zone, a six-dimensional irreducible representation of the group $Im3m$ corresponding to the line Δ is passive, and consequently the phase transition $Im3m \rightarrow I4/mmm$ in the general case takes place through an incommensurate phase.

Let us consider the structure with space group $I4/mmm$ in the paramagnetic phase. In the Brillouin zone the line characterized by a vector $\mathbf{k}_{10} = (0, 0, 2\mu\pi/\tau_z)$, begins at the center $\mathbf{k}_{14} = (0, 0, 0)$ and ends at the point $\mathbf{k}_{15} = (0, 0, \pi/\tau_z)$.^{4,12} The groups of the wave vectors \mathbf{k}_{14} and \mathbf{k}_{15} are the same and have the total symmetry of the structure, $G_{\mathbf{k}} = I4/mmm$. The group $G_{\mathbf{k}_{10}}$ of the wave vector \mathbf{k}_{10} is $I4mm$. The irreducible representations of the small group $I4mm$ of the vector $\mathbf{k} = (0, 0, k_z)$ is presented below:

$I4mm$	E	C'_2	σ_h	σ_v	σ'_h	σ'_v	C_4	C'_2
A_1	1	1	1	1	1	1	1	1
A_2	1	1	-1	-1	-1	-1	1	1
B_1	1	1	1	1	-1	-1	-1	-1
B_2	1	1	-1	-1	1	1	-1	-1
E	1 0	-1 0	1 0	-1 0	0 1	0 -1	0 -1	0 1
	0 1	0 -1	0 -1	0 1	1 0	-1 0	1 0	-1 0

Consequently, the space group $I4/mmm$ has four two-dimensional and one four-dimensional irreducible representations corresponding to the wave vector $\mathbf{k}_{10}=(0,0,2\mu\pi/\tau_z)$. The space group $I4/mmm$ has eight one-dimensional and two two-dimensional irreducible representations A_{1g} , A_{2g} , B_{1g} , B_{2g} , E_g , A_{1u} , A_{2u} , B_{1u} , B_{2u} , and E_u , which correspond to the Brillouin zone center.¹³ Since the group $I4/mmm$ is a symmorphic group, the irreducible representations $I4/mmm$ corresponding to the point $\mathbf{k}_{15}=(0,0,\pi/\tau_z)$ are given by¹⁴

$$D_{\mathbf{k}_{15},i}(\{\beta|\mathbf{b}\}) = \exp(-i\mathbf{k}_{15}\mathbf{b})\Gamma_i,$$

where \mathbf{b} is a reciprocal lattice vector, and $\Gamma_i \in [A_{1g}, A_{2g}, B_{1g}, B_{2g}, E_g, A_{1u}, A_{2u}, B_{1u}, B_{2u}, E_u]$.

It can be shown by a direct calculation that the two-dimensional $\tau_4(\mathbf{k}_{15})$ and four-dimensional $\tau_5(\mathbf{k}_{15})$ irreducible representations of the space group $I4/mmm$ induced by the representations A_2 and E are also contained in the magnetic representation. The decomposition of the pseudovector representation τ_{pv} in the irreducible representations of the group $I4/mmm$ has the form

$$\tau_{pv} = A_{2g} \oplus E_g.$$

Below we discuss the sequence of magnetic phase transitions from the incommensurate phase which are associated with the one-dimensional $D_{\mathbf{k}_{15},2}$ and two-dimensional $\tau_4(\mathbf{k}_{15})$ irreducible representations of the group $I4/mmm$ and which correspond to the vectors $\mathbf{q}=(0,0,\pi/\tau_z)$ and $\mathbf{q}=(0,0,2\pi\mu/\tau_z)$ contained in the magnetic representation. The L group in the case of the one-dimensional irreducible representation $D_{\mathbf{k}_{15},2}$ consists of two matrices, namely (1) and (-1) . In accordance with the condition of invariance, the thermodynamic potential functional is expressed as

$$\Phi_0 = \frac{1}{d} \int_0^d \tilde{\Phi}_0(z) dz,$$

where

$$\begin{aligned} \tilde{\Phi}_0(z) = & \frac{\alpha_0}{2} \eta^2(z) + \frac{\beta_0}{4} \eta^4(z) + \frac{\gamma_0}{6} \eta^6(z) + \frac{\delta_0}{2} (\eta')^2 \\ & + \frac{\lambda_0}{2} (\eta'')^2 + \frac{\chi_0}{2} \eta^2 (\eta')^2, \end{aligned} \quad (1)$$

d is the period of $\tilde{\Phi}_0(z)$, and a prime denotes a derivative with respect to z .¹⁵

We supplement the thermodynamic potential with an additional term characterizing the energy E_g of the electron subsystem of the dopant atoms incorporated in the structure. Then the term mE_g (m is the dopant concentration) incorpo-

rates the change in the thermodynamic potential of the electron subsystem due to the interaction of the matrix and dopant atoms. Assuming that $E(\eta)$ is invariant with respect to the same symmetry transformations, we can write

$$\begin{aligned} E_g(\eta) = & E_0 + \frac{a}{2} \eta^2(z) + \frac{b}{4} \eta^4(z) + \frac{\gamma'}{6} \eta^6(z) \\ & + \frac{\delta'}{2} (\eta')^2 + \frac{\lambda'}{2} (\eta'')^2 + \frac{\chi'}{2} \eta^2 (\eta')^2. \end{aligned} \quad (2)$$

Consequently, the thermodynamic potential functional is represented by the expression

$$\Phi = \frac{1}{d} \int_0^d \bar{\Phi}(z) dz,$$

where

$$\begin{aligned} \bar{\Phi}(z) = & \frac{\alpha}{2} \eta^2 + \frac{\beta}{4} \eta^4 + \frac{\gamma}{6} \eta^6 + \frac{\delta}{2} (\eta')^2 \\ & + \frac{\lambda}{2} (\eta'')^2 + \frac{\chi}{2} \eta^2 (\eta')^2, \end{aligned} \quad (3)$$

with $\alpha = \alpha_0 + ma$, $\beta = \beta_0 + mb$, $\gamma = \gamma_0 + m\gamma'$, $\delta = \delta_0 + m\delta'$, $\lambda = \lambda_0 + m\lambda'$, and $\chi = \chi_0 + m\chi'$.

The equilibrium phases of the system are determined from the condition of minimum thermodynamic potential. Thus we obtain for the initial paramagnetic phase

$$\eta = 0, \quad \Phi = 0. \quad (4)$$

In the commensurate antiferromagnetic phase $\eta' = 0$ and, hence,

$$\Phi = \frac{\alpha}{2} \eta^2 + \frac{\beta}{4} \eta^4 + \frac{\gamma}{6} \eta^6, \quad (5)$$

and from the minimization condition we find that

$$\eta_c = \pm \left(\frac{-\beta + (\beta^2 - 4\alpha\gamma)^{1/2}}{2\gamma} \right)^{1/2},$$

which implies that

$$\Phi_c = - \frac{6\alpha\beta\gamma - \beta^2 + (\beta^2 - 4\alpha\gamma)^{1/2}}{24\gamma^2}. \quad (6)$$

In the incommensurate phase we obtain from Euler's equation an equation for $\eta(z)$ and find the minimum of Φ :

$$\lambda \eta^{(IV)} - \delta \eta'' - \chi [\eta^2 \eta'' + \eta (\eta')^2] + \alpha \eta + \beta \eta^3 + \gamma \eta^5 = 0. \quad (7)$$

This last equation can have periodic solutions with different periods d . The equilibrium period d is determined by the condition $\delta\Phi/\delta d = 0$, which takes the form

$$\begin{aligned} \lambda \eta''' \eta' - \frac{\lambda}{2} (\eta'')^2 - \frac{\delta}{2} (\eta')^2 - \frac{\chi}{2} \eta^2 (\eta')^2 \\ + \frac{\alpha}{2} \eta^2 + \frac{\beta}{4} \eta^4 + \frac{\lambda}{6} \eta^6 = 0. \end{aligned} \quad (8)$$

Condition (8) can take a different form if it is integrated over z from zero to d and substitute the expression for Φ :

$$\int_0^d [2\lambda(\eta'')^2 + \delta(\eta')^2 + \chi(\eta')^2 \eta^2] dz = 0. \quad (9)$$

In the sinusoidal regime of the incommensurate phase, where $\eta \rightarrow 0$, we obtain the following in a first approximation, using the standard expansions:

$$\begin{aligned} \eta &= \rho_0 \cos(qx), & \rho_0^2 &= \frac{4(\alpha_0 - \alpha)}{3\beta + 2\chi q_0^2}, \\ q &= q_0 \left(1 + \frac{\rho_0^2 \chi}{8\delta} \right), & \alpha_0 &= \frac{\delta^2}{4\lambda}, \\ q_0^2 &= -\frac{\delta}{2\lambda}, & \Phi &= -\frac{(\alpha_0 - \alpha)^2}{2(3\beta + 2\chi q_0^2)}. \end{aligned} \quad (10)$$

Consequently, the modulation wave vector is a function of temperature and dopant concentration.

By making the substitution $Z = (\eta')^2$, we obtain an exact solution of equation (8):

$$\begin{aligned} \frac{\lambda}{8} \left[4Z \frac{d^2 Z}{d\eta^2} - \left(\frac{dZ}{d\eta} \right)^2 \right] - \frac{\delta}{2} Z - \frac{\chi}{2} \eta^2 Z \\ + \frac{\alpha}{2} \eta^2 + \frac{\beta}{4} \eta^4 + \frac{\gamma}{6} \eta^6 = \Phi. \end{aligned} \quad (11)$$

If the solution of this equation is known, the function $\eta = n(z)$ can be found from the relation

$$\int [Z(\eta)]^{-1/2} d\eta = z - z_0. \quad (12)$$

We seek the solution in the form

$$Z = \frac{\chi}{8\lambda} c \eta^4 + \frac{\beta}{\chi} g_1 \eta^2 + \frac{\beta^2 \lambda g_0}{\chi^3}, \quad (13)$$

where the unknown constants c , g_0 , and g_1 are dimensionless.

To determine c , g_0 , and g_1 we substitute (13) into (11) and obtain the following equations:

$$\begin{aligned} 3c(c-1) + 8\gamma &= 0, \\ 2g_1(5c-4) &= \delta c - 4, \\ g_0(2-3c) &= 2(g_1^2 - \delta g_1 + \alpha), \\ \Phi &= \frac{\beta^2 \lambda^2 g_0 (2g_1 - \delta)}{2\chi^4}. \end{aligned} \quad (14)$$

Equation (12) has a real solution only for $Z > 0$. The interval of values for which $Z > 0$ must be bounded, since otherwise η would reach infinite values. As a result, depending on the sign of χ and the number of real roots of the equation $Z(\eta) = 0$, there are three possible cases of interest.

I. For $\chi > 0$ and $\beta g_1 < 0$ the polynomial $Z(\eta)$ has four real roots. From Eq. (12) we find

$$\eta = \rho \operatorname{sn}(pz, k), \quad \rho^2 = -8 \frac{\beta \lambda k^2 g_1}{\chi^2 c (1+k^2)}, \quad (15)$$

$$p^2 = -\frac{\beta g_1}{\chi(1+k^2)}, \quad k^2 = \frac{1 - \sqrt{1 - c g_0 / 2g_1^2}}{1 + \sqrt{1 - c g_0 / 2g_1^2}},$$

where $\operatorname{sn}(pz, k)$ is a Jacobi elliptic function with modulus k , and p is the wave vector.

II. For $\chi < 0$, if $g_0 < 0$ the polynomial $Z(\eta)$ has only two real roots. There is a single region in which $Z > 0$, and after some manipulations, Eq. (12) gives

$$\begin{aligned} \eta &= \rho \operatorname{cn}(pz, k), & \rho^2 &= \frac{8\beta \lambda k^2 \bar{g}_1}{\chi^2 c}, \\ p^2 &= -\frac{\beta \bar{g}_1}{\chi}, & k^2 &= \frac{1}{2} \left[1 \pm \left(1 - \frac{c g_0}{2g_1^2} \right)^{-1/2} \right], \end{aligned} \quad (16)$$

where $\bar{g}_1 = g_1 / (1 - 2k^2)$ and, hence, $\beta \bar{g}_1 > 0$. Here $\operatorname{cn}(pz, k)$ is a Jacobi elliptic function. It should be emphasized that the phases corresponding to solutions I and II are separated by a line of Lifshitz points determined by the equation $\chi = 0$.

III. For $\chi < 0$, $\beta g_1 < 0$ the polynomial $Z(\eta)$ has four real roots. In this case we find from Eq. (12) that

$$\begin{aligned} \eta &= \rho \operatorname{dn}(pz, k), & \rho^2 &= -8 \frac{\lambda \beta g_1}{\chi_2 c (2-k^2)}, \\ p^2 &= \frac{\beta g_1}{\chi(2-k^2)}, & k^2 &= \frac{2\sqrt{1 - c g_0 / 2g_1^2}}{1 + \sqrt{1 - c g_0 / 2g_1^2}}. \end{aligned} \quad (17)$$

Since the elliptic function $\operatorname{dn}(pz, k) > 0$, this incommensurate phase in magnets has a nonzero average magnetization.

The temperature dependence of the parameter k ($0 \leq k \leq 1$) in phases I, II, and III is determined by direct substitution of solutions (15)–(17), respectively, into Eq. (9). The value $k = 0$ corresponds to the temperature of the transition from the paramagnetic phase to the incommensurate phase (T_N), and $k = 1$ corresponds to the transition temperature from the incommensurate to the commensurate phase (T_C). In addition, Eq. (9) determines the temperature interval in which the incommensurate phase exists. Because of the concentration dependence of the coefficients of the thermodynamic potential, the temperature interval $T_N - T_C$ depends on m , becoming narrower as m increases. It follows from the explicit form of the solution (15) and (16) that the magnetic moments in phases I and II are ordered antiferromagnetically. In phase III the ordering is ferromagnetic.

It should be emphasized that because the coefficients of the thermodynamic potential are functions of the dopant concentration, there can be a succession of phases I, II, and III on the $x-T$ diagram. Moreover, the commensurate phase determined by functional (3) is antiferromagnetically ordered. In this case the magnetic cell is doubled in the commensurate phase.

Let us consider the two-dimensional irreducible representation of the space group $I4/mmm$ which corresponds to the vector $\mathbf{q} = (0, 0, k_s)$, specifying an internal point of the Brillouin zone.^{16,17} This irreducible representation clearly does not satisfy the Lifshitz condition, and the phase transi-

tion in the system is therefore described by a two-component order parameter, and the thermodynamic potential functional contains a Lifshitz invariant.

Let us assume that the structure is uniform in the directions x and y ; then the thermodynamic potential functional is a one-dimensional integral along the z direction.

From symmetry considerations we express the thermodynamic potential functional as

$$F = \frac{1}{d} \int_0^d \tilde{f}(z) dz$$

where

$$\begin{aligned} \tilde{f}(z) = & \frac{\alpha_0}{2} \rho^2 + \frac{\beta_0}{4} \rho^4 + \gamma_0 \rho^8 \cos 8\varphi - \delta_0 \rho^2 \varphi' \\ & + \frac{k_0}{2} \rho^2 (\varphi')^2 + \frac{\lambda_0}{2} \rho^2 (\varphi'')^2, \end{aligned} \quad (18)$$

and ρ and φ are the amplitude and phase of the order parameter.

When (18) is taken into account, the expression for the thermodynamic potential becomes

$$\begin{aligned} E_g = E_0 + & \frac{a}{2} \rho^2 + \frac{b}{4} \rho^4 + \Gamma \rho^8 \cos 8\varphi - \Delta \rho^2 \varphi' \\ & + \frac{k'}{2} \rho^2 (\varphi')^2 + \frac{\lambda'}{2} \rho^2 (\varphi'')^2. \end{aligned} \quad (19)$$

Now the thermodynamic potential functional can be written as

$$\begin{aligned} F = & \frac{1}{d} \int_0^d f(z) dz, \\ f(z) = & \frac{\alpha}{2} \rho^2 + \frac{\beta}{4} \rho^4 + \gamma \rho^8 \cos 8\varphi - \delta \rho^2 \varphi' \\ & + \frac{k}{2} \rho^2 (\varphi')^2 + \frac{\lambda}{2} \rho^2 (\varphi'')^2, \end{aligned} \quad (20)$$

where $\alpha = \alpha_0 + am$, $\beta = \beta_0 + bm$, $\gamma = \gamma_0 + \Gamma m$, $\delta = \delta_0 + m\Delta$, $\lambda = \lambda_0 + m\lambda'$, and $k = k_0 + mk'$.

The harmonic solution representing the incommensurate phase is $\varphi = kx$, and from the equilibrium condition on the thermodynamic potential we obtain

$$k_0 = \frac{\delta}{k}, \quad \rho^2 = \frac{1}{\beta} (\alpha_0 - \alpha), \quad \alpha_0 = \frac{\delta^2}{k}. \quad (21)$$

Minimization of the thermodynamic potential functional (20) with respect to the phase leads to an Euler equation of the form

$$\lambda \varphi^{(IV)} - k \varphi'' - 16\gamma\rho^6 \sin 4\varphi \cos 4\varphi = 0. \quad (22)$$

Before solving Eq. (22), let us remark that on the phase diagram of the system described by the functional (20), the line of Lifshitz points is determined by the equation $k(P, T, m) = 0$, where P is the pressure. Consequently, the line of Lifshitz points separates phases with $k(P, T, m) < 0$ and $k(P, T, m) > 0$. Let us first determine the solution of equation (22) that describes the incommensurate phase for which $k(P, T, m) < 0$.

The first integral of equation (22) has the form

$$\lambda \left[\varphi' \varphi''' - \frac{1}{2} (\varphi'')^2 \right] - \frac{k}{2} (\varphi')^2 + 2\gamma\rho^6 \cos^2 4\varphi = \xi, \quad (23)$$

where ξ is a constant of integration.

After the substitution

$$S(\varphi) = (\varphi')^2, \quad \cos 4\varphi = t \quad (24)$$

Eq. (23) can be written in the form

$$\begin{aligned} \lambda [8(1-t^2)S(t)S''(t) - 8tS(t)S'(t) - 2(1-t^2)(S'(t))^2] \\ - \frac{k}{2} S(t) + 2\gamma\rho^6 t^2 = \xi. \end{aligned} \quad (25)$$

We seek the solution of equation (25) in the form

$$S(t) = A + Bt. \quad (26)$$

By direct substitution we find

$$(\varphi')^2 = A + B \cos 4\varphi, \quad (27)$$

where $A = -k/16\lambda$, $B = (w/6\lambda)^{1/2}$, $\omega = 2\gamma\rho^6$. The solution of equation (20) has the form

$$z = \int_0^\varphi \frac{dt}{(A + B \cos 4t)^{1/2}}. \quad (28)$$

The intersoliton distance is determined by the expression

$$z_0 = \frac{2}{\pi} K(k) d_0, \quad (29)$$

where the soliton width is given by the expression

$$d_0 = \frac{\pi}{8(A+B)^{1/2}}. \quad (30)$$

Here $K(k)$ is the elliptic integral of the first kind.

The incommensurate phase described by solution (28) with $k(P, T, m) < 0$ will be called incommensurate phase II.

Let us determine the solution of equation (22) for $k(P, T, m) > 0$; to a first approximation, we shall assume that λ/k is small. Then the phase of the order parameter is determined as the solution of the one-dimensional sine-Gordon equation

$$k \varphi'' + 16\gamma\rho^6 \sin 4\varphi \cos 4\varphi = 0. \quad (31)$$

The first integral of this equation has the form

$$\frac{k}{2} (\varphi')^2 + 2\gamma\rho^6 \sin 4\varphi = \mu, \quad (32)$$

where μ is a constant of integration. After making the substitution $g(u) = w \sin^2 u$, where $u = 4\varphi$, we write the solution of equation (32) as

$$z = \frac{1}{4} \left(\frac{k}{2} \right)^{1/2} \int_0^{4\varphi} \frac{du}{[\mu - g(u)]^{1/2}}. \quad (33)$$

The incommensurate phase described by solution (33) will be called incommensurate phase I.

In the commensurate phase the expression for the magnetic moment in the n th unit cell of the crystal in terms of the magnetic moment in the first cell is

$$\mathbf{M}_n = \mathbf{M}_1 \exp(i\mathbf{k} \cdot \mathbf{t}_n) + \mathbf{M}_1 \exp(-i\mathbf{k} \cdot \mathbf{t}_n).$$

It follows from this expression that in the case $\mathbf{M}_1 = M/2(\mathbf{m}_1 + ip\mathbf{m}_2)$, $(\mathbf{m}_1 \cdot \mathbf{m}_2) = 0$, $\mathbf{m}_1^2 = \mathbf{m}_2^2$, with an ellipticity parameter $p \neq 0$, the magnetic moment

$$\mathbf{M}_n = M[\mathbf{m}_1 \cos(\mathbf{k} \cdot \mathbf{t}_n) - p\mathbf{m}_2 \sin(\mathbf{k} \cdot \mathbf{t}_n)]$$

describes an elliptical helix in space.

If we set $p=0$, then we have a structure of the spin-wave type, for which

$$\mathbf{M}_n = M\mathbf{m}_1 \cos(\mathbf{k} \cdot \mathbf{t}_n).$$

For $\mathbf{m}_1 \parallel \mathbf{k}$ this last expression describes an LSW structure, and for $\mathbf{m}_1 \perp \mathbf{k}$ it describes a TSW structure. The change in volume of the magnetic cell in the commensurate phase is determined by a commensurate value of the wave vector.

The temperature width of the existence region of the incommensurate phase is determined by the relation

$$\frac{E(k)}{k} = \frac{1}{a} \left[c + \frac{1}{1 + b(1 - T/T_N)} \right]^{-1} (1 - T/T_N)^{-3/2},$$

where $E(k)$ is the elliptic integral of the second kind; $0 \leq k \leq 1$, and a , b , and c are certain parameters of the thermodynamic potential. It is clear that as the dopant concentration increases, the temperature region in which the incommensurate phase exists becomes narrower.

CONCLUSIONS

The tetragonal structure with space group $I4/mmm$, which is the magnetic symmetry group of the paramagnetic phase, arises as a result of a structural phase transition from the close-packed paraphase with space group $Im3m$. The transformation properties of the order parameter describing the structural phase transition $Im3m \rightarrow I4/mmm$ are determined by the six-dimensional irreducible representation of the group $Im3m$ corresponding to the wave vector $\mathbf{k} = (0, 0, 2\pi/na)$, while the $I4/mmm$ phase arises for odd values $n \geq 3$, when only two rays of \mathbf{k}_8 are active, i.e., only two, conjugate components of the order parameter are non-zero. The line Δ is characterized by the vector \mathbf{k}_8 , the group of the wave vector of which is $I4mm$, and it begins at the center and ends at the vertex H of the Brillouin zone. The symmetry groups of the Γ and H points are maximal in the sense that the structure has its highest symmetry. Since the line Δ is internal to the Brillouin zone, the six-dimensional irreducible representation is passive, and the Lifshitz condition is not satisfied. Therefore, in principle, the structural phase transition $Im3m \rightarrow I4/mmm$ takes place through an intermediate incommensurate phase, and $I4/mmm$ is the symmetry of the commensurate phase.

In the Brillouin zone of the tetragonal paramagnetic phase with symmetry $I4/mmm$ the points with the highest symmetry are the center $\mathbf{k}_{14} = (0, 0, 0)$ and the surface point $\mathbf{k}_{15} = (0, 0, \pi/\tau_z)$. The line connecting these points is contained by a vector $\mathbf{k}_{10} = (0, 0, 2\mu\pi/\tau_z)$, the wave vector of which has the group $4mm$. The one-dimensional irreducible representation $D_{\mathbf{k}_{15,2}}$ of the group $I4/mmm$ which corresponds to the vector \mathbf{k}_{15} , contained in the magnetic representation, determines a thermodynamic potential functional without a Lifshitz invariant. This functional describes a structure of the LSW type. The equilibrium condition of the functional determines an ordering of the type

$\eta = \rho \operatorname{sn}(pz, k)$ and $\eta = \hbar \operatorname{cn}(pz, k)$ and a phase with ferromagnetic ordering of the type $\eta = \rho \operatorname{dn}(pz, k)$. The commensurate phase that corresponds to these phases is antiferromagnetically ordered, and the magnetic cell is doubled.

The thermodynamic potential functional made up of invariants of the irreducible representation of the group $I4/mmm$ corresponding to the wave vector $\mathbf{k}_{10} = (0, 0, 2\mu\pi/\tau_z)$, which is contained in the magnetic representation, contains a Lifshitz invariant. Minimizing this functional leads to two different solutions, which correspond to different incommensurate phases. On the phase diagram these phases are separated by a line of Lifshitz points.

We note that in magnets the physical reason for the appearance of Lifshitz invariants is the relativistic Dzyaloshinskii–Moriya interaction.⁸ For a functional with a Lifshitz invariant a solution of the LSW type arises in the case when the ellipticity parameter is equal to zero and the magnetic moments are directed along the modulation wave vector.

Furthermore, the size of the temperature interval in which the incommensurate phase exists in these compounds depends on the dopant concentration. The magnetic ordering depends on the magnitude of the modulation wave vector, and as this magnitude changes so do the magnetic symmetry groups in the commensurate phases. For example, a doubling of the magnetic cell of the commensurate phase is observed in crystals of $U(\text{Pd}_{0.98}\text{Fe}_{0.02})_2\text{Ge}_2$. In the compounds $U(\text{Pd}_{1-x}\text{Fe}_x)_2\text{Ge}_2$ the volume of the magnetic cell in the commensurate phase is quadrupled. For a detailed comparison of the results it will be necessary to carry out precision experiments to refine the interrelationship between the magnetic ordering and the magnitude of the modulation wave vector as a function of the dopant concentration in these families of compounds.

The author thanks Professors V. A. Aksenov and V. P. Dmitriev for a fruitful discussion of the results of this study.

*E-mail: gadjiev@nf.jinr.ru

- ¹H. Ptasiwicz-Bak, J. Leciejewicz, and A. Zygmunt, *J. Phys. F* **11**, 1225 (1981).
- ²G. Andre, F. Bouree, and A. Oles, *Solid State Commun.* **97**, 923 (1996).
- ³A. M. Balagurov, V. V. Sikolenko, I. S. Lyubutin, Zh. Andre, F. Bure, and Kh. M. Du, *JETP Lett.* **66**, 647 (1997).
- ⁴V. A. Aksenov and B. R. Gadjiev, OIYaI Preprint R17-98-256 [in Russian], Joint Institute for Nuclear Research, Dubna (1998).
- ⁵V. P. Dmitriev and P. Toledano, *Kristallografiya* **40**, 548 (1995).
- ⁶Yu. M. Gufan, V. P. Dmitriev, S. B. Roshal', and V. I. Snezhkov, *Landau Phases in Semiconductor Structures* [in Russian], Izd. Rostovskogo Universiteta, Rostov-on-Don (1990).
- ⁷H. M. Duh, I. S. Lyubutin, I. M. Jiang, G. H. Hwang, and K. D. Lain, *J. Magn. Magn. Mater.* **153**, 87 (1996).
- ⁸V. M. Fridkin, *Ferroelectric Semiconductors* [in Russian], Nauka, Moscow (1976).
- ⁹R. F. Mamin and G. B. Teitel'baum, *Fiz. Tverd. Tela (Leningrad)* **30**, 3536 (1988) [*Sov. Phys. Solid State* **30**, 2032 (1988)].
- ¹⁰G. Ya. Lyubarskiĭ, *Group Theory in Solid State Physics* [in Russian], Nauka, Moscow (1958).
- ¹¹D. V. Kovalev, *Irreducible and Induced Representations and Corepresentations of Fedorov Groups* [in Russian], Nauka, Moscow (1986).
- ¹²Yu. A. Izyumov, *Neutron Diffraction on Long-Period Structures* [in Russian], Énergoatomizdat, Moscow (1997).

- ¹³H. Poulet and J.-P. Mathieu, *Vibrational Spectra and Symmetry of Crystals*, Gordon and Breach, Paris (1970); Mir, Moscow (1973).
- ¹⁴H.-W. Streitwolf, *Group Theory in Solid State Physics* [MacDonald, London (1971); Mir, Moscow (1971)].
- ¹⁵V. A. Golovko, Zh. Éksp. Teor. Fiz. **94**, 182 (1988) [Sov. Phys. JETP **67**, 316 (1988)].

- ¹⁶B. R. Gadjiev, M.-G. Yu. Seidov, and V. R. Abdurakhmanov, Fiz. Tverd. Tela (St. Petersburg) **38**, 3 (1996) [Phys. Solid State **38**, 1 (1996)].
- ¹⁷B. R. Gadjiev, M.-G. Yu. Seidov, and V. R. Abdurakhmanov, Fiz. Nizk. Temp. **21**, 1241 (1995) [Low Temp. Phys. **21**, 950 (1995)].

Translated by Steve Torstveit

LOW-DIMENSIONAL AND DISORDERED SYSTEMS

Nature of critical current and coherent phenomena in granular MoN_x thin films

V. G. Prokhorov and G. G. Kaminsky

*Institute for Metal Physics, 36 Vernadsky Blvd., 03680 Kiev, Ukraine**

Y. P. Lee

Honyang University, Seoul, 133-791, Korea

I. I. Kravchenko

Department of Physics, University of Florida, Gainesville, FL 32611, USA

(Submitted March 27, 2000; revised May 11, 2000)

Fiz. Nizk. Temp. **26**, 1191–1196 (December 2000)

Investigations of the critical current versus temperature and applied magnetic field are carried out for granular MoN_x films. All samples display a two-stage superconducting transition and can be treated as a percolating network of SNS contacts with a Josephson coupling between grains. The temperature behavior of the critical current for the films studied is the same as the $I_c(T)$ dependence for a SNS junction in the diffusive limit. The value of critical current in a magnetic field is governed by the pinning of Josephson vortices. © 2000 American Institute of Physics. [S1063-777X(00)00312-1]

1. INTRODUCTION

The study of superconducting properties of nonuniform high-resistance films has attracted a great deal of attention recently due to the discovery of the superconductor-insulator transitional in two-dimensional (2D) systems.^{1–3} However, another remarkable feature of these materials is connected with the possibility of forming a regular granular structure. The interplay between microstructural disorder and spatial modulation of the superconducting order parameter allows us to treat these materials as a network of Josephson junctions that are very similar in Bi- and Tl-based anisotropic high- T_c superconductors.⁴ The granular nature of these objects clearly plays a major role in their superconductivity, and an understanding of the behavior of spatially nonuniform conventional superconductors is essential for establishing which properties of the cuprates might follow simply from their geometry and microstructural inhomogeneity. Even though the superconducting properties of granular films have been studied for a long time, the physical nature of this effect continues to be a matter of controversy.

In this paper we propose a new method for the preparation of granular MoN_x films, which can be treated as a percolating network of superconductor-normal metal-superconductor (SNS) contacts with a Josephson coupling between grains. The main peculiarity of the studied films is the occurrence of a two-stage transition from the normal to the long-range superconducting (coherent) state. It is shown that the observed linear dependence of the transition temperature to the phase-coherent state on the residual resistance can be explained in the framework of the proximity-effect model for the superconductor-normal metal (SN) system. The temperature behavior of the critical current I_c for the films studied is very similar to the $I_c(T)$ dependence obtained for a SNS

junction in the diffusive limit. The microscopic superconducting parameters estimated from fitting the experimental $I_c(T)$ curves coincide with ones obtained by independent methods. In contrast with $I_c(T)$, the magnetic field dependence of the critical current cannot be described on the basis of the theoretical models developed for single or multiple SNS junctions. We suggest that the transition of the MoN_x granular films to the resistive state under the action of current in an applied magnetic field results from the start of the flux lines' motion rather than from the switching of the Josephson junctions. Therefore the value of the critical current is determined by the pinning force of the Josephson vortices owing to the magnetic interaction with the grains.

2. EXPERIMENTAL PROCEDURE

The MoN_x films were prepared on Al₂O₃ substrates by thermal evaporation in a vacuum chamber with a base pressure of 6.7×10^{-4} Pa. A Mo strip (0.25 × 2 × 85 mm) was used for the evaporation. The deposition of the films was carried out with the following technological parameters. The current was about 50 A, the output power was ~50 W, the nitrogen pressure was around 10^{-3} Pa, and the substrate temperature during the deposition was ~350 K.

The deposited films have a thickness $d \approx 200$ nm. An x-ray diffraction analysis showed that a hexagonal MoN phase⁵ ($a = b \approx (0.572 \pm 0.001)$ nm, $c \approx (0.560 \pm 0.005)$ nm) is formed in about 90% of the film volume. On the other hand, the low value of the critical temperature T_c of 5.0–6.5 K shows that the prepared films have a nonstoichiometric concentration of nitrogen and their composition is represented as MoN_x. The average grain size estimated by high-resolution electron microscopy turned out to be $\langle D \rangle \approx 100$ nm. The geometric dimensions of the samples were set by a

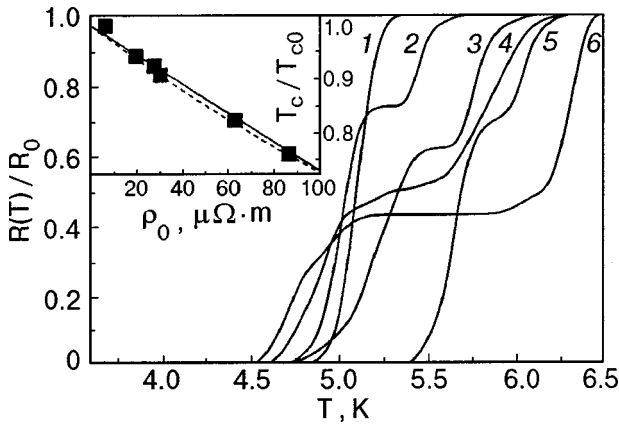


FIG. 1. Superconducting transition curves for MoN_x films with different values of the residual resistivity ρ_0 [$\mu\Omega\cdot\text{m}$]: 6.2 (1); 30.2 (2); 19.8 (3); 62.4 (4); 27.5 (5); 86.1 (6). The inset shows the dependence of the ratio T_c/T_{c0} on ρ_0 . The solid and dashed lines are theoretical curves obtained by using Eqs. (1) and (3), respectively.

photolithographic model to have a width of 0.325 mm and a length between voltage contacts of 3.65 mm. The resistance was measured by the conventional dc four-probe techniques. A voltage drop of 1 $\mu\text{V}/\text{cm}$ served as the criterion for choosing the critical current. The applied magnetic field was always maintained perpendicular to the film surface and to the direction of the transport current.

3. RESULTS AND DISCUSSION

Figure 1 shows the resistance curves of the superconducting transition for MoN_x films with different values of the residual resistivity ρ_0 measured at 10 K. It can be seen that all the films with $\rho_0 > 6.2 \mu\Omega\cdot\text{m}$ have a two-stepped shape of $R(T)/R_0$, where R_0 is the resistance before the superconducting transition. Therefore, the transition of the films to the superconducting state is carried out in two stages. The first superconducting state occurs inside the grains at a high temperature, T_{c0} , and a long-range phase-coherent superconducting state is formed at a lower temperature, T_c . Unfortunately, we have not observed any relation between the value of the residual resistance (or sheet resistance, $R_{\text{II}} = \rho_0/d$) and the temperature positions of the two superconducting transitions, such as is very often found in disordered thin films.^{6,7} However, the difference between the first and second resistance steps (T_{c0} and T_c) depends directly on the total resistivity of the film.

The disorder-induced depression of T_{c0} is in good qualitative agreement with the percolation description of a weakly coupled random 2D network of Josephson junctions. Using the theoretical results for a percolating network of Josephson-coupled grains, together with the temperature-dependent BCS energy gap, one can write⁷

$$\frac{T_c}{T_{c0}} = 1 - \frac{0.3e^2\rho_0}{\pi\hbar L}, \quad (1)$$

where T_{c0} is the superconducting transition temperature of the grain and T_c is the depressed transition temperature of the grain boundary as mentioned above; L is the characteristic length of the microstructure morphology (proportional to the grain size), and $\pi\hbar/4e^2 = 6.45 \text{ k}\Omega$ is the quantum of

resistance. A better agreement between the experimental and theoretical data is observed by fitting with $L \approx 25 \text{ nm}$, as is seen in the inset of Fig. 1. If it is assumed, according to Ref. 7, that $L \approx 0.3\langle D \rangle$, where $\langle D \rangle$ is the average grain size in the film, $\langle D \rangle$ turns out to be about 83 nm, which is of the same order of magnitude as the data obtained by electron-microscopic analysis. The observed linear dependence of the ratio T_c/T_{c0} on the residual resistance suggests that our samples are very similar to a composite In– InO_x film with an island microstructure.⁷

On the other hand, one can obtain a similar linear-like behavior of T_c/T_{c0} versus resistivity from Kresin's theoretical model⁸ of the proximity effect for strongly coupled superconductors. Let us consider the film as a SNS proximity sandwich system, where the grains are S and the grain boundaries N . If the thickness of the normal metal (the width of the grain boundaries) is smaller than the coherence length for the boundaries, the superconducting critical temperature for the whole SNS system can be described by⁹

$$T_c = T_{c0}(\pi T_{c0}/2\gamma u)^\alpha, \quad (2)$$

where $\alpha = n_N L_N / n_S L_S$, n_N and n_S are the electron density of states of the normal and superconducting layers, and L_N and L_S are the layer thicknesses, respectively. For a granular film L_N corresponds to the width w of the grain boundary, as mentioned, and L_S to the average grain size $\langle D \rangle$. In case of a nearly ideal SN contact, $u \approx \omega_c$, where ω_c is the average phonon frequency (equal to the Debye frequency in this model). $\gamma = 0.577$ is Euler's constant. Taking into account that the resistivity is inversely proportional to the electron density of states, $\rho = 1/(e\mathcal{D}n)$ where $\mathcal{D} = v_F^2\tau/3$ is the electron diffusion coefficient (v_F is the Fermi velocity and τ is the mean free time between collisions of electrons), Eq. (2) can be simplified to

$$\frac{T_c}{T_{c0}} \approx 1 + \frac{\rho_{0S}}{\rho_{0N}} \frac{w}{\langle D \rangle} \ln \left(\frac{2.72 T_{c0}}{w_c} \right), \quad (3)$$

where ρ_{0S} is the resistivity of the grains, and ρ_{0N} is that of the grain boundaries.

This equation is formally equivalent to Eq. (1), since the logarithmic term in Eq. (3) is negative in sign. The value of the electron diffusion coefficient is little different between grain and grain boundary in a covalent compound of the type considered, and $\ln x \approx x - 1$ when $x \ll 1$. If we also assume that the minimum metallic conductivity of the grain boundary is realized as $\sigma_{\text{min}} \approx 0.03e^2/\hbar a$ according to Mott and Koveh,¹⁰ we can estimate the value of $\rho_{0N} = \sigma_{\text{min}}^{-1} \approx 156 \mu\Omega\cdot\text{m}$, where a is the crystal lattice constant. With $\omega_c \approx 350 \text{ K}$ and $T_{c0} \approx 5 \text{ K}$ for our films,¹¹ the ratio of the grain boundary width to the average grain size, $w/\langle D \rangle$, is estimated to be about 0.1. Therefore, the average width of the grain boundaries turns out to be 10 nm in our case. This is an absolutely reasonable value for the films deposited at a low temperature. Consequently, the prepared MoN_x thin films can be treated as a percolating network of SNS contacts with a Josephson coupling between grains.

3.1. Temperature dependence of the critical current

Figure 2 shows the temperature dependence of the critical current for the MoN_x film with $\rho_0 = 30.2 \mu\Omega\cdot\text{m}$ at differ-

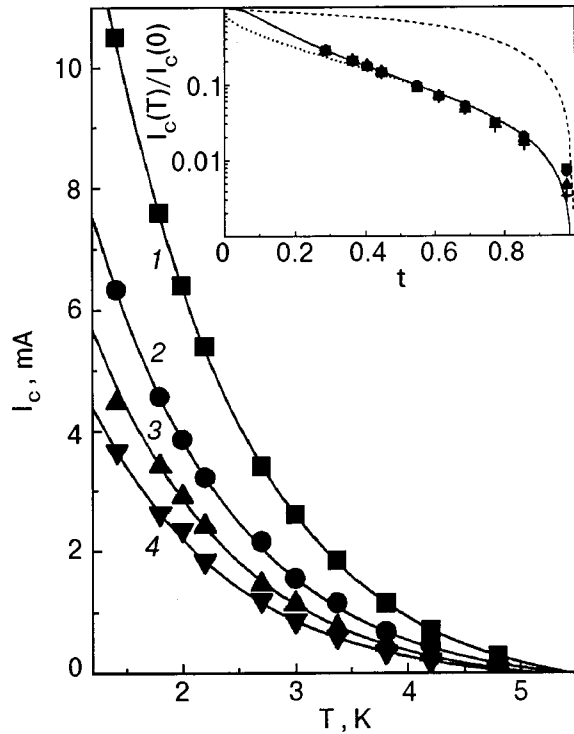


FIG. 2. Temperature dependence of the critical current for a MoN_x film with $\rho_0 = 30.2 \mu\Omega \cdot \text{m}$ at different values of applied magnetic field [T]: 0 (1); 0.1 (2); 0.2 (3); 0.3 (4). The inset shows the logarithmic dependence of $I_c(T)/I_c(0)$ on the reduced temperature $t = T/T_c$. The dashed line corresponds to the Ambegaokar–Baratoff expression, the solid line is calculated for the model of a SIS junction with a suppressed superconducting energy gap, and the dotted line corresponds to the model of a SNS junction in the diffusive limit.

ent values of applied magnetic field. The $I_c(T)$ behavior displays a fundamental deviation from the Ambegaokar–Baratoff (AB) expression developed for the case of the ideal superconductor–insulator–superconductor (SIS) Josephson junction, $I_c(T)R_N = \pi\Delta(T)/2 \tanh(\Delta(T)/2T)$.¹² R_N is the normal resistance of the junction, and $\Delta(T)$ is the superconducting energy gap. A better agreement between the experimental data and the AB model can be obtained by using a severely depressed value of the superconducting energy gap as a fitting parameter. The dashed line in the inset of Fig. 2 is plotted with a value of $\Delta(0) \approx 1.76k_B T_c$, while the solid line requires $\Delta(0) \approx 0.12k_B T_c$. It is worthy of note that the decrease in the energy gap of the Josephson junctions has already been observed experimentally. For example, the energy gap obtained for high- T_c layered superconductors from measurements of the intrinsic Josephson effect¹³ is about a factor of two smaller than that determined from tunneling¹⁴ or spectroscopy¹⁵ measurements. However, even though such an energy gap suppression is predicted in the theoretical works,^{16,17} this problem is far from being totally understood. On the other hand, the small value of the energy gap suggests that the transition temperature for the phase-coherent superconducting state (the second step on the resistance curves in Fig. 1) is lower than T_{c0} , an effect which has not been observed experimentally. We are proposing that the strong deviation of the experimental data from the AB expression in our case results from another physical cause.

Taking into account the good agreement between the

experimental dependence of T_c/T_{c0} on ρ_0 and Kresin's model⁹ for the SN proximity sandwich, we expect that the temperature behavior of the critical current of the films can be described in the framework of the approaches for SNS-type Josephson junctions.^{18–20} The critical current is written as

$$I_c(T) = AI_c(0) \exp\left(-\frac{L_N}{\xi_N}\right), \quad (4)$$

where $I_c(0)$ is the critical current at zero temperature, and $A \approx 12/\pi$ for $T \ll T_c$ and $A \approx 1 - T/T_c$ at $T \rightarrow T_c$. For the normal layer in a SNS system, ξ_0 is replaced by the normal metal coherence length, $\xi_N = \hbar v_F / 2\pi k_B T$ (in the ballistic limit $L_N \ll l$, where l is the impurity scattering length) or $\sqrt{\hbar \mathcal{D} / 2\pi k_B T}$ (in the diffusive limit $L_N \gg l$). Because the resistance of the grain boundary is larger than that of the grain itself, it is reasonable to assume the diffusive limit for our case. Using the well-known expression for the superconductor coherence length, $\xi(0) = (\xi_0 l)^{1/2}$, where $\xi_0 = 0.18\hbar v_F / k_B T_c$, one can write Eq. (4) in a form that is more convenient for fitting the experimental data:

$$\frac{I_c(T)}{I_c(0)} \approx \left(1 - \frac{T}{T_c}\right) \exp\left(-\frac{0.57L_N}{\xi(0)} \left(\frac{T}{T_c}\right)^{1/2}\right). \quad (5)$$

It is seen in the inset of Fig. 2 that better agreement with the experimental data is provided with $L_N/\xi(0) \approx 2.5$. In our case $L_N = w$, the width of grain boundary. Therefore, the value of the coherence length estimated from the temperature dependence of the critical current is equal to $\xi(0) \approx 4 \text{ nm}$. This is in the same order of magnitude as the value calculated from the expression for upper critical magnetic field, $H_{c2}(0) = \phi_0 / 2\pi \xi^2(0) \approx 0.69(dH_{c2}/dT|_{T_c})T_c$, where ϕ_0 is the magnetic flux quantum ($2.07 \times 10^{-15} \text{ T} \cdot \text{m}^2$). The measured value of $dH_{c2}/dT|_{T_c}$ for our films was $\approx 3\text{--}3.5 \text{ T/K}$, leading to $\xi(0) \approx 6\text{--}7 \text{ nm}$.

3.2. Magnetic-field dependence of the critical current

It is well known that in a SIS system, the Josephson current as a function of magnetic field shows a Fraunhofer pattern.²¹ However, in the case of a Josephson medium consisting of SNS junctions in which N is a 2D normal metal on the mesoscopic scale, the dependence of the Josephson current on magnetic field is expected to be not so simple. The Fraunhofer oscillations of the critical current have not been observed even in the stacked intrinsic Josephson junctions of $\text{Bi}_2\text{Sr}_2\text{CaCu}_2\text{O}_{8+\delta}$ layered high- T_c single crystals.^{4,22} Figure 3 shows the $I_c(B)$ difference for the MoN_x film measured at different temperatures, which does not display any manifestation of oscillatory behavior.

Two theoretical approaches have been used for explanation of the magnetic-field dependence of the critical current in spatially nonuniform superconductors connected in a system of Josephson junctions. The first of them is based on the solution of a Hamiltonian that is formally the same as for an XY disordered ferromagnet in 3D.^{23,24} The second one suggests the pinning of the Josephson vortices by microstruc-

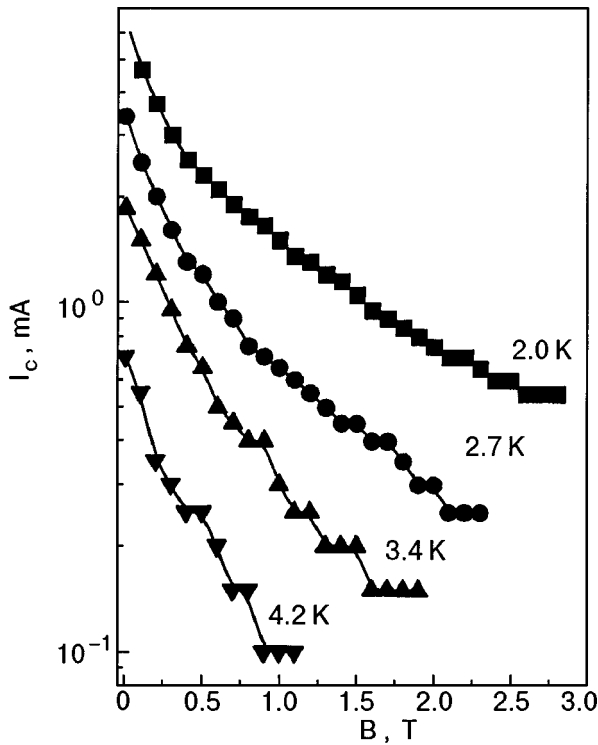


FIG. 3. Dependence of the critical current on applied magnetic field for a MoN_x film with $\rho_0=30.2 \mu\Omega\cdot\text{m}$ at different temperatures.

tural inhomogeneities, and the value of the critical current is determined by the driving force necessary for flux line motion.^{25,26}

For the system of a Josephson junction network, the magnetic field dependence of the critical current can be described by²³

$$I_c(B)/I_c(0) \approx 0.82(1 - \gamma_S^{-1} \sin \gamma_S)^{1/2} B_0/B, \quad (6)$$

$$\gamma_S = 2.7(\Lambda/\lambda_c)(B/B_0),$$

where B_0 is the first critical magnetic field, and Λ and λ_c can be treated as a correlation length for the phase-coupled junctions and a penetration depth, respectively. Unfortunately, Eq. (6) is not able to describe well the experimental $I_c(B)$, especially in the low magnetic field range, as seen in Fig. 4. Moreover, the fitting parameter obtained, $B_0 \approx 0.25$ T, is too large for our films.

Because of the growth mechanism and the tendency to form the so-called columnar texture of the grains, the grain boundaries of the prepared MoN_x films are arranged perpendicularly to the plane of the substrate. Consequently, a 2D network of Josephson junctions (grain boundaries) with a 2D array of Josephson vortices can be formed. The rather small size of the grains ($\langle D \rangle \ll \lambda_J$), where $\lambda_J = (\phi_0/2\pi\mu_0 j_c t)^{1/2} \approx 10 \mu\text{m}$ in our case is the Josephson penetration depth, allows us to assume that the interaction between Josephson vortices leads to the formation of a flux-line lattice. The dynamics of such a system can be described by the pinning theory. Since the Josephson vortices do not have normal cores, in contrast to the Abrikosov vortices, the mechanism of the flux-line pinning is governed by the magnetic interaction, and the grains play the role of the pinning centers. In this case the critical current is expressed by $I_c(B)$

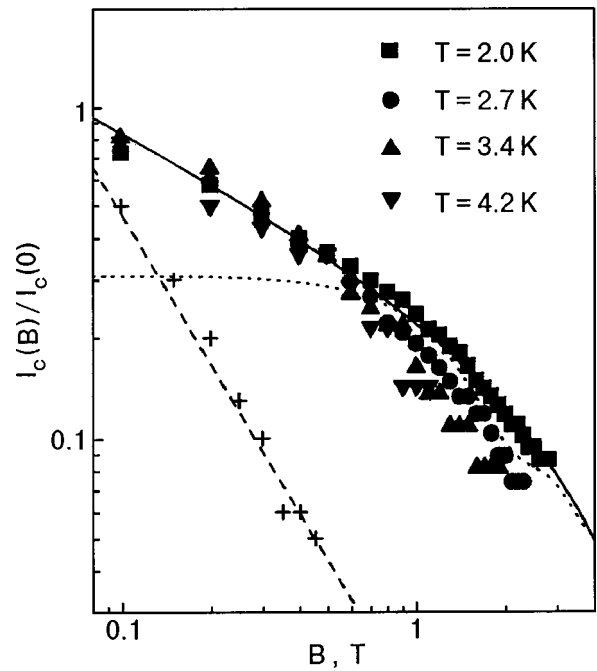


FIG. 4. Dependence of $I_c(B)/I_c(0)$ on applied magnetic field for a MoN_x film with $\rho_0=30.2 \mu\Omega\cdot\text{m}$. The solid line is the theoretical curve based on the Josephson vortex pinning model, the dotted line corresponds to the XY model, and the dashed line indicates the dependence $I_c \sim 1/B^{1.5}$. The cross symbols represent the experimental data for the intrinsic Josephson junctions of Bi₄Sr₂CaCu₂O_{8- δ} from Ref. 4.

$= 2cM\phi_0^{1/2}/\lambda B^{1/2}$, where the magnetization of $M \approx (H_{c2} - B)/[4\pi(2\kappa^2 - 1)]$; λ is the London penetration depth, and κ is the Ginzburg–Landau parameter.²⁷ Taking into account that the elementary pinning force has to decrease proportionally to the drop in the order parameter according to the rise of the field,²⁷ the final expression for $I_c(B)$ is simplified to

$$\frac{I_c(B)}{I_c(0)} \approx \frac{4\pi}{\kappa d} \left(\frac{\phi_0}{B}\right)^{1/2} \left(1 - \frac{B}{H_{c2}}\right)^2. \quad (7)$$

Figure 4 shows that the theoretical curve is in good agreement with the experimental data practically in the whole range of magnetic fields. A fitting to the experiment allows us to estimate the values of the Ginzburg–Landau parameter, $\kappa \approx 70$, and the upper critical field, $H_{c2} \approx 10$ T, which coincide with those obtained from an analysis of the $(dH_{c2}/dT)|_{T_c}$ data for these films.

For comparison, we also show in Fig. 4 the experimental results for the stacked intrinsic Josephson junctions of a Bi₂Sr₂CaCu₂O_{8+ δ} single crystal.²² It is seen that the magnetic field behavior of the critical current is described by a power law ($I_c \sim 1/B^{1.5}$), as well. However, the pinning mechanism has a more exotic nature and is connected with the collective pinning phenomenon.²⁶

SUMMARY

We have developed a new method for the preparation of granular MoN_x films that can be treated as a 2D network of SNS Josephson junctions. It was shown that the temperature dependence of the critical current can be described in the framework of the SNS junction model in the diffusive limit. For an explanation of the superconducting transport proper-

ties in an applied magnetic field, a simple model for the magnetic pinning of the Josephson vortices is suggested, where the grains play the role of the pinning centers.

This work was supported by the Science and Technology Center in Ukraine through Project No. 1455, and by the Korea Research Foundation through the BSRI program (1998-015-D00087).

*E-mail: pug@imp.kiev.ua

-
- ¹A. M. Goldman and N. Marković, *Phys. Today* **51**, 39 (1998).
²A. F. Hebard and M. A. Paalanen, *Phys. Rev. Lett.* **65**, 927 (1990).
³S. Tanda, S. Ohzeki, and T. Nakayama, *Phys. Rev. Lett.* **69**, 530 (1992).
⁴A. Yurgens, D. Winkler, T. Claeson, G. Yang, I. F. G. Parker, and C. E. Gough, *Phys. Rev. B* **59**, 7196 (1999).
⁵S. L. Roberson, D. Finello, and R. F. Davis, *Thin Solid Films* **324**, 30 (1998).
⁶I. A. Parshin, I. L. Landau, and L. Rinderer, *Phys. Rev. B* **54**, 1308 (1996).
⁷A. F. Hebard and A. T. Fiory, *Phys. Rev. Lett.* **58**, 1131 (1987).
⁸V. Kresin, *Phys. Rev. B* **25**, 157 (1982).
⁹V. Z. Kresin, A. Bill, S. A. Wolf, and Yu. N. Ovchinnikov, *Phys. Rev. B* **56**, 107 (1997).
¹⁰N. F. Mott and M. Koveh, *Adv. Phys.* **34**, 329 (1985).
¹¹V. G. Prokhorov, *Fiz. Nizk. Temp.* **24**, 544 (1998) [*Low Temp. Phys.* **24**, 410 (1998)].
¹²V. Ambegaokar and A. Baratoff, *Phys. Rev. Lett.* **10**, 486 (1963); **11**, 104 (1963).

- ¹³A. Yurgens, D. Winkler, N. V. Zavaritsky, and T. Claeson, *Phys. Rev. B* **53**, R8887 (1996).
¹⁴K. Kitazawa, *Science* **271**, 313 (1996).
¹⁵A. G. Loeser, Z.-X. Shen, D. S. Dessau, D. S. Marshall, C. H. Park, P. Fournier, and A. Kapitulnik, *Science* **273**, 325 (1996).
¹⁶X.-J. Fan, G. Li, and X.-G. Li, *Physica C* **311**, 93 (1999).
¹⁷R. A. Klemm, C. T. Rieck, and K. Scharberg, *Phys. Rev. B* **58**, 1051 (1998).
¹⁸K. K. Likharev, *Rev. Mod. Phys.* **51**, 101 (1979).
¹⁹U. Lederhann, A. L. Fauchere, and G. Blatter, *Phys. Rev. B* **59**, R9027 (1999).
²⁰P. W. Brouwer and C. W. J. Beenakker, *Chaos, Solitons Fractals* **8**, 1249 (1997).
²¹M. Tinkham, *Introduction to Superconductivity*, McGraw-Hill, New York (1975).
²²V. M. Krasnov, N. Mros, A. Yurgens, and D. Winkler, *Physica C* **304**, 172 (1998).
²³C. Lebeau, A. Raboutou, P. Peyral, and J. Rosenblatt, *Physica B* **152**, 100 (1988).
²⁴J. Rosenblatt, A. Raboutou, P. Peyral, and C. Lebeau, *Rev. Phys. Appl.* **25**, 73 (1990).
²⁵J. R. Phillips, H. S. J. Van der Zant, J. White, and T. P. Orlando, *Phys. Rev. B* **47**, 5219 (1993).
²⁶L. N. Bulaevskii, D. Dommgues, M. P. Maley, A. R. Bishop, and B. I. Ivlev, *Phys. Rev. B* **53**, 14601 (1996).
²⁷A. Campbell and J. Evetts, *Critical Current in Superconductors*, Taylor and Francis, London (1972).

This article was published in English in the original Russian journal. Reproduced here with stylistic changes by the Translation Consultant.

On the theory of carrier-induced ferromagnetism in diluted magnetic semiconductors

Yu. G. Semenov

Institute of Semiconductor Physics, National Academy of Sciences of Ukraine, Prospect Nauki 45, Kiev, 03028, Ukraine

S. M. Ryabchenko*

Institute of Physics, National Academy of Sciences of Ukraine, Prospect Nauki 46, Kiev, 03028, Ukraine

(Submitted May 15, 2000)

Fiz. Nizk. Temp. **26**, 1197–1201 (December 2000)

Two different approaches (presented in the literature as alternative approximations) to the problem of carrier-induced ferromagnetism in the system of disordered magnetic ions of a diluted magnetic semiconductor are analyzed. They are based on a self-consistent procedure for the mean exchange fields and the RKKY interaction. Calculations in the framework of an exactly solvable model are carried out, and it is shown that these approaches stem from two different contributions to the magnetic susceptibility. One stems from the diagonal part of the carrier-ion exchange interaction and corresponds to the mean field approximation. The other one stems from the off-diagonal part of the same interaction and describes the indirect interaction between localized spins via free carriers. These two contributions can give rise to different magnetic properties. Thus the aforementioned contributions are complementary and not alternative to each other. A general approach is proposed and compared with different approximations to the problem under consideration. © 2000 American Institute of Physics. [S1063-777X(00)00412-6]

INTRODUCTION

In recent years there has been a substantial increase of interest in studies of carrier-induced ferromagnetism in diluted magnetic semiconductors (DMSs). A number of works (see Ref. 1 and references therein) present proof of the existence of a ferromagnetic transition in the DMS $\text{Pb}_{1-x-y}\text{Sn}_y\text{Mn}_x\text{Te}$, induced by the strong exchange interaction of the Mn ions with band holes. A ferromagnetic phase transition has also been found in *p*-doped DMS quantum wells.² Carrier-induced ferromagnetism was observed in the DMS $(\text{Ga}_{1-x}\text{Mn}_x)\text{As}$ with *x* of a few percent, where holes are associated with the Mn ions in these structures.³

To describe the transition to a ferromagnetic (FM) phase induced by free carriers, all of the authors of the aforementioned works used similar approaches: the role of band carriers was reduced to the induction of indirect interaction between localized spins through electrons (holes) (LeL interaction), known in the physics of metals as the RKKY (Ruderman–Kittel–Kasuya–Yosida) interaction.⁴ The magnetic ions were considered as a subsystem separated from the electrons (holes) because of a small free-carrier contribution to the total magnetization of the system. A consideration of magnetic ions with the RKKY interaction in terms of the Curie–Weiss field permits one to incorporate in it the spin–spin interactions caused by other mechanisms (LL interaction). The latter mechanisms are assumed to result in a temperature shift Θ_{LL} in the Curie law for the magnetic susceptibility without free carriers, $\chi^{-1} \propto T - \Theta_{\text{LL}}$. Thus, the electrons (holes) change this dependence by the additional shift Θ_{LeL} (Ref. 1):

$$\chi^{-1} \propto T - \Theta_{\text{LL}} - \Theta_{\text{LeL}}. \quad (1)$$

Since for Mn-based DMSs $\Theta_{\text{LL}} < 0$ while $\Theta_{\text{LeL}} > 0$, the FM phase transition can take place if $\Theta_{\text{LeL}} > |\Theta_{\text{LL}}|$.

Another approach to the problem under consideration was developed in Refs. 5 and 6, where the carrier-ion exchange interaction was treated in terms of a self-consistent mean field approximation (MFA). The indirect LeL interaction does not appear in this approach, but the free-carrier contribution to the thermodynamic potentials was taken into account in the MFA. As a result, this theory predicts a temperature shift Θ_{MF} in the Curie law:

$$\chi^{-1} \propto T - \Theta_{\text{LL}} - \Theta_{\text{MF}}. \quad (2)$$

Now we would like to emphasize that the values calculated for the temperature shifts Θ_{LeL} and Θ_{MF} under some additional (but common enough) assumptions coincide with each other for 3D, 2D, and 1D electron gases.² This coincidence can lead to the spurious conclusion that the MFA and LeL (or RKKY) interaction considered in the Curie–Weiss field approximation are of an identical nature. This paper draws attention to the fact that free carriers still cause a significant contribution to the thermodynamic potentials even after the LeL interaction is taken into account. This contribution treated in the MFA is not identical to the LeL (or RKKY) interaction. This last statement becomes clear if we take into account that the LeL (RKKY) interaction appears after partial diagonalization of the interaction Hamiltonian with respect to space quantum numbers (the electron wave vectors \mathbf{k} in the case of the RKKY interaction), while the MFA approach^{5,6} uses only the diagonal part of the interaction and therefore does not depend on the spatial configuration of the magnetic ions. It is therefore possible to imagine a physical situation in which the MFA contribution exceeds

the RKKY contribution to the magnetic susceptibility. Thus the main result we want to prove below can be reduced to the statement that, generally speaking, the static magnetic susceptibility depends significantly on both Θ_{MF} and Θ_{LeL} .

The structure of the paper is following. First we illustrate our approach with a model allowing exact statistical calculations. Then we consider a more realistic system that is related to the experimental situation in Refs. 1–3. We conclude with a discussion of the general approach to the FM phase transitions in DMSs and compare our approach with the works devoted to this problem.

MAGNETIC SUSCEPTIBILITY IN EXACTLY SOLVABLE MODEL

The Hamiltonian of our model is similar to that applied in the aforementioned works and comprises a sum of localized spin moments (LSMs), electrons, and their interaction Hamiltonians:

$$H = H_m + H_e + H_{em}, \quad (3)$$

where

$$H_m = g_m \mu_B B \sum_j S_Z^j \equiv \omega_m M_L;$$

$$H_e = \sum_{b,k,\sigma} (\varepsilon_b + \omega_e \sigma) a_{b,k,\sigma}^+ a_{b,k,\sigma};$$

$$H_{em} = -(J/N_0) \sum_{b,b',k,\sigma} A_{b,b'} (\sigma M) a_{b,k,\sigma}^+ a_{b',k,\sigma}.$$

Here S_Z^j is the Z component of the j th LSM spin, while $M_L = \sum_j S_Z^j$, $j=1, \dots, N_m$; N_m is the number of LSMs in the system; g_m and $\omega_m = g_m \mu_B B$ are, respectively, the LSM g factor and Zeeman splitting in the field B ; ω_e is band electron Zeeman splitting in the field B . Three quantum numbers can be assigned to the electrons: band number b , intraband quantum number k , and spin projection $\sigma = \pm 1/2$; $a_{b,k,\sigma}^+$ and $a_{b,k,\sigma}$ are the creation and annihilation operators; J is the carrier–ion exchange interaction constant; the normalization factor N_0 equals one-half of the number of electronic states in each of bands b , and $A_{b,b'}$ is an interband transition matrix element.

The structure of Hamiltonian (3) is similar to that in Refs. 1–3 and 6. The differences lie both in the dispersion of the band carriers, $\varepsilon_{b,k} = \varepsilon_{b',k}$, which corresponds to flat bands, and in the lack of intraband exchange scattering. The exchange scattering between bands b and b' is taken into account by the matrix element $A_{b,b'}$.

If we restrict ourselves to only two electronic bands $b = 1, 2$, the diagonalization of the Hamiltonian becomes trivial. The eigenenergies E are determined by the repopulating of electrons within bands $b=1$ and 2 as well as by the normalized values of the ion spin projections $\mu = M_L/N_m$. For simplicity we assume $A_{b,b'} = 1$. Thus the energy per unit volume reads:

$$E_b = n_b (\varepsilon_1 + \varepsilon_2) / 2 + (G_L + \omega_e) (n_{b+} - n_{b-}) \pm (n_b \Delta E / 2) \times \left[1 + \left(\frac{G_L}{\Delta E} \right)^2 \right]^{1/2} + \omega_m n_m \mu. \quad (4)$$

The minus and plus signs correspond to $b=1$ and $b=2$; ΔE is the energy interval between these bands; n_{b+} and n_{b-} are the concentrations of electrons with spin projection $\sigma = +1/2$ and $-1/2$ in the band b , the total electron concentra-

tion is $n_b = n_{b+} + n_{b-}$; $G_L = Jx\mu$ is the effective exchange field of magnetic ions acting on electrons, $x = N_m/N_0$ is the fraction of magnetic cations in the crystal, n_m and N_m are their concentration and total number, and N_0 is the total number of cations in the crystal.

Since value of G_L is infinitesimal at $T > T_c$ (T_c is the FM phase transition temperature) and $B \rightarrow 0$, the square root in Eq. (4) can be expanded in the small parameter $(G_L/\Delta E)^2$ up to the first nonvanishing term. We will also assume that only the lowest energy band $b=1$ is filled, i.e., $\Delta E \gg kT$. Then the energy spectrum assumes the following form:

$$E = n_e \varepsilon_1 + n_e G_L \sigma_e + \omega_m n_m \mu - n_e G_L^2 / (4\Delta E). \quad (5)$$

For brevity, we introduce the total concentration of electrons $n_e = n_{b=1}$ and the average projection of electronic spins $\sigma_e = (n^+ - n^-) / (n^+ + n^-)$; the electronic g factor is assumed to be equal to zero.

There are two possible courses of further action. The first one (following Refs. 1–3) is to restrict consideration to the magnetic ions only. This restriction means consideration of only the last two terms in Eq. (5). The second way^{5,6} is to consider only the first three terms. Note that last term in Eq. (5) is just the contribution to the energy from the LeL spin–spin interaction induced by the band electrons, because $G_L^2 \propto \sum_{jj'} S_Z^j S_Z^{j'}$, while all the rest of the terms are due to the electron and LSM energies with the diagonal part of their interaction. We consider a third approach that takes into account the full energy of the system (5).

For magnetic susceptibility calculations we need the partition function. This function has the form

$$Z = \int \int U_{N_m}(M_L) U_{N_e}(M_B) e^{-E/kT} dM_B dM_L, \quad (6)$$

and can be immediately calculated with the help of Eq. (5). The projections of the total LSM spins $M_L = N_m \mu$ and the band electrons $M_B = N_e \sigma_e$ are introduced in Eq. (6). Beyond magnetic saturation, the statistical weight $U_N(M)$ is given by a Gaussian distribution in the thermodynamic limit $N_m \rightarrow \infty$, $N_e \rightarrow \infty$ (Ref. 7):

$$U_N(M) = \frac{(2S+1)^N}{(\pi \Delta_S)^{1/2}} e^{(M^2/\Delta_S)}, \quad (7)$$

where $\Delta_S = 2/3S(S+1)N$. Equation (7) is also applicable for band electrons with $S=1/2$ if the electrons obey Boltzmann statistics. Such an approach is evidently realized in the limit $N_e \ll N_0$. Thus, the partition function Z is calculated by straightforward integration in Eq. (6) with the aforementioned assumptions. After some algebra we arrive at the following final result:

$$\chi_0^{-1} = \chi_{0,L}^{-1} \left(1 - \frac{\Theta_{LeL}}{T} - \frac{\Theta_{MF}^2}{T^2} \right)$$

with

$$\Theta_{LeL} = \frac{1}{6} S(S+1) \frac{J^2 x^2 N_e}{\Delta E N_m};$$

$$\Theta_{MF} = \left[\frac{1}{12} S(S+1) J^2 \Omega_0^2 n_m n_e \right]^{1/2}, \quad (8)$$

where $\chi_{0,L} = 2/3S(S+1)(g\mu_B)^2 n_m/T$ is the paramagnetic susceptibility of noninteracting LSMs, and Ω_0 is the volume of the unit cell.

Calculations in the framework of the approach of Refs. 1–3 reproduce the result (8) but without the last term $(\Theta_{MF}/T)^2$. This term appears as a contribution of free carriers to the thermodynamic potential due to the diagonal part of the carrier–ion exchange interaction H_{em} (3). One can see that the diagonalization procedure does not remove this term, and therefore the LeL interaction can never take it into account.

Another approach^{5,6} treats the interaction H_{em} in the first order of perturbation theory only. As a result, the last term in Eq. (5) does not appear, and therefore $\Theta_{LeL} = 0$ in Eq. (8) for our model. It is interesting to note that, in spite of the extreme simplicity of the model under consideration, the expression for Θ_{MF} in Eq. (8) reproduces the result of Ref. 6 obtained in terms of self-consistent exchange fields for a more realistic situation.

One can see that expression (8) for Θ_{MF} is neither quantitatively nor qualitatively similar to Θ_{LeL} . It permits one to make the following general statement. For problems of magnetic phase transitions, magnetic susceptibility, magnetization, etc., it is important to simultaneously take into account the contributions of both the magnetic ions and electron subsystems to the thermodynamic potentials despite the negligible magnetization of the free carriers. In doing so, it is also important to take into account both the diagonal and off-diagonal parts of the carrier–ion exchange interaction. The omission of any of the aforementioned terms in the Hamiltonian leads, generally speaking, to significant inaccuracy or even to qualitative changes.

GENERAL APPROACH TO CALCULATION OF CRITICAL TEMPERATURE

We now present a correct consideration of the problem of spontaneous magnetic transitions induced by band carriers in DMSs. We choose the Hamiltonian in a form similar to (3) but incorporate the LL spin–spin interaction H_{LL} between the LSM in the magnetic part H_m and the intraband exchange scattering between Bloch electron states in the interaction H_{em} (Ref. 8). In such a case the intraband exchange scattering generates the LeL interaction. To calculate the magnetic susceptibility with the help of the modified Hamiltonian (3), we shall carry out the approximate diagonalization of Eq. (3) by elimination of its off-diagonal (in \mathbf{k} and \mathbf{k}') components by the canonical transformation method⁹ in the second order of perturbation theory. As a result, the effective LeL spin–spin interaction operator assumes the form

$$H_{LeL} = \sum_{j,j'} J_{\text{eff}}(\mathbf{R}_{j,j'}) S^j \cdot S^{j'}, \quad (9)$$

where $\mathbf{R}_{j,j'}$ is the radius vector joining the pairs of magnetic ions at the crystal lattice sites j and j' . The structure of the indirect interaction (9) is similar to the Hamiltonian H_{LL} , so they can be combined. The specific form of $J_{\text{eff}}(\mathbf{R}_{j,j'})$ in Eq. (9) depends on the degeneracy of the electron gas,¹⁰ the influence of magnetic field,¹¹ the effect of casual anisotropy,¹² the structure of the energy band of the semiconductor,¹ and the dimensionality of the system.²

Then the diagonal part of the operator H_{em} should be written in the form of the Zeeman energy of the LSMs in the effective field $B_e = J\Omega_0\sigma_e/g_m\mu_B$ and added to the Zeeman term of the magnetic Hamiltonian H_m . We should emphasize here that B_e is similar to the Knight field in nuclear magnetism. The LSM g -factor shift induced by the field B_e has recently been observed in DMSs.¹³

One more standard step is the transformation of the spin–spin interactions in H_m to the energy in the Curie–Weiss fields. It is well known that such an approach reduces the thermodynamical treatment of interacting spins to consideration of isolated spins with an effective temperature $T_{\text{eff}} = T - \Theta$. The parameter $\Theta = \Theta_{LL} + \Theta_{LeL}$ is determined by both the LL and the LeL interactions [Eq. (9)].

As a result, the free energy can be presented in terms of the electronic and ionic parts only:¹⁴

$$F = F_e(\sigma_e) + F_m(B + J\Omega_0\sigma_e/g_m\mu_B, T - \Theta), \quad (10)$$

where $F_m(B + B_e, T - \Theta)$ is the contribution of noninteracting (isolated) spins subjected to the uniform magnetic field $B + B_e$ at the temperature $T - \Theta$. Note that Eq. (10) takes into account both diagonal (the term $B_e = J\Omega_0\sigma_e/g_m\mu_B$) and off-diagonal (the term Θ_{LeL}) parts of the carrier–ion exchange interaction. The electronic spin polarization σ_e is found by minimization of the functional (10). Then, substitution of the expression for σ_e obtained in this manner into Eq. (10) completely determines the thermodynamic characteristics of the system: the magnetization $M_\alpha = -\partial F/\partial B_\alpha$; magnetic susceptibility $\chi_{\alpha,\alpha} = -\partial^2 F/\partial B_\alpha^2$, $\alpha = x, y, z$; and the temperature of the magnetic phase transition T_c .

The specific form of the free energy functional (10) depends on the aforementioned and many other peculiarities of our system. As an illustration, we consider now the most popular case of a degenerate electron gas in a simple isotropic and of a semiconductor. We consider the magnetic transition temperature T_c on the basis of the previous results.^{1–3,6} Equation (10) permits one to obtain the following equation for the critical temperature point:

$$(T_{\text{eff}})_c - \Theta_{MF} = 0. \quad (11)$$

Here Θ_{MF} is given by the corresponding formulas of Refs. 2 and 6 and $(T_{\text{eff}})_c = T_c - \Theta_{LL} - \Theta_{RKKY}$, where $\Theta_{LeL} = \Theta_{RKKY}$ for the specific case considered. The parameter Θ_{RKKY} coincides with Θ_{MF} only under the assumptions mentioned in the introduction to this paper. The parameter Θ_{LL} should be taken from experiment, $\Theta_{LL} = -T_0$, where $T_0 > 0$ corresponds to the antiferromagnetic LL exchange interaction realized in the majority of experimental situations for DMSs (see Ref. 15 and references therein). We can thus obtain $T_c = 2\Theta_{MF} - T_0$. If one takes into account only self-consistent exchange mean fields or RKKY interactions, the value of T_c is determined by a different expression: $T_c = \Theta_{MF} - T_0$. This difference can be important in the prediction of conditions for the realization of carrier-induced ferromagnetism in different experimental situations.

CONCLUSION

We have shown that neglecting the electronic contribution to the free energy (10) leads to a substantial lowering of the predicted T_c value despite the consideration of the indi-

rect interaction via free carriers. Moreover, the example considered shows that such neglect can lead to qualitatively different results in some cases. The present work also shows that different parts of the interaction operator are responsible for different mechanisms of FM ordering in DMS. Therefore, both diagonal and off-diagonal (in \mathbf{k}) parts of the carrier–ion exchange interaction are important. Nevertheless, the main conclusion of previous works remains valid: carrier-induced FM transition in DMS is possible at high enough carrier concentrations, and reduction of the dimensionality of the system enhances this effect.

This paper was partially supported by Ukrainian Fundamental Research Foundation Grant No. 4/871.

*E-mail: ryabch@iop.kiev.ua

¹T. Story, R. R. Galazka, R. B. Frankel, and P. A. Wolff, Phys. Rev. Lett. **56**, 777 (1986); M. Z. Cieplak, A. Sienkiewicz, Z. Wilamowski, and T. Story, Acta Phys. Pol. A **69**, 1011 (1986); T. Story, G. Karczewski, L. Swierkowski, and R. R. Galazka, Phys. Rev. B **42**, 10477 (1990); T. Story, P. J. T. Eggenkamp, C. H. W. Swuste, H. J. M. Swagten, W. M. J. de Jonge, and A. Szczerbakow, Phys. Rev. B **47**, 227 (1993).

²A. Haury, A. Wasiela, A. Arnoult, J. Cibert, S. Tatarenko, T. Dietl, and Y. Merle d'Aubigny, Phys. Rev. Lett. **79**, 511 (1997); T. Dietl, A. Haury, and Y. Merle d'Aubigny, Phys. Rev. B **55**, R3347 (1997).

³F. Matsukura, H. Ohno, A. Shen, and Y. Sugawara, Phys. Rev. B **57**, R2037 (1998).

⁴M. A. Ruderman and C. Kittel, Phys. Rev. **96**, 99 (1954); T. Kasuya, Prog. Theor. Phys. **16**, 45 (1956); K. Yosida, Phys. Rev. **106**, 893 (1957).

⁵A. A. Abrikosov, Zh. Éksp. Teor. Fiz. **65**, 814 (1973) [Sov. Phys. JETP **38**, 403 (1974)].

⁶E. A. Pashitskij and S. M. Ryabchenko, Fiz. Tverd. Tela (Leningrad) **21**, 545 (1979) [Sov. Phys. Solid State **21**, 322 (1979)].

⁷S. M. Ryabchenko and Yu. G. Semenov, Zh. Éksp. Teor. Fiz. **84**, 1419 (1983) [Sov. Phys. JETP **57**, 825 (1983)].

⁸Yu. G. Semenov and B. D. Shanina, Phys. Status Solidi B **104**, 631 (1981).

⁹G. L. Bir and G. E. Picus, *Symmetry and Strain-Induced Effects in Semiconductors*, Wiley, New York (1972).

¹⁰B. I. Kochelaev, Fiz. Tverd. Tela (Leningrad) **7**, 2859 (1965) [Sov. Phys. Solid State **7**, 2315 (1966)].

¹¹B. M. Khabibulin, Zh. Éksp. Teor. Fiz. **57**, 1605 (1969) [Sov. Phys. JETP **30**, 868 (1970)].

¹²N. P. Il'in and I. Ya. Korenblit, Zh. Éksp. Teor. Fiz. **81**, 2070 (1981) [Sov. Phys. JETP **54**, 1100 (1981)].

¹³T. Story, C. H. W. Swuste, P. J. T. Eggenkamp, H. J. M. Swagten, W. J. M. de Jonge, and A. Szczerbakow, Phys. Rev. Lett. **77**, 2802 (1996).

¹⁴Yu. G. Semenov and V. N. Sokolov, *Report on the Grant No. 2/276-93 of Fundamental Research Foundation of Ukraine* (1993) (unpublished).

¹⁵J. A. Gaj, W. Greishaber, C. Boden-Deshayes, J. Cibert, G. Feillrt, Y. Merle d'Aubigny, and A. Waseila, Phys. Rev. B **50**, 5512 (1994).

This article was published in English in the original Russian journal. Reproduced here with stylistic changes by the Translation Consultant.

Temperature dependence of the electron–phonon scattering time of charge carriers in *p*-Si/SiGe heterojunctions

V. V. Andrievskii, I. B. Berkutov, and Yu. F. Komnik*

B. Verkin Institute for Low Temperature Physics and Engineering, National Academy of Sciences of Ukraine, pr. Lenina 47, 61164 Kharkov, Ukraine

O. A. Mironov and T. E. Whall

Department of Physics, University of Warwick, Coventry, CV4 7AL, UK

(Submitted May 10, 2000; revised July 18, 2000)

Fiz. Nizk. Temp. **26**, 1202–1206 (December 2000)

Si/Si_{0.64}Ge_{0.36} heterojunctions with *p*-type conductivity exhibit an electron overheating effect. An analysis of the damping of the amplitudes of the Shubnikov–de Haas oscillations upon a change in temperature and applied electric field yields the temperature dependence of the electron–phonon relaxation time: $\tau_{\text{eph}} = 10^{-8} T^{-2}$ s. © 2000 American Institute of Physics. [S1063-777X(00)00512-0]

Two-dimensional electron systems (inversion layers, delta layers, heterojunctions, and quantum wells) have unique properties in that, on the one hand, the charge carriers in them have a two-dimensional character of their motion and, on the other hand, this two-dimensional state is realized in the bulk of the semiconductor, i.e., the phonons interacting with the carriers are three-dimensional. Information about the electron–phonon interaction in inversion layers, delta layers, and heterojunctions at low temperatures (~ 1 K) cannot be obtained from the behavior of the quantum corrections to the conductivity due to the weak localization and electron interaction effects (see, e.g., Refs. 1–7), since at such temperatures the dominant inelastic relaxation process is electron–electron scattering.

The electron–phonon interaction time τ_{eph} can be determined by studying the electron overheating effect.⁸ In the electron overheating effect the electron temperature T_e exceeds the phonon temperature T_{ph} under the influence of a high electric field (current) or of other, “heating” factors. The transfer of excess energy from the electron to the phonon system, even under conditions of strong elastic scattering, is governed by the time τ_{eph} . Therefore the problem of determining τ_{eph} experimentally reduces to finding the value of the overheating of the electron gas $\Delta T_e = (T_e - T_{\text{ph}})$ under conditions of high current flow. To realize the electron overheating effect it is necessary to ensure the free escape of phonons from the conducting layer into the surrounding crystal (i.e., to provide good acoustical coupling of the conducting layer and the crystal). This requirement is manifestly satisfied for inversion layers, delta layers, and heterostructures.

The electron overheating effect has been analyzed previously with the use of Shubnikov–de Haas (SdH) oscillations for inversion layers on silicon^{9,10} and for Si/Si_{0.7}Ge_{0.3} heterostructures with *n*-type conductivity.¹¹ In the cited papers the falloff of the amplitude of the oscillations with increasing applied electric field was used to find a relation between the electron temperature and the rate of loss of the excess energy by the electrons; in Ref. 11 the dependence of the energy

loss time on the overheating temperature was found, and it was concluded that the main channel of electron energy loss is the emission of acoustical phonons.

In this study we have realized the electron overheating effect in Si/Si_{0.64}Ge_{0.36} heterojunctions containing implanted boron, which led to a *p*-type conductivity. The samples were obtained by molecular beam epitaxy (MBE).¹ The conducting region had a width of 0.55 mm, and the distance between the potential contacts was 2.25 mm. The mobile charge carrier concentration n was $2 \times 10^{11} \text{ cm}^{-2}$, and the Hall mobility of the carriers was $\sim 12000 \text{ cm}^2 \text{ V}^{-1} \text{ s}^{-1}$.

At low temperatures (0.35–2 K) the heterojunctions exhibited pronounced SdH oscillations (Fig. 1). Naturally, as the temperature was raised, and also as the current flowing through the heterojunctions increased, the amplitude of the SdH oscillations fell off. The electron temperature T_e under conditions of high current flow can be determined from a comparison of the change in the amplitude of the SdH oscillations under the influence of current and under the influence of temperature. We carried out such an analysis for three extrema in the magnetic field interval 8–14 kOe. Figure 2 shows the change in the amplitude of the SdH oscillations with quantum numbers $\nu = 5, 6, 7$ as the temperature and current are varied. From a comparison of the curves one can find T_e at each specified value of the current.

The value of τ_{eph} can be calculated from the data for the electron overheating effect with the use of the heat balance equation, which assumes that the electrical power $P = E^2 \sigma$ released in a unit volume is equal to the amount of energy transferred by the electrons to the lattice per unit time:

$$E^2 \sigma = \int_{T_{\text{ph}}}^{T_e} \frac{C_e(T) dT}{\tau_{\text{eph}}(T)}. \quad (1)$$

If it is assumed that $\tau_{\text{eph}}^{-1} = \alpha T^p$ and that the electronic heat capacity $C_e(T) = \gamma T$, then it follows from (1) that¹²

$$E^2 \sigma = \frac{\alpha \gamma}{p+2} (T_e^{p+2} - T_{\text{ph}}^{p+2}). \quad (2)$$

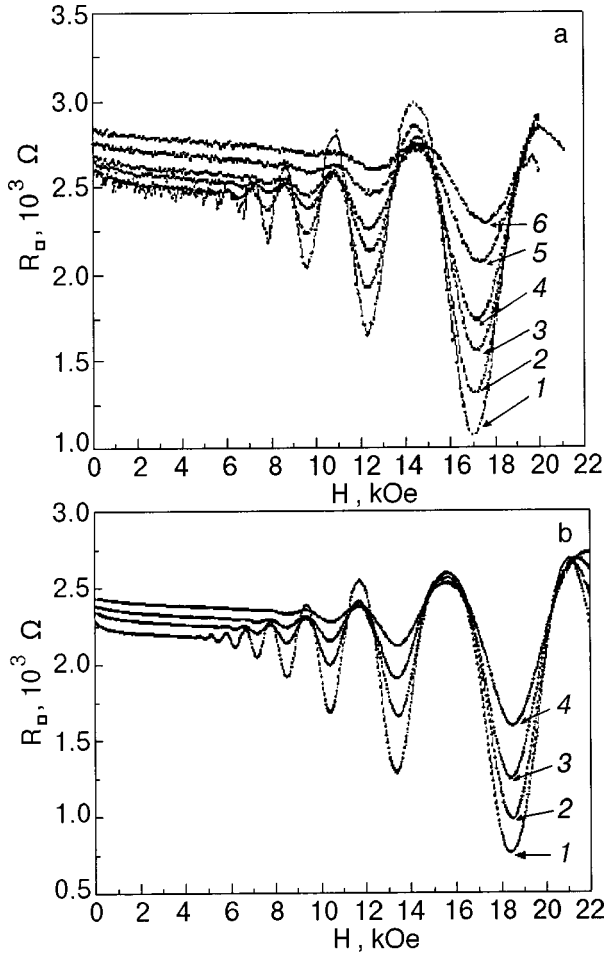


FIG. 1. Shubnikov-de Haas oscillations at various temperatures T [K]: 0.334 (1), 0.619 (2), 0.834 (3), 0.984 (4), 1.281 (5), and 1.514 (6) (a) and at various currents [nA]: 100 (1), 1000 (2), 1790 (3), and 3000 (4) (b).

Under the condition $T_e \gg T_{ph}$ one should observe a dependence $T_e \propto E^{2/(p+2)}$. Figure 3 shows the experimental dependence of T_e on the applied electric field E (points) together with the relation $T_e \propto E^{1/2}$ (continuous curve), which approximates the experimental data quite well (except for the points at small E , for which the condition $T_e \gg T_{ph}$ is not satisfied). Thus we arrive at the preliminary finding that the exponent p in the relation $\tau_{eph}^{-1} = \alpha T^p$ is equal to 2.

We attempted to find the temperature dependence $\tau_{eph}(T)$ directly from the experimental data presented above. Let us assume that in the steady state τ_{eph} in (1) corresponds to a certain temperature T_{eph} that characterizes the electron-phonon interaction under conditions of electron overheating. Then from (1) we have

$$E^2 \sigma = (T_e - T_{ph}) \frac{T_e + T_{ph}}{2} \frac{\gamma}{\tau_{eph}(T_{eph})}. \quad (3)$$

For $T_{eph} = (T_e + T_{ph})/2$ Eq. (3) implies the following relation, which was first given in Ref. 13:

$$T_e - T_{ph} = \frac{E^2 \sigma}{\gamma T_{eph}} \tau_{eph}(T_{eph}). \quad (4)$$

Since the value of γ is unknown for our objects of study, we must turn to the relation¹⁴

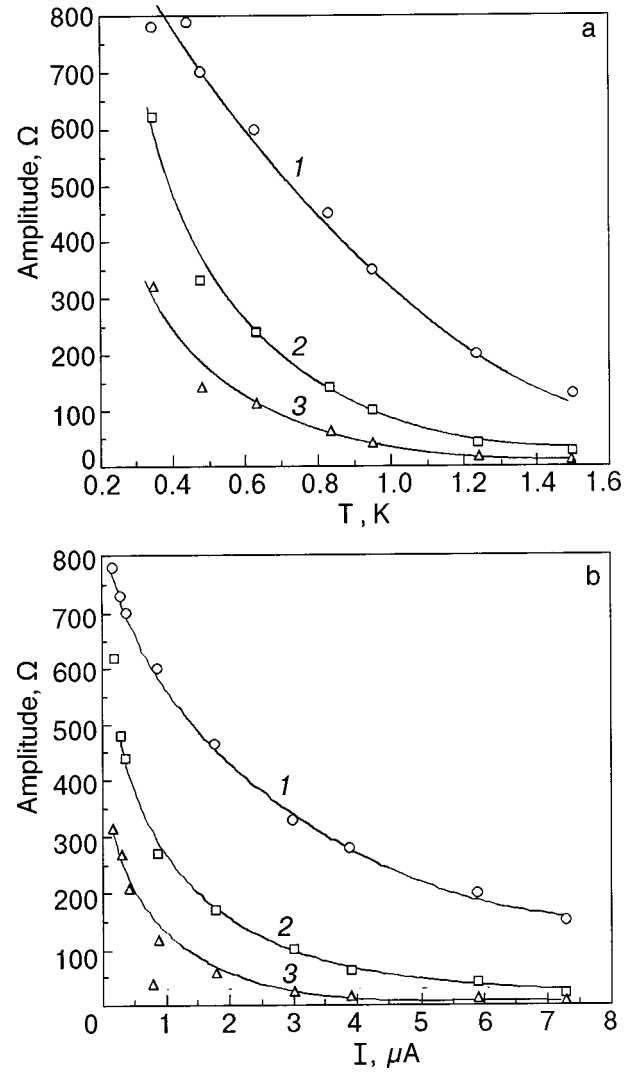


FIG. 2. Change in the amplitude of the SdH oscillations with quantum numbers $\nu = 5$ (1), 6 (2), 7 (3) upon changes in temperature (a) and current (b).

$$(kT_e)^2 = (kT_{ph})^2 + \frac{6}{\pi^2} (eE)^2 D \tau_{eph}, \quad (5)$$

where D is the electron diffusion coefficient, and E is the electric field that leads to heating of the electrons. This relation is obtained from Eq. (4) with the electronic heat capacity and conductivity expressed in terms of the density of states ν_{ds} : $C_e = (\pi^2/3) k^2 \nu_{ds} T$ and $\sigma = e^2 \nu_{ds} D$. For two-dimensional electrons $\nu_{ds} = m^*/(\pi \hbar^2)$, $D = (1/2) v_F^2 \tau$, and the Fermi velocity $v_F = (\hbar/m^*) (2\pi n)^{1/2}$. The elastic scattering time can be determined from the formula $R_{\square}^{-1} = n e^2 \tau / m^*$. For the effective mass we take the value $m^* = 0.242 m_0$ (m_0 is the free electron mass), obtained from an analysis of the SdH oscillations. The electric field in a conducting channel of length L and width a can be found from the values of the current I and the resistance per square R_{\square} : $E = IR/L = IR_{\square}/a$ (since $R = R_{\square} L/a$). For T_{ph} one should take the temperature of the crystal (in our case $T_{ph} = 0.37$ K).

From calculations based on Eq. (5) we obtained the temperature dependence of τ_{eph} (Fig. 4). We assumed, as in Refs. 15 and 16, that $T_{eph} = 1/2(T_{ph} + T_e)$. The temperature

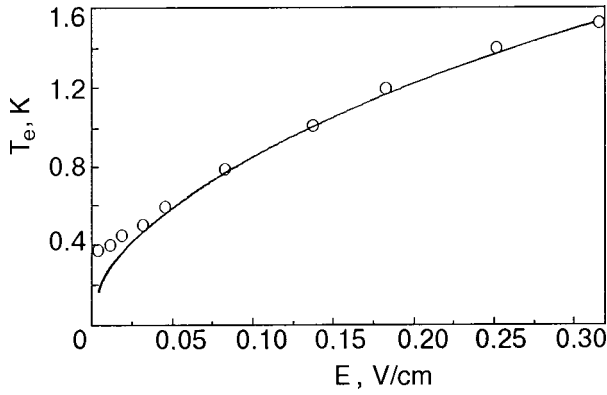


FIG. 3. Electron temperature T_e versus the applied electric field E (points) and the approximating function $T_e \propto E^{1/2}$ (continuous curve).

dependence $\tau_{\text{eph}}(T)$ presented in Fig. 4 can be approximated at temperatures above ~ 0.4 K by a power law: $\tau_{\text{eph}} = 10^{-8} T^{-p}$, where $p \approx 2$.

Let us discuss the possible causes of a temperature dependence $\tau_{\text{eph}}^{-1} \propto T^2$. For three-dimensional conductors in the “clean” limit one should have $\tau_{\text{eph}}^{-1} \propto T^3$ (Refs. 17 and 18), while for strong disordering, in the “dirty” limit, the theory predicts a weakening of the electron–phonon interaction and the appearance of a temperature dependence of the form $\tau_{\text{eph}}^{-1} \propto lT^4$, where l is the mean free path of the electrons^{17,19,20} (the transition from the “clean” to the “dirty” limit corresponds to a transition from the inequality $q_{\text{ph}}l > 1$ to the inequality $q_{\text{ph}}l < 1$, so that in the latter case the mean free path of the electrons is shorter than the wavelength of a thermal phonon, $\lambda_{\text{ph}} = 2\pi/q_{\text{ph}} = 2\pi\hbar s/kT$, where q_{ph} is the phonon wave vector and s is the phonon velocity).

Our experimental dependence $\tau_{\text{eph}}^{-1} \propto T^2$ is very often observed for thin films in an analysis of the behavior of the quantum corrections to the conductivity due to weak localization and electron interaction effects (see, e.g., Refs. 16 and 21–25) or in the analysis of experiments on electron overheating (see, e.g., Refs. 15 and 26–29). The appearance of a temperature dependence of this kind for films can be attributed to modification of the phonon spectrum in thin films. Let us clarify this statement. The time τ_{eph} is determined by the Éliashberg function $\alpha^2(\omega)F(\omega)$ in the frequency region corresponding to the energy of thermal phonons:³⁰

$$\tau_{\text{eph}}^{-1} = 4\pi \int d\omega \frac{\alpha^2(\omega)F(\omega)}{\text{sh}(\hbar\omega/kT)}. \quad (6)$$

For a quantized phonon spectrum the density of states is a linear function of ω , i.e., $F(\omega) \propto \omega$. In that case (with allowance for the weak dependence of α on ω) it turns out that $\tau_{\text{eph}}^{-1} \propto T^2$. An analogous result was observed in an analysis of the possibility that shear waves (waves of the Love type) with an unusual dispersion relation $\omega \propto q^{1/2}$ can exist in a film–substrate system.³¹ We might also point out Refs. 12 and 32, in which a dependence $\tau_{\text{eph}}^{-1} \propto lT^3$ was obtained in the “dirty” limit for the case of a two-dimensional phonon spectrum. Accordingly, in the “clean” limit one would expect a dependence of the form $\tau_{\text{eph}}^{-1} \propto T^2$. However, these variant explanations of the behavior $\tau_{\text{eph}}^{-1} \propto T^2$ cannot be directly ap-

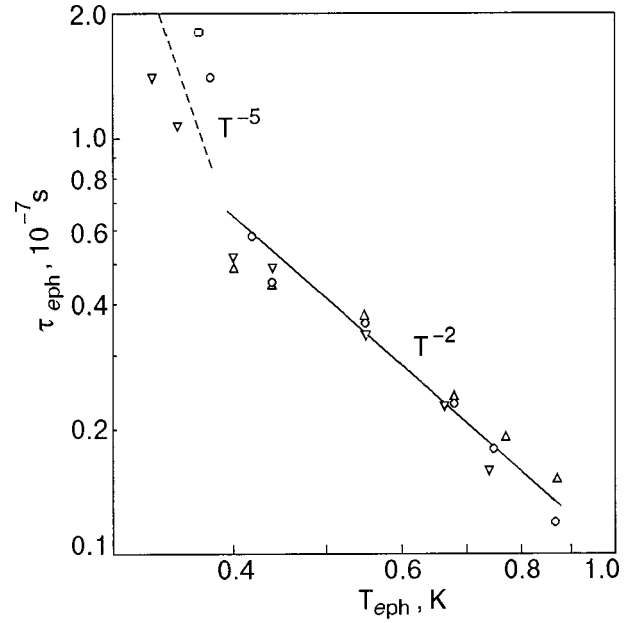


FIG. 4. Temperature dependence of the electron–phonon relaxation time τ_{eph} found from the decrease in amplitude of the SdH oscillations with quantum numbers $\nu=5$ (Δ), 6 (∇), and 7 (\circ) under the influence of a current.

plied to the heterostructures studied here, since in them the two-dimensionality is inherent to the electron system, while the phonons remain three-dimensional.

In our view, the temperature dependence $\tau_{\text{eph}}^{-1} \propto T^2$ obtained in this study is due to the two-dimensional nature of the electron system. In heterojunctions, as a result of the discontinuity of the bands at the heterointerface and the appearance of internal electric fields, a potential well (which to a first approximation is triangular in shape) is formed in which the motion of the electrons (or holes) in the direction transverse to the well (along the z axis) is quantized, while in the plane of the interface (xy) the motion remains free. The electrons occupy size-quantization levels (subbands) and are described by the dispersion relation

$$\varepsilon = \frac{p_x^2 + p_y^2}{2m} + \varepsilon_i. \quad (7)$$

At low temperatures the absorption or emission of phonons is accompanied by a change in the electron momentum components p_x, p_y . At high temperatures, intersubband transitions can occur. According to Ref. 33, for $kT > kT_2 = \sqrt{8ms^2W}$ (where $W = \pi^2\hbar^2/(2md^2)$ is, in order of magnitude, the ground-state energy of the size quantization, s is the speed of sound, and d is the characteristic width of the well) the electron–phonon scattering processes are quasielastic and are characterized by a temperature dependence $\tau_{\text{eph}}^{-1} \propto T$. An estimate of T_2 for our objects (for $s = 9 \times 10^5$ cm/s,³⁴ $d \sim 100$ Å) gives a value ~ 40 K. At low temperatures ($T < T_2$) a situation can arise in which the wave momentum of a thermal phonon, $q_T = kT/(\hbar s)$, is sufficient to change the electron wave vector by the maximum value $2k_F$, since at lower temperatures one has $q_T < 2k_F$, and only small-angle scattering of the electrons is possible. The temperature T_1 separating these regions corresponds to the condition $q_T = 2k_F$. In the region of partial inelasticity ($T > T_1$) an elec-

tron upon interacting completely changes its momentum and absorbs (emits) a phonon with a wave vector predominantly perpendicular to the interface. Conservation of total momentum and energy for the two-dimensional electron system implies a dependence $\tau_{\text{eph}}^{-1} \propto T^2$ (Ref. 33). In the small-angle scattering region ($T < T_1$) the wave vector of the phonon participating in the interaction is arbitrary in direction and limited in magnitude by the temperature. In this case the scattering is similar to small-angle scattering in a three-dimensional metal and is described by a temperature dependence $\tau_{\text{eph}}^{-1} \propto T^5$ (Refs. 33 and 35).

The temperature dependence $\tau_{\text{eph}}^{-1} \propto T^2$ found in the present study corresponds to the region of partial inelasticity $T > T_1$. In Fig. 4 one can discern a tendency for $\tau_{\text{eph}}(T)$ to become steeper for $T < 0.4$ K. For purposes of illustration, the dashed line in Fig. 4 shows the dependence $\tau_{\text{eph}}^{-1} \propto T^5$. Thus the experimental results are described rather successfully in terms of the concept developed for electron–phonon relaxation of two-dimensional charge carriers.³³ At the same time, numerical estimates of the characteristic temperature T_1 for the transition from a dependence of the form $\tau_{\text{eph}}^{-1} \propto T^2$ to $\tau_{\text{eph}}^{-1} \propto T^5$ did not give a unique value. For example, the value $k_F = 0.04 \times 10^6 \text{ cm}^{-1}$ found from the condition $q_T = 2k_F$ for $T_1 \sim 0.4$ K turned out to be substantially smaller than the value of the wave vector determined from the well-known relation for a two-dimensional electron system: $k_F = (2\pi n)^{1/2}$. In the latter case the value $k_F = 1.12 \times 10^6 \text{ cm}^{-1}$ was obtained. This discrepancy is possibly due to the fact that the total concentration of charge carriers is distributed between the size-quantization subbands, and at low temperatures the subband with the low occupation becomes important in electron–phonon relaxation processes. Our values of τ_{eph} (10^{-7} – 10^{-8} s at T_{eph} in the interval 0.37–1 K) are entirely reasonable.

The authors thank C. P. Parry, P. J. Phillips, and T. J. Grasby for the MBE preparation of the samples, and M. Mironov for taking part in the measurements.

*E-mail: komnik@ilt.kharkov.ua

¹⁾The samples were prepared at the Advanced Semiconductors Group, University of Warwick, Coventry, UK.

¹Y. Kavaguchi and S. Kawaji, *J. Phys. Soc. Jpn.* **48**, 699 (1980).

²M. J. Uren, R. A. Davies, M. Kaveh, and M. Pepper, *J. Phys. C* **14**, 5737 (1981).

³D. J. Bichop, R. C. Dynes, and D. C. Tsui, *Phys. Rev. B* **26**, 773 (1982).

⁴M. Asche, K. J. Friedland, P. Kleinert, and H. Kostial, *Semicond. Sci. Technol.* **7**, 923 (1992).

⁵N. L. Matthey, T. E. Whall, R. A. Kubiak, and M. J. Kearney, *Semicond. Sci. Technol.* **7**, 604 (1992).

⁶Vit. B. Krasovitskiĭ, O. N. Makarovskii, O. A. Mironov, T. Whall, and N. L. Matthey, *Fiz. Nizk. Temp.* **21**, 833 (1995) [*Low Temp. Phys.* **21**, 612 (1995)].

⁷V. Yu. Kashirin, Yu. F. Komnik, O. A. Mironov, C. J. Emelius, and T. E. Whall, *Fiz. Nizk. Temp.* **22**, 1174 (1996) [*Low Temp. Phys.* **22**, 642 (1996)].

⁸V. A. Shklovskii, *J. Low Temp. Phys.* **41**, 375 (1980).

⁹T. Neugebauer and G. Landwehr, *Phys. Rev. B* **21**, 702 (1980).

¹⁰J. Lutz, F. Kuchar, K. Ismail, H. Nickel, and W. Schlapp, *Semicond. Sci. Technol.* **8**, 399 (1993).

¹¹G. Stöger, G. Brunthaler, G. Bauer, K. Ismail, B. S. Meyerson, J. Lutz, and F. Kuchar, *Semicond. Sci. Technol.* **9**, 765 (1994).

¹²P. M. Echternach, M. R. Thoman, C. M. Gould, and H. M. Bozler, *Phys. Rev. B* **46**, 10339 (1992).

¹³P. W. Anderson, E. Abrahams, and T. V. Ramakrishnan, *Phys. Rev. Lett.* **43**, 718 (1979).

¹⁴S. Hershfield and V. Ambegaokar, *Phys. Rev. B* **34**, 2147 (1986).

¹⁵S. I. Dorozhkin, F. Lell, and W. Schoepe, *Solid State Commun.* **60**, 245 (1986).

¹⁶V. Yu. Kashirin and Yu. F. Komnik, *Fiz. Nizk. Temp.* **19**, 410 (1993) [*Low Temp. Phys.* **19**, 288 (1993)].

¹⁷J. Rammer and A. Schmid, *Phys. Rev. B* **34**, 1352 (1986).

¹⁸M. Yu. Reizer, *Phys. Rev. B* **40**, 5411 (1989).

¹⁹A. Schmid, *Z. Phys.* **259**, 421 (1973).

²⁰M. Yu. Reizer and A. V. Sergeev, *Zh. Éksp. Teor. Fiz.* **90**, 1056 (1986) [*Sov. Phys. JETP* **63**, 616 (1986)].

²¹M. E. Gershenson, V. N. Gubankov, and Yu. E. Zhuravlev, *Zh. Éksp. Teor. Fiz.* **85**, 287 (1983) [*Sov. Phys. JETP* **58**, 167 (1983)].

²²R. P. Peters and G. Bergman, *J. Phys. Soc. Jpn.* **54**, 3478 (1985).

²³R. Rosenbaum, M. Ben-Shlomo, S. Goldsmith, and R. L. Boxmax, *Phys. Rev. B* **39**, 10009 (1989).

²⁴G. Dumpich and A. Carl, *Phys. Rev. B* **43**, 12074 (1991).

²⁵B. I. Belevtsev, Yu. F. Komnik, and E. Yu. Belyaev, *Fiz. Nizk. Temp.* **21**, 839 (1995) [*Low Temp. Phys.* **21**, 646 (1995)].

²⁶S. I. Dorozhkin and V. T. Dolgoplov, *JETP Lett.* **36**, 18 (1982).

²⁷C. G. Smith, and M. N. Wybourne, *Solid State Commun.* **57**, 411 (1986).

²⁸G. Bergman, Wei Wei, Yao Zou, and R. M. Mueller, *Phys. Rev. B* **41**, 7386 (1990).

²⁹E. M. Gershenson, M. E. Gershenson, G. N. Gol'tsman, A. M. Lyul'kin, A. D. Semenov, and A. V. Sergeev, *Zh. Éksp. Teor. Fiz.* **97**, 901 (1990) [*Sov. Phys. JETP* **70**, 505 (1990)].

³⁰B. Keck and A. Schmid, *J. Low Temp. Phys.* **24**, 611 (1976).

³¹E. S. Syrkin, Yu. F. Komnik, and E. Yu. Belyaev, *Fiz. Nizk. Temp.* **22**, 107 (1996) [*Low Temp. Phys.* **22**, 80 (1996)].

³²D. Belitz and S. Das Sarma, *Phys. Rev. B* **36**, 7701 (1987).

³³V. Karpus, *Fiz. Tekh. Poluprovodn.* **20**, 12 (1986) [*Sov. Phys. Semicond.* **20**, 6 (1986)]; *Fiz. Tekh. Poluprovodn.* **21**, 1949 (1987) [*Sov. Phys. Semicond.* **21**, 1180 (1987)]; *Fiz. Tekh. Poluprovodn.* **22**, 439 (1988) [*Sov. Phys. Semicond.* **22**, 268 (1988)].

³⁴M. P. Shaskol'skaya (Ed.), *Acoustic Crystals* [in Russian], Nauka, Moscow (1982).

³⁵P. J. Price, *Solid State Commun.* **51**, 607 (1984).

Translated by Steve Torstveit

QUANTUM EFFECTS IN SEMICONDUCTORS AND DIELECTRICS**Selective spectroscopy of Pr³⁺ impurity ions in Y₂SiO₅, Gd₂SiO₅, and Lu₂SiO₅ crystals**

Yu. V. Malyukin,* R. S. Borisov, P. N. Zhmurin, A. N. Lebedenko, and B. V. Grinev

Institute of Single Crystals, National Academy of Sciences of Ukraine, pr. Lenina 60, 61001 Kharkov, Ukraine

N. V. Znamensky, É. A. Manykin, Yu. V. Orlov, E. A. Petrenko, and T. G. Yukina

Kurchatov Institute Russian Science Center, pl. Kurchatova 1, 123182 Moscow, Russia

(Submitted May 12, 2000; revised June 26, 2000)

Fiz. Nizk. Temp. **26**, 1207–1213 (December 2000)

Based on a study of the low-temperature optical spectra of Pr³⁺ activator ions in Y₂SiO₅, Gd₂SiO₅, and Lu₂SiO₅ crystals, it is shown that the parameters and character of the crystal-field splitting of the ¹D₂ and ³H₄ terms of the impurity ions are substantially different in crystals belonging to different crystallographic types. In Y₂SiO₅ and Lu₂SiO₅ crystals a pseudosymmetry effect is observed in the splitting of the ¹D₂ term for ions localized in inequivalent cation sites. The activator ions nonuniformly occupy the inequivalent cation sites as their concentration is increased. At high concentrations of activator ions (~1 at. %) the optical absorption spectra exhibit spectral lines belonging to dimers of activator ions.

© 2000 American Institute of Physics. [S1063-777X(00)00612-5]

1. INTRODUCTION

Y₂SiO₅ (YSO), Gd₂SiO₅ (GSO), and Lu₂SiO₅ (LSO) are crystals of the oxyorthosilicate class.^{1,2} A rather large number of rare-earth impurity ions (up to 10 at. %) can be introduced into the cation sites of YSO, LSO, and GSO without degrading the structural and optical quality.³ This property of oxyorthosilicates gives them an advantage over other crystalline matrices.⁴ For example, problems with optical quality are well known for the laser crystal Al₂O₃:Ti³⁺ starting at only 0.1 at. % activator ions.^{4,5} The high isomorphous capacity of YSO, LSO, and GSO crystals is extremely attractive for developing new laser and scintillator materials. In this regard the activator ions Ce³⁺ and Pr³⁺ are of particular interest.^{4,6–9} Oxyorthosilicates activated by Ce³⁺ ions are efficient scintillators which have been recently developed.^{6,7,10} The Pr³⁺ ion provides multifrequency laser generation under IR pumping.^{8,9}

The YSO, LSO, and GSO crystals are of different structural types.^{1,2} This is reflected, in particular, in differences in their unit cell parameters: YSO ($a = 14.43 \text{ \AA}$, $b = 10.41 \text{ \AA}$, $c = 6.733 \text{ \AA}$, $\beta = 122.13^\circ$, $V = 856.1 \text{ \AA}^3$), LSO ($a = 14.33 \text{ \AA}$, $b = 10.32 \text{ \AA}$, $c = 6.671 \text{ \AA}$, $\beta = 122.3^\circ$, $V = 833.8 \text{ \AA}^3$), GSO ($a = 9.16 \text{ \AA}$, $b = 7.09 \text{ \AA}$, $c = 6.83 \text{ \AA}$, $\beta = 107.58^\circ$, $V = 422.9 \text{ \AA}^3$). It is also known that the unit cell of these crystals has two inequivalent cation sites.^{1,2}

For example, in the YSO crystal one of the sites is a distorted octahedron in which the Y–O distance varies in the range 2.21–2.33 Å.^{1,2} The second site has a coordination sphere with an additional, seventh oxygen ion drawn into it.^{1,2} For the second type of cation site the Y–O distance varies in the range 2.15–2.39 Å.^{1,2} thus the inequivalence of the cation sites is due to different coordination numbers with respect to oxygen and different distances from the rare-earth ion to the ligand.^{1,2}

In connection with the aforementioned features of the lattice structure of oxyorthosilicates, it is of considerable importance to elucidate the relations governing the splitting of the terms of the Pr³⁺ impurity ion under the influence of the crystalline field in crystals having different structural types and also to determine the essentials of how the optical spectra transform as the concentration of activator ions is increased.

In this paper we show that two Pr³⁺ optical centers form in YSO, LSO, and GSO crystals, corresponding to the substitution of the activator ions into the two inequivalent cation sites. In YSO and LSO crystals a pseudosymmetry effect is observed in the splitting of the ¹D₂ term into Stark levels for the Pr³⁺ ions localized in different cation sites. It is found that as the activator concentration increases, a nonuniform occupation of the inequivalent cation sites of the YSO lattice occurs.

2. EXPERIMENTAL TECHNIQUE

The optical absorption and luminescence spectra of the crystals were recorded on an automated spectrofluorimeter constructed on the basis of an MDR-23 grating monochromator. The luminescence spectra were excited by a frequency-tunable organic dye laser. The luminescence quenching kinetics in the samples was recorded by a technique of time-correlated counting of single photons.

The YSO, LSO, and GSO crystals were grown by the Czochralski method. In the LSO and GSO samples the activator ion concentration was 0.3 at. %. In the YSO crystal the activator ion concentration was varied (0.3, 0.6, and 1.8 at. %).

Low temperatures were attained by means of a helium optical cryostat. The crystals were immersed in helium vapor.

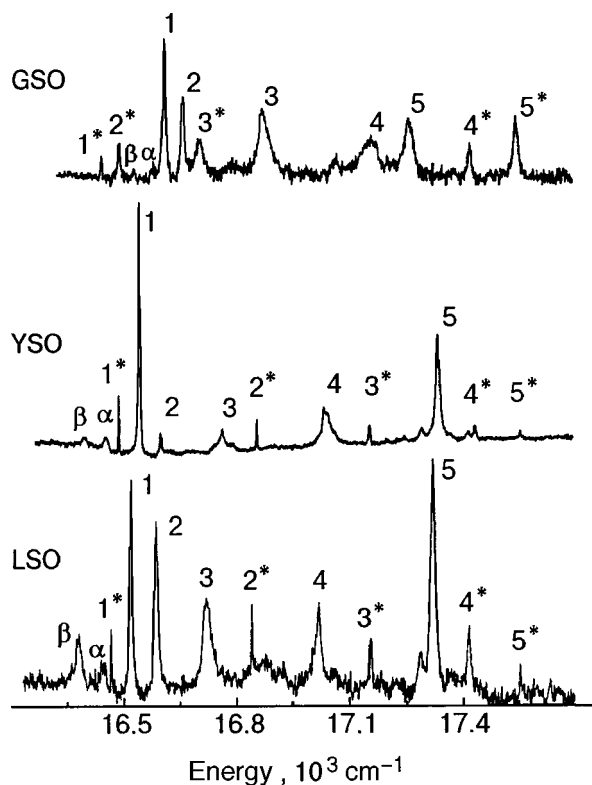


FIG. 1. Fragments of the absorption spectra of LSO, YSO, and GSO crystals in the region of the optical transitions ${}^3H_4 \leftrightarrow {}^1D_2$ of Pr^{3+} impurity ions at $T = 77$ K.

3. EXPERIMENTAL RESULTS AND DISCUSSION

We investigated a spectral region containing optical transitions involving the Stark components of the 1D_2 and 3H_4 terms of the Pr^{3+} ion.^{11–13} This choice was made because of the relative simplicity of interpretation of the spectral lines. For example, the spectral lines due to optical transitions between the Stark components of the terms 1I_6 , 1P_3 , and 3H_4 are strongly mixed, making their correction interpretation difficult.^{11,12}

Figure 1 shows fragments of the absorption spectra of YSO, LSO, and GSO crystals containing Pr^{3+} ions. The spectral region corresponds to the interval in which the optical spectra of Pr^{3+} impurity ions are observed.^{11–14} For YSO and LSO crystals one can distinguish two groups of spectral lines with considerably different widths. The spectral lines of one of these groups are labeled by just a number, and the other by a number with an asterisk. Each group consists of five spectral lines. The spectral lines broaden monotonically as their number in the sequence increases. Such behavior is ordinarily observed in rare-earth ions for spectral lines belonging to the same multiplet.¹⁴

The indicated groups of spectral lines belong to two Pr^{3+} optical centers. The different optical centers are formed as a result of the substitution of Pr^{3+} ions in two inequivalent cation sites.^{1,2} Each of the five spectral lines is due to an optical transition between the lower Stark component of the 3H_4 term and the five Stark components of the 1D_2 term. In YSO, LSO, and GSO crystals the degeneracy of the 1D_2 and 2H_4 terms of the Pr^{3+} ion is completely lifted by the crystalline field, since the point symmetry of the two cation sites is extremely low.^{1,2}

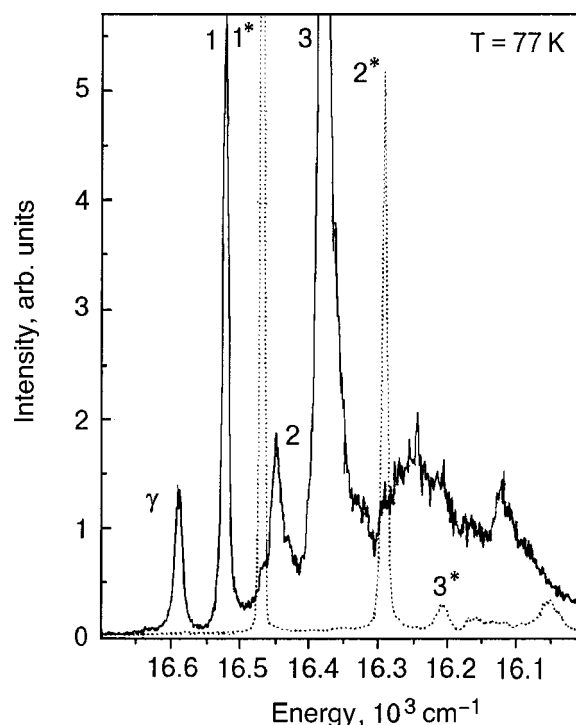


FIG. 2. Fragments of the luminescence spectra upon the selective excitation of the two types of Pr^{3+} optical centers in the LSO crystal.

The dividing of the spectral lines into groups and the identification of each spectral line were based on a study of the luminescence spectra under selective excitation and of the temperature dependence of certain lines in the absorption spectrum (Fig. 1). For example, the spectral lines α and β vanished when the crystals were cooled to 5 K. Selective excitation of each of the spectral lines belonging to a single group gave rise to identical luminescence spectra (Fig. 2). Excitation into spectral lines belonging to different groups (Fig. 1) gave rise to two types of luminescence spectra (Fig. 2). The highest-frequency spectral line in the luminescence spectra of both types were resonantly coincident with spectral line 1 or 1^* (Fig. 1). The frequency intervals separating spectral lines α and β from line 1 (Fig. 1) was precisely coincident with the frequency intervals between the two spectral lines lying below line 1 in energy in the luminescence spectrum (Fig. 2). Consequently, the spectral lines α and β are due to absorption from the two lower, thermally populated Stark components of the term 3H_4 .

It has previously been proposed¹³ that the spectral line due to the second Stark component of the 1D_2 term is hidden inside spectral line 1 (Fig. 1). Selective spectroscopy of the optical spectra in the YSO crystal has made it possible to give a complete interpretation of the line in the absorption spectrum of the second type (Fig. 1).

In the luminescence spectra of the YSO, LSO, and GSO crystals also contain spectral lines with temperature-dependent intensities. For example, for LSO at 77 K the luminescence spectrum of the first type contains a spectral line γ (Fig. 2) that vanishes at a temperature of 5 K. This line is due to the luminescence from the second, thermally populated Stark component of the 1D_2 term. The frequency intervals separating the spectral lines 1 and γ in the luminescence

TABLE I. Parameters of the splitting of the 1D_2 term in reference to the spectral lines 1 and 1* (their frequencies are indicated in parentheses).

Splitting parameter, cm^{-1}					
YSO		LSO		GSO	
type I	type II	type I	type II	type I	type II
0(16529.2)	0(16477.3)	0(16521.7)	0(16466.9)	0(16657.9)	0(16496.7)
59.6	364	66	373.7	42.1	43.8
224.9	667.9	202.2	688.4	248	248.7
501.2	948	498.2	951.7	525.9	940
801.3	1071.5	801.8	1091.4	621.8	1056.7

spectrum (Fig. 2) and the spectral lines 1 and 2 in the absorption spectrum (Fig. 1) are the same.

The features of the luminescence spectra noted above, together with the clear connection between the temperature dependence of the spectral lines in the absorption spectrum (Fig. 1) and in the luminescence spectrum (Fig. 2), make it possible to find the values of the splitting of the 1D_2 and 3H_4 terms of the Pr^{3+} impurity ions under the influence of the crystalline field in YSO, LSO, and GSO crystals. The results of the analysis are summarized in Table I, which gives the values of the splitting of the 1D_2 term for the two optical centers, relative to the spectral lines 1 and 1* (Fig. 1). The character of the splitting of the 1D_2 term is substantially different for ions occupying the inequivalent cation sites. In the YSO and LSO crystals, which belong to the same crystallographic type,^{1,2} the energy parameters of the splitting of the 1D_2 term and of the Stark components are similar (see Fig. 1 and Table I). It is clear that the Stark components of the term are uniquely related to the corresponding spectral lines. For the first type of optical centers the spectral lines 1 and 2 are separated by a minimum energy interval $\sim 60 \text{ cm}^{-1}$. Spectral line 3 is adjacent to them. Then, after a substantially larger interval $\sim 290 \text{ cm}^{-1}$, come spectral lines 4 and 5 (Fig. 1). For the second type of optical centers in YSO and LSO crystals, lines 4* and 5* are separated by the smallest energy interval. Lower in energy is the spectral line 3*. Then, after an interval of $\sim 300 \text{ cm}^{-1}$, come the spectral lines 1* and 2*. In a qualitative sense, without maintaining the same frequency intervals, a quasi-reverse order is observed for the splitting of the 1D_2 term in the YSO and LSO crystals. This effect is similar to the splitting of the 2D term of the impurity ion Tl^{3+} in ligand fields with tetrahedral and octahedral symmetry.^{15,16} In the case considered in the present study one can speak of a quasisymmetry effect, since the inequivalent cation sites have extremely low point symmetry.

Unlike the YSO and LSO crystals, in GSO the spectral lines for the two optical centers are grouped by type: 1-2-3 (1*-2*-3*) and then 4-5 (4*-5*) (Fig. 1).

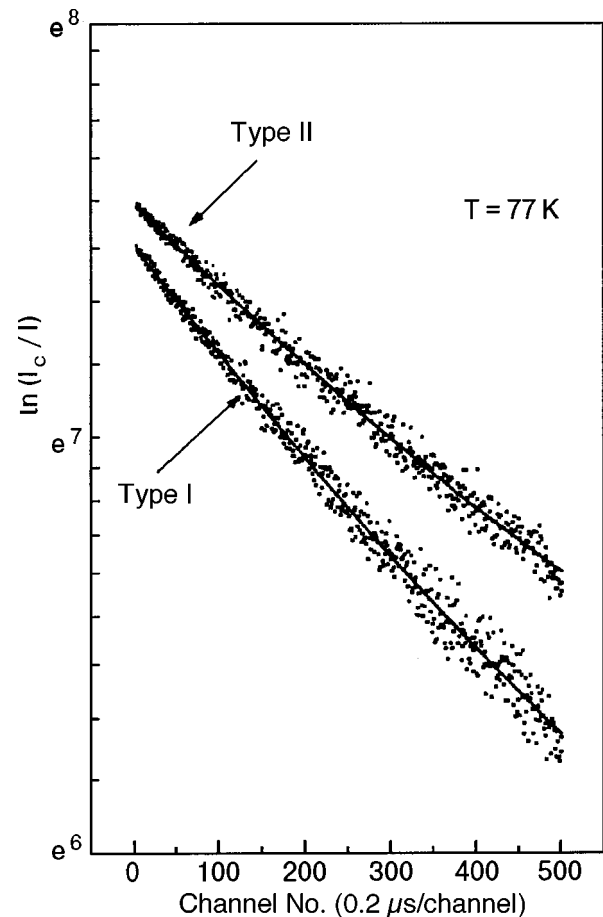
In Ref. 13 a complete interpretation is given for all nine lines in the luminescence spectrum of the YSO crystal, corresponding to optical transitions between the lower Stark component of the 1D_2 term and the nine Stark components of 3H_4 . For the LSO (Fig. 2) and GSO crystals there is as yet reliable information only for three of the spectral lines, which correspond to the analogous optical transitions to the three lowest Stark components of the 3H_4 term. For the GSO

TABLE II. Parameters of the splitting of the 3H_4 term in reference to the spectral lines 1 and 1* (their frequencies are indicated in parentheses).

Splitting parameter, cm^{-1}				
YSO		LSO		GSO
type I	type II	type I	type II	type I
0(16521)	0(16469.3)	0(16521)	0(16469.3)	0(16652.8)
89.7	174.7	72.5	178.5	27.7
143.6	274.8	135.8	261.3	82.8

crystal an interpretation of the spectral lines is given only for the luminescence spectrum of the first type. For comparison the parameters of the crystal-field splitting of the 3H_4 term relative to the spectral lines 1 and 1* are given in Table II.

The kinetics of the quenching of the emission in the luminescence spectra of both types was investigated under selective excitation of optical transitions belonging to different optical centers (Fig. 1). The kinetics of the luminescence quenching was identical for the spectral lines corresponding to the same type of luminescence. The shape of the luminescence quenching curves for the first and second types in YSO, LSO, and GSO crystals containing 0.3 at. % praseodymium ions is well described by a single-exponent power law (Fig. 3). The time constants for the quenching of the luminescence of the first and second types at $T=77 \text{ K}$ are as follows: $\tau_1=108 \text{ } \mu\text{s}$, $\tau_2=145 \text{ } \mu\text{s}$ for YSO; $\tau_1=64 \text{ } \mu\text{s}$, τ_2

FIG. 3. Kinetics of the luminescence quenching in the two types of luminescence spectra in an LSO crystal containing 0.3 at. % Pr^{3+} ions.

$=82 \mu\text{s}$ for LSO, and $\tau_1=39 \mu\text{s}$, $\tau_2=50 \mu\text{s}$ for GSO. The ratio of the time constants for the quenching of the luminescence of the first and second types was 1.3 for each crystal. A comparison of the splitting parameters of the terms 1D_2 (Table I) and 3H_4 (Table II) shows that the second type of Pr^{3+} optical centers is subjected to a stronger perturbation by the crystalline field. It is as if the time constant for quenching of the luminescence of the second type in this case should be smaller, since it is known^{4,14} that for electric-dipole optical transitions within the f shell of rare-earth ions the parity-forbiddenness is lifted by the crystalline field. In our case, however, an important role is played not only by the amplitude but also by the symmetry of the crystalline field in the region of localization of the impurity center. Apparently, for the second type of optical centers the contribution of the odd harmonics in the expansion of the field of the ligands is smaller than for the first. It is the odd harmonics of the crystalline field that lift the forbiddenness of the electric-dipole optical transitions within the f shell.^{4,14}

As expected, increasing the concentration of Pr^{3+} activator ions in the YSO crystal lead to a broadening of their optical spectra. The integrated area under the two spectral lines 1 and 1* increases in proportion to the increase in the total concentration of impurity ions. However, the integrated area of each of the lines 1 and 1* changes in different ways: the integrated area of the spectral line 1 grows in proportion to 1:2.2:6.5 while for line 1* this ratio is 1:1.6:3.2. Consequently, the impurity ions occupy the inequivalent sites of the YSO crystal in a nonuniform way. As the concentration of activator ions increases, additional spectral lines with a concentration-dependent intensity appear in their optical absorption spectra. In the case of the highest concentration of activator ions, the spectral lines δ_1 and δ_2 appear in the optical spectrum near the spectral lines 1 and 1* (Fig. 4). Essentially, the spectral line δ_2 merges with the spectral line 1 at high temperature. It is clear that the spectral lines δ_1 and δ_2 are of an identical nature. On account of the appreciable broadening of the spectral line 1, the line δ_2 is less pronounced (Fig. 4). Let us therefore analyze the causes of the appearance of the spectral line δ_1 . The frequency interval separating the high-frequency spectral satellite from line 1* is 8.9 cm^{-1} . We did not observe any line in the luminescence spectrum that would be resonantly coincident with δ_1 (Fig. 4).

The concentration dependence and temperature dependence of the intensity δ_1 suggest that the spectral line δ_1 is due to absorption by dimers of activator ions. Indeed, the activator ion concentration of 1.8 at. % is quite high, and activator ions can occupy two adjacent equivalent cation sites.¹⁷ As a result of the dipole-dipole interaction (V_{dd}) between identical activator ions, two dimeric energy states form.¹⁸ Depending on the relative orientation of the dipole moments of the optical transitions of the interacting ions, the optical spectrum of the dimer can manifest both states simultaneously or only one of them.¹⁸ In our case a dimeric energy state appears above the state of the isolated ion. Consequently, the dipole moments of the optical transitions of the interacting ions are directed precisely antiparallel.¹⁸ As a rule, the upper state of the dipole is subject to strong nonradiative relaxation.¹⁸ Therefore, the luminescence spectrum

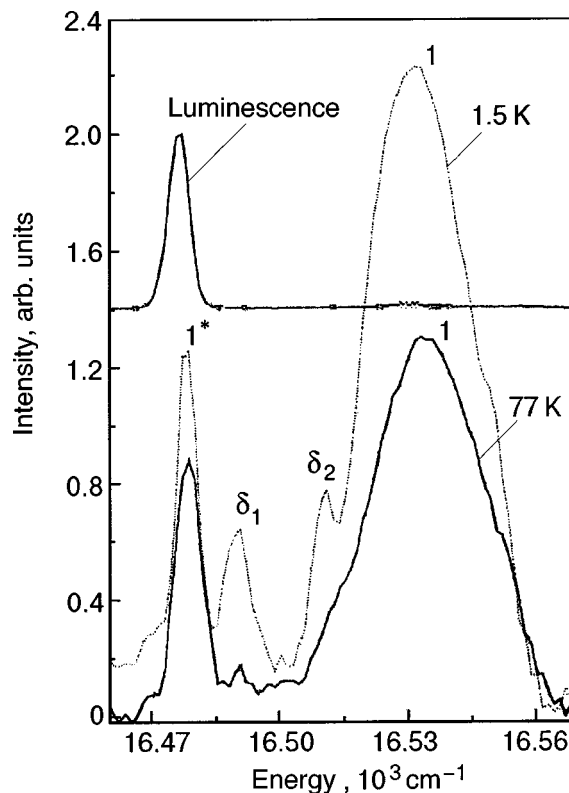


FIG. 4. Fragments of the absorption spectrum of a YSO crystal containing the highest concentration of activator ions (1.8 at. %) at different temperatures.

does not contain a spectral line resonantly coincident with δ_1 (Fig. 4).

In the general case the dimeric states are described by a wave function of the form $\phi = a_1(t)\varphi_1 + a_2(t)\varphi_2$ (where φ_1 and φ_2 are the wave functions of the states of the monomers; $a_1(t)$ and $a_2(t)$ are complex functions of time). If the relative phases $a_1(t)$ and $a_2(t)$ beat randomly with a frequency greater than V_{dd}/η , then the dimeric states are destroyed. Since the scattering of phonons on impurity centers is one of the causes of disruption of the phases of $a_1(t)$ and $a_2(t)$, increasing the temperature of the crystal leads to a decrease in the intensity of the spectral line δ_1 (Fig. 4). For a similar reason the dimeric states do not form if the initial states are subjected to strong nonradiative relaxation. This applies to the Stark components of the 1D_2 term, which lie above the metastable state in energy. Therefore, dimeric states do not form for the Stark components associated with the spectral lines 2*, 3*, 4*, and 5* (Fig. 1).

In Ref. 13, in the selective excitation of luminescence of the first type in the region of the optical transition $^3H_4 \leftrightarrow ^3P_0$ the spectral line 1* (Fig. 1), which belongs to the luminescence of the second type, was observed. Direct laser excitation of the optical centers of the second type was ruled out. Consequently, electronic excitation was transferred from the first type of optical center to the second. The mechanism responsible for the transfer of electronic excitation energy remains unclear. We therefore made a detailed investigation of the luminescence spectra in YSO crystals with different concentrations of activator ions. At $T=5$ and 77 K the luminescence spectra of the first and second types did not contain spectral lines that could belong to the other type of lumines-

cence. The fragment of the type-II luminescence spectrum in Fig. 4 shows that it completely lacks a spectral line resonantly coincident with line 1. Consequently, in the excitation of the spectra of the first and second types of luminescence in the region of the optical transitions involving the Stark components of the 1D_2 term there is no interaction between different optical centers.

4. CONCLUSION

Based on a study of the optical absorption spectra and the luminescence spectra under selective excitation we have shown that there are substantial differences in the parameters and the character of the crystal-field splitting of the 1D_2 and 3H_4 terms in crystals belonging to different crystallographic types (Table I). In YSO and LSO crystals a pseudosymmetry effect is observed in the splitting of the 1D_2 term for Pr^{3+} ions localized in inequivalent cation sites. The different Pr^{3+} optical centers in the YSO crystal do not interact when it is selectively excited in the region of the optical transitions ${}^1D_2 \leftrightarrow {}^3H_4$. In the YSO crystal the Pr^{3+} activator ions non-uniformly occupy the inequivalent cation sites. As the activator ion concentration is increased, their optical spectra broaden considerably, and spectral lines corresponding to dimeric states appear.

*E-mail: malyukin@isc.kharkov.com

¹B. A. Maksimov, Yu. A. Kharitonov, V. V. Ilyukhin, and N. V. Belov, *Kristallografiya* **15**, 926 (1970) [*Sov. Phys. Crystallogr.* **15**, 806 (1970)].

²B. A. Maksimov, Yu. A. Kharitonov, V. V. Ilyukhin, and N. V. Belov,

Dokl. Akad. Nauk SSSR **183**, 1072 (1968) [*Sov. Phys. Dokl.* **12**, 116 (1968)].

³G. V. Anan'eva, A. M. Korovkin, T. I. Merkulyaeva, A. M. Morozov, M. V. Petrov, I. R. Savinova, V. R. Startsev, and P. P. Feofilov, *Neorg. Mater.* **17**, 1037 (1981).

⁴A. A. Kaminskiĭ (Ed.), *Physics and Spectroscopy of Crystals* [in Russian], Nauka, Moscow (1986).

⁵R. E. Powell, *J. Appl. Phys.* **58**, 2331 (1985).

⁶C. L. Melcher, R. A. Manente, C. A. Peterson, and J. S. Schweitzer, *J. Cryst. Growth* **128**, 1001 (1993).

⁷P. Dorenbos, C. W. E. van Eijk, A. J. J. Bos, and C. L. Melcher, *J. Lumin.* **60–61**, 979 (1994).

⁸A. A. Kaminskiĭ, *Dokl. Akad. Nauk SSSR* **319**, 870 (1991) [*Sov. Phys. Dokl.* **36**, 586 (1991)].

⁹M. Malinowski, M. F. Joubert, and B. Jacquier, *J. Lumin.* **60–61**, 179 (1994).

¹⁰H. Suzuki, T. A. Tombrello, C. L. Melcher, and J. S. Schweitzer, *Nucl. Instrum. Methods Phys. Res. A* **320**, 263 (1992).

¹¹H. H. Caspers, H. E. Rast, and R. A. Buchanan, *J. Chem. Phys.* **43**, 2124 (1965).

¹²K. Holliday, M. Croci, E. Vauthey, and U. P. Wild, *Phys. Rev.* **47**, 14741 (1993).

¹³Yu. V. Malyukin, B. I. Minkov, R. S. Borisov, V. P. Seminozhenko, N. V. Znamenskiĭ, É. A. Manykin, D. V. Marchenko, and E. A. Petrenko, *Fiz. Nizk. Temp.* **24**, 571 (1998) [*Low Temp. Phys.* **24**, 432 (1998)].

¹⁴I. B. Bersuker, *Electronic Structure and Properties of Coordination Compounds* [in Russian], Khimiya, Leningrad (1986).

¹⁵M. Grinberg, A. Mandelis, and K. Fjeldsted, and A. Othonos, *Phys. Rev. B* **48**, 5922 (1993).

¹⁶M. Grinberg, A. Mandelis, and K. Fjeldsted, and A. Othonos, *Phys. Rev. B* **48**, 5935 (1993).

¹⁷Yu. K. Voron'ko, T. G. Mamedov, V. V. Osiko, M. I. Timoshechkin, and I. A. Shcherbakov, *Zh. Éksp. Teor. Fiz.* **65**, 1141 (1973) [*Sov. Phys. JETP* **38**, 565 (1974)].

¹⁸R. M. Hochstrasser, *Molecular Aspects of Symmetry* [Benjamin, New York (1966); Mir, Moscow (1969)].

Translated by Steve Torstveit

PHYSICAL PROPERTIES OF CRYOCRYSTALS

On the structureless shape of the optical absorption bands of the β -oxygen cryocrystal

V. M. Loktev*

*N. N. Bogolyubov Institute of Theoretical Physics, National Academy of Sciences of Ukraine,
ul. Metrologicheskaya 14-b, 03143 Kiev, Ukraine*

S. G. Sharapov

*N. N. Bogolyubov Institute of Theoretical Physics, National Academy of Sciences of Ukraine, ul.
Metrologicheskaya 14-b, 03143 Kiev, Ukraine; "Kiev Polytechnical Institute" National Technical University
of Ukraine, pr. Pobedy 37, 02056 Kiev, Ukraine*

(Submitted April 17, 2000; revised June 13, 2000)

Fiz. Nizk. Temp. **26**, 1214–1225 (December 2000)

An attempt is made to calculate the absorption spectrum of the β phase of solid oxygen with allowance for the absence of long-range magnetic order in it. It is shown that the correlational character of the spin ordering in β -O₂ leads to a substantial change in the spectral function describing the electronic spectrum of this cryocrystal and, as a consequence, results in a loss of the fine structure of the corresponding optical absorption bands, which become broad and structureless. © 2000 American Institute of Physics. [S1063-777X(00)00712-X]

INTRODUCTION

As we know (see Part III of Ref. 1), the O₂ molecule, owing to its unfilled outer (valence) electron shell (two electrons in a twofold degenerate π_g orbital), has, according to Hund's rule, an uncompensated electron spin in the electronic ground state. As a result, unlike the majority of other extremely simple cryocrystals, the intermolecular interaction in solid oxygen is largely determined by the valence (exchange) component, which makes for a collinear orientation of the O₂ molecule and also for spin ordering in its high-temperature monoclinic α and rhombohedral β modifications ($T < T_{\alpha\beta} = 23.8$ K and $T_{\alpha\beta} \leq T \leq T_{\beta\gamma} = 43.8$ K, where $T_{\alpha\beta}$ and $T_{\beta\gamma}$ are the temperatures of the magnetostructural $\alpha\beta$ and $\beta\gamma$ transformations, respectively).

While the crystal structure of α -, β -, and γ -O₂ are known and have been fairly well studied (see, e.g., Refs. 2 and 3), in regard to the magnetic order this can be said only about α -O₂, which is a two-sublattice biaxial antiferromagnet (AFM),^{2,4} the easy axis of which lies along the monoclinic axis of its lattice. The high-temperature cubic γ phase is paramagnetic (PM); this phase also lacks collinearity of the axes of the molecules. As to the magnetism of the β phase, the available information about it for a long time remained of a contradictory nature. On the one hand, many experimental (in particular, spectral) results indicate that β -oxygen should be classified as a paramagnetic system.^{5–7} On the other hand, the temperature dependence of the static magnetic susceptibility explicitly attests to the AFM ordering in β -O₂ (Refs. 8 and 9), as has been independently confirmed by the presence of a peak (albeit strongly smeared) in the neutron-scattering spectrum.^{10–12}

This contradiction was to a certain extent eliminated by one of the present authors, who showed that to a first approximation in which only the strong AFM exchange be-

tween nearest-neighbor molecules aligned along the threefold symmetry axis is taken into account and in which the sign of the intramolecular "spin-axis" coupling constant A_{s-a} is specified (as positive), β -O₂ can be treated as a set of weakly coupled hexagonal planes with three magnetic sublattices.¹³ Here the angles between neighboring spins of different sublattices are $\pm 2\pi/3$, and the magnetic properties of the system as a whole are isomorphic to the well-known XY model and can be described in the framework of that model. Although the three-sublattice magnetic structure of β -oxygen (sometimes called the Loktev structure) was acknowledged and had been studied in a number of papers (see, e.g., Refs. 14–18), the final answer to the question of its total magnetocrystalline symmetry was given only relatively recently.^{19,20}

It was shown^{19,20} that the ground-state energy of the Loktev structure is degenerate with respect to any uniform rotations of the spin vectors \mathbf{S}_n in the basal plane (\mathbf{n} is the vector of a site of the planar lattice). It is known that for such a case the continuous degeneracy in the 2D system causes destruction of the long-range (dipolar) order in the system at all $T \neq 0$, which is formally expressed as the fact that $\langle \mathbf{S}_n \rangle = 0$, or

$$\langle S_n^j S_m^k \rangle \rightarrow 0, \quad |\mathbf{n} - \mathbf{m}| \rightarrow \infty, \quad (1)$$

where $\langle \dots \rangle$ denotes a mathematical averaging, and j, k are the spin projections. Indeed, the absence of an average spin corresponds to paramagnetism, but the nonzero spin correlation functions (1) at short distances argue in favor of ordering, at least of a short-range nature. Moreover, this order can be organized in such a way that the magnetic symmetry of the system on the whole at any finite temperature is lower than the symmetry of the true PM state.²¹ It is this type of

ordering, which is called correlational ordering and is characterized²⁰ by its own order parameter, that is realized in β -O₂.

What we have said is clearly sufficient to warrant a separate treatment of those properties of the β phase of solid O₂ which are governed by the magnetic subsystem. First among these should no doubt be the electronic (excitonic) properties and the optical spectra corresponding to them.

Experimental studies of these spectra, the most completely of which are those of Prikhot'ko and co-workers^{6,22–24} and Eremenko and co-workers,^{5,25,26} demonstrated convincingly that while the absorption bands (of both the mono- and bimolecular natures) of the α phase are discrete, with a highly developed fine structure that is preserved practically without visible changes all the way to $T = T_{\alpha\beta}$, this fine structure literally vanishes after the $\alpha\beta$ transition, these bands becoming very smeared. Completely structureless contours of the absorption bands are also characteristic of γ -O₂, which, however, can be explained (at least in principle) as being due to the characteristic orientational disorder of the molecules in this modification. The radical transformation of the electronic spectra¹ at the $\alpha\beta$ transition, which is expressed in an abrupt change in the shape of the bands, cannot be attributed to its monoclinic distortion nor to critical broadening of the spectral linewidths, which occurs only in the immediate vicinity of the transition point.^{27,28} In our opinion this transformation is a direct consequence of a change in the character of the magnetic order in the system. This is not so much because of the change of the type or, equivalently, the wave vector \mathbf{Q}_{mag} of the planar magnetic structure [for example, from two sublattices with $\mathbf{Q}_{\text{mag}}^{(2)} = (\pi/\sqrt{3}, \pi)$ to three sublattices with $\mathbf{Q}_{\text{mag}}^{(3)} = (2\pi/\sqrt{3}, 2\pi/3)$]²⁹ as it is a result of the loss of long-range order and its transformation into correlational order with the properties in (1). Contributing to this, of course, is the increasing two-dimensionality of the magnetic subsystem of the oxygen cryocrystal upon transition from the α to the β phase and the easy-plane nature (for the structures of these phases) of the rather strong intrinsic magnetic anisotropy of the O₂ molecule, which, as we have said, holds the spin of the molecule in the basal plane of these phases.

Below, for the example of β -O₂, we attempt to calculate the optical spectrum in the region of the one-exciton transition of a crystal having correlational magnetic ordering.

2. SPECTRUM OF ELECTRONIC EXCITATIONS OF β -OXYGEN

In AFM insulators, the excited states corresponding to transitions (one- and two-center) of electrons inside the unfilled shells of PM ions (molecules) are small-radius states, or Frenkel excitons. Complete and detailed studies of the spectra of these excitations have been carried out essentially only for the simplest case, that of crystals with two magnetic sublattices possessing long-range order.^{30–32} The intermediate phase of solid O₂ is an example of a different kind of magnetic structure, the excitonic spectrum of which, as far as we are aware, has not been calculated even for $T=0$.

To investigate it, let us limit consideration to a model crystal whose molecules, like O₂, have a twofold degenerate outer shell containing two electrons. If, for the sake of sim-

plicity, we take into account only one-electron excited states of only one type, then the excitonic spectrum of such a magnetic crystal can be described by the Hamiltonian^{1,32}

$$\mathcal{H} = \mathcal{H}_{SM} + \mathcal{H}_{\text{res}} + \mathcal{H}_{\text{exch}}, \quad (2)$$

in which

$$\mathcal{H}_{SM} = -\frac{\Delta\varepsilon}{2} \sum_{\mathbf{n}_\alpha} \mathbf{S}_{\mathbf{n}_\alpha}^2 \quad (3)$$

is the operator of the intramolecular single-particle states, which corresponds to the model of an oriented gas in the theory of molecular excitons,³³

$$\mathcal{H}_{\text{res}} = -\frac{t}{2} \sum_{\substack{\mathbf{n}_\alpha, \rho_{\alpha\beta} \\ (\alpha \neq \beta)}} \sigma_{\mathbf{n}_\alpha} \sigma_{\mathbf{n}_\alpha + \rho_{\alpha\beta}} \quad (4)$$

is the operator representing the resonant interaction between electronically excited molecules, and

$$\mathcal{H}_{\text{exch}} = \frac{J}{2} \sum_{\substack{\mathbf{n}_\alpha, \rho_{\alpha\beta} \\ (\alpha \neq \beta)}} \mathbf{S}_{\mathbf{n}_\alpha} \mathbf{S}_{\mathbf{n}_\alpha + \rho_{\alpha\beta}} \quad (5)$$

is the intermolecular exchange interaction operator.² In Eqs. (2)–(5) the following notation was used: $\Delta\varepsilon$ is the energy of the excited electronic state of the molecule, t and J are the resonant and exchange integral for the nearest neighbors from different sublattices, separated by a vector $\rho_{\alpha\beta}$, $\mathbf{S}_{\mathbf{n}_\alpha}$ is the spin operator, $\sigma_{\mathbf{n}_\alpha}$ is a pseudospin operator, which, in distinction to $\mathbf{S}_{\mathbf{n}_\alpha}$, specifies transitions between states with different multiplicities (in this case, between the ground triplet $S=1$ and the excited single $S=0$), and α, β ($=1, 2, 3$) are the indices of the magnetic sublattices. In Hamiltonian (2) we have dropped the Hamiltonian of the easy-plane magnetic anisotropy, which is given by the ‘‘spin–axis’’ coupling operator $A_{s-a}(\mathbf{S}_{\mathbf{n}_\alpha}^Y)^2$ in the molecule (where the axis Y is along the molecular axis) and does not contribute directly to the optical properties we are interested in.

The operators $\sigma_{\mathbf{n}_\alpha}$ obey the following commutation relations:

$$\begin{aligned} [\sigma_{\mathbf{n}_\alpha}^j, \sigma_{\mathbf{m}_\beta}^k] &= [S_{\mathbf{n}_\alpha}^j, S_{\mathbf{m}_\beta}^k]; \\ [\sigma_{\mathbf{n}_\alpha}^j, S_{\mathbf{m}_\beta}^k] &= i \delta_{\mathbf{n}_\alpha \mathbf{m}_\beta} \varepsilon_{jkl} \sigma_{\mathbf{n}_\alpha}^l, \end{aligned} \quad (6)$$

where δ_{jk} is the Kronecker delta, and ε_{jkl} is the completely antisymmetric unit tensor.

Hamiltonian (2) is written in the laboratory reference frame, but for the physical system under study, whose magnetic structure by assumption has three spin sublattices, the quantization axis of each sublattice being directed at angles of 120° to one another, it is convenient to use proper frames that take this circumstance into account. We choose an orientation of the coordinate system in the laboratory frame such that the X and Z axes specify the plane on which the average magnetization lies, while the Y axis explores the direction perpendicular to it (i.e., along the threefold axis of the rhombohedron). The transition to the proper axes of quantization for the physical situation under study is effected by the matrix

$$\begin{pmatrix} \cos \varphi_{\mathbf{n}_\alpha} & 0 & \sin \varphi_{\mathbf{n}_\alpha} \\ 0 & 1 & 0 \\ -\sin \varphi_{\mathbf{n}_\alpha} & 0 & \cos \varphi_{\mathbf{n}_\alpha} \end{pmatrix} \quad (7)$$

of ‘‘plane’’ rotations that take $\boldsymbol{\sigma}_{\mathbf{n}_\alpha} = (\sigma_{\mathbf{n}_\alpha}^X, \sigma_{\mathbf{n}_\alpha}^Y, \sigma_{\mathbf{n}_\alpha}^Z)$ and $\mathbf{S}_{\mathbf{n}_\alpha} = (S_{\mathbf{n}_\alpha}^X, S_{\mathbf{n}_\alpha}^Y, S_{\mathbf{n}_\alpha}^Z)$ into $\boldsymbol{\sigma}_{\mathbf{n}_\alpha} = (\sigma_{\mathbf{n}_\alpha}^\xi, \sigma_{\mathbf{n}_\alpha}^\eta, \sigma_{\mathbf{n}_\alpha}^\zeta)$ and $\mathbf{S}_{\mathbf{n}_\alpha} = (S_{\mathbf{n}_\alpha}^\xi, S_{\mathbf{n}_\alpha}^\eta, S_{\mathbf{n}_\alpha}^\zeta)$ while preserving the commutation relations (6); it is assumed below that the proper axis for each spin is $\zeta_{\mathbf{n}_\alpha}$.

Making the transformation (7) and substituting the corresponding operators into Hamiltonians (4) and (5), we obtain the following expressions for the latter:

$$\begin{aligned} \mathcal{H}_{\text{res}} = & -\frac{t}{2} \sum_{\substack{\mathbf{n}_\alpha, \boldsymbol{\rho}_{\alpha\beta} \\ (\alpha \neq \beta)}} [(\sigma_{\mathbf{n}_\alpha}^\xi \sigma_{\mathbf{n}_\alpha + \boldsymbol{\rho}_{\alpha\beta}}^\xi + \sigma_{\mathbf{n}_\alpha}^\zeta \sigma_{\mathbf{n}_\alpha + \boldsymbol{\rho}_{\alpha\beta}}^\zeta) \\ & \times \cos(\varphi_{\mathbf{n}_\alpha} - \varphi_{\mathbf{n}_\alpha + \boldsymbol{\rho}_{\alpha\beta}}) + \sigma_{\mathbf{n}_\alpha}^\eta \sigma_{\mathbf{n}_\alpha + \boldsymbol{\rho}_{\alpha\beta}}^\eta \\ & + (\sigma_{\mathbf{n}_\alpha}^\xi \sigma_{\mathbf{n}_\alpha + \boldsymbol{\rho}_{\alpha\beta}}^\zeta + \sigma_{\mathbf{n}_\alpha}^\zeta \sigma_{\mathbf{n}_\alpha + \boldsymbol{\rho}_{\alpha\beta}}^\xi) \\ & \times \sin(\varphi_{\mathbf{n}_\alpha} - \varphi_{\mathbf{n}_\alpha + \boldsymbol{\rho}_{\alpha\beta}})]; \end{aligned} \quad (8)$$

$$\begin{aligned} \mathcal{H}_{\text{exch}} = & \frac{J}{2} \sum_{\substack{\mathbf{n}_\alpha, \boldsymbol{\rho}_{\alpha\beta} \\ (\alpha \neq \beta)}} [(S_{\mathbf{n}_\alpha}^\xi S_{\mathbf{n}_\alpha + \boldsymbol{\rho}_{\alpha\beta}}^\xi + S_{\mathbf{n}_\alpha}^\zeta S_{\mathbf{n}_\alpha + \boldsymbol{\rho}_{\alpha\beta}}^\zeta) \\ & \times \cos(\varphi_{\mathbf{n}_\alpha} - \varphi_{\mathbf{n}_\alpha + \boldsymbol{\rho}_{\alpha\beta}}) + S_{\mathbf{n}_\alpha}^\eta S_{\mathbf{n}_\alpha + \boldsymbol{\rho}_{\alpha\beta}}^\eta \\ & + (S_{\mathbf{n}_\alpha}^\xi S_{\mathbf{n}_\alpha + \boldsymbol{\rho}_{\alpha\beta}}^\zeta + S_{\mathbf{n}_\alpha}^\zeta S_{\mathbf{n}_\alpha + \boldsymbol{\rho}_{\alpha\beta}}^\xi) \\ & \times \sin(\varphi_{\mathbf{n}_\alpha} - \varphi_{\mathbf{n}_\alpha + \boldsymbol{\rho}_{\alpha\beta}})], \end{aligned} \quad (9)$$

the mean-field structure of which, as one can readily verify, is analogous to the Hamiltonian of the XY model. This is most clearly seen in the quasiclassical approximation, in which it is assumed that $S_{\mathbf{n}_\alpha}^\zeta = \langle S_{\mathbf{n}_\alpha}^\zeta \rangle \equiv s$ (cf. Eq. (1), where the average refers to the laboratory frame) and $\langle S_{\mathbf{n}_\alpha}^{\xi, \eta} \rangle = 0$ (Ref. 34), as a result of which the operator (9) takes on the standard form for this model:

$$\mathcal{H}_{\text{exch}} \rightarrow \mathcal{H}_{\text{exch}}^{XY} = \frac{Js^2}{2} \sum_{\substack{\mathbf{n}_\alpha, \boldsymbol{\rho}_{\alpha\beta} \\ (\alpha \neq \beta)}} \cos(\varphi_{\mathbf{n}_\alpha} - \varphi_{\mathbf{n}_\alpha + \boldsymbol{\rho}_{\alpha\beta}}). \quad (10)$$

As to the pseudospin operators, a similar approximation for them (or some sort of nontrivial averages³⁾ cannot be introduced, since they describe transitions between the ground (triplet) and excited (singlet) states. One can, however, simplify expression (9) substantially by taking the following circumstance into account: the operators $\boldsymbol{\sigma}_{\mathbf{n}_\alpha}^+ = 2^{-1/2}(\boldsymbol{\sigma}_{\mathbf{n}_\alpha}^\xi \pm i \boldsymbol{\sigma}_{\mathbf{n}_\alpha}^\eta)$ and $\sigma_{\mathbf{n}_\alpha}^\zeta$ can be represented (see Refs. 1 and 32) by the creation $B_{\mathbf{n}_\alpha}^+(S_Z)$ and annihilation $B_{\mathbf{n}_\alpha}(S_Z)$ operators for excitations at each sublevel $S_Z = \pm 1, 0$ of the ground spin multiplet. Among these it is important to consider only the lowest (in the proper frame) sublevel, with $S_Z = 1$, since the other two ($S_Z = 0$ and $S_Z = -1$) are just spin-excited states, the electronic transitions from which in one way or other involve the participation of spin excitations (magnons), which can be neglected in a calculation of the excitonic bands. Here the component $\sigma_{\mathbf{n}_\alpha}^\zeta$, which contains

only the operators $B_{\mathbf{n}_\alpha}(0)$ and $B_{\mathbf{n}_\alpha}^+(0)$, in a first approximation (a calculation of the energy bands of noninteracting excitons and magnons) do not contribute and can be omitted; the same is also true for the operators $B_{\mathbf{n}_\alpha}(-1)$ and $B_{\mathbf{n}_\alpha}^+(-1)$. The details of the transformations from the pseudospin operators to the second-quantization operators (i.e., the transition operators) are set forth in Ref. 1.

In the stated approximations the Hamiltonian of free electronic excitations moving along an AFM insulator whose spin subsystem corresponds to the quasiclassical approach does indeed take the standard form:

$$\mathcal{H}_{\text{res}} \rightarrow \mathcal{H}_{\text{res}}^{XY} = -\frac{t}{2} \sum_{\substack{\mathbf{n}_\alpha, \boldsymbol{\rho}_{\alpha\beta} \\ (\alpha \neq \beta)}} B_{\mathbf{n}_\alpha}^+ B_{\mathbf{n}_\alpha + \boldsymbol{\rho}_{\alpha\beta}} \cos^2 \frac{\varphi_{\mathbf{n}_\alpha} - \varphi_{\mathbf{n}_\alpha + \boldsymbol{\rho}_{\alpha\beta}}}{2}, \quad (11)$$

where the operators $B_{\mathbf{n}_\alpha}^+$ and $B_{\mathbf{n}_\alpha}$, corresponding to $S_Z = 1$, can now to a good approximation (see Refs. 31–33) be assumed to be Bose operators. In Eq. (11) we have dropped the nonresonant terms, which in the investigated (exciton) region of the spectrum give a vanishingly small ($\sim t^2/\Delta\varepsilon$; Ref. 33) contribution to the energy.

Without restricting the generality we assume that the angles of rotation of the spins of each site, $\varphi_{\mathbf{n}_\alpha}$ are related to the rotation angle $\varphi_{\mathbf{n}}$, which characterizes the cell as a whole, in such a way that $\varphi_{\mathbf{n}_\alpha} = \varphi_{\mathbf{n}} + 2\pi(\alpha - 1)/3$. This allows us to consider both a system with long-range ($T=0$) order, for which $\varphi_{\mathbf{n}_\alpha} - \varphi_{\mathbf{n}_\alpha + \boldsymbol{\rho}_{\alpha\beta}} = 2\pi(\alpha - \beta)/3$, and a system without it, when

$$\varphi_{\mathbf{n}_\alpha} - \varphi_{\mathbf{n}_\alpha + \boldsymbol{\rho}_{\alpha\beta}} = 2\pi(\alpha - \beta)/3 - \nabla \varphi_{\mathbf{n}_\alpha} \boldsymbol{\rho}_{\alpha\beta} + \dots$$

The first case admits calculation of the excitonic spectrum in the three-sublattice magnetic structure of $\beta\text{-O}_2$ by direct diagonalization of Hamiltonian (11). Assuming that $\varphi_{\mathbf{n}_\alpha} - \varphi_{\mathbf{n}_\alpha + \boldsymbol{\rho}_{\alpha\beta}} = \pm 2\pi/3$ and transforming to the \mathbf{k} representation, we obtain the exciton Hamiltonian of a hexagonal plane in the form⁴⁾

$$\begin{aligned} \mathcal{H}_{\text{ex}} = \mathcal{H}_{SM} + \mathcal{H}_{\text{ex}} = \Delta\varepsilon \sum_{\mathbf{k}} B_{\mathbf{k}\alpha}^+ B_{\mathbf{k}\alpha} \\ - \frac{tz}{4} \sum_{\mathbf{k}} \sum_{\alpha \neq \beta} [\gamma(\mathbf{k}) B_{\mathbf{k}\alpha}^+ B_{\mathbf{k}\beta} + \text{h.c.}], \end{aligned} \quad (12)$$

$$\gamma(\mathbf{k}) = \frac{1}{z} \left(2e^{ik_x(a/2)} \cos \frac{\sqrt{3}}{2} k_z a + e^{-ik_x a} \right),$$

which is brought to diagonal form by the transformation

$$\begin{pmatrix} B_1(\mathbf{k}) \\ B_2(\mathbf{k}) \\ B_3(\mathbf{k}) \end{pmatrix} = \frac{1}{3^{1/2}} \begin{pmatrix} 1 & 1 & 1 \\ 1 & \varepsilon & \varepsilon^2 \\ 1 & \varepsilon^2 & \varepsilon \end{pmatrix} \begin{pmatrix} B_{\mathbf{k}1} \\ B_{\mathbf{k}2} \\ B_{\mathbf{k}3} \end{pmatrix}, \quad (13)$$

$$\varepsilon \equiv \exp(2\pi i/3).$$

In Eq. (12) we have used the notation $z = 3$ for the number of nearest neighbors belonging to another magnetic sublattice, and a for the lattice constant of the triangular lattice. Direct substitution of (13) into (12) gives

$$\begin{aligned}\mathcal{H}_{\text{ex}} &= \sum_{\mathbf{k}, \mu=1,2,3} \varepsilon_{\mu}(\mathbf{k}) B_{\mu}^{+}(\mathbf{k}) B_{\mu}(\mathbf{k}); \\ \varepsilon_1(\mathbf{k}) &\equiv \varepsilon_A(\mathbf{k}) = \Delta\varepsilon - tz \operatorname{Re} \gamma(\mathbf{k}); \\ \varepsilon_{2,3}(\mathbf{k}) &\equiv \varepsilon_E(\mathbf{k}) = \Delta\varepsilon + \frac{tz}{2} [\operatorname{Re} \gamma(\mathbf{k}) + \sqrt{3} \operatorname{Im} \gamma(\mathbf{k})].\end{aligned}\quad (14)$$

Thus the excitonic spectrum of the β phase consists of three bands of A and E symmetry, the last two being degenerate. For the region of small wave vectors ($\mathbf{k} \cdot \mathbf{a} \ll 1$) we easily find from (14) that

$$\begin{aligned}\varepsilon_A(\mathbf{k}) &= \Delta\varepsilon - tz \left(1 - \frac{1}{4} \mathbf{k}^2 \mathbf{a}^2 \right) = \Delta\varepsilon_A + \frac{\mathbf{k}^2}{2m_A^*}, \\ \varepsilon_E(\mathbf{k}) &= \Delta\varepsilon - \frac{tz}{2} \left(1 - \frac{1}{4} \mathbf{k}^2 \mathbf{a}^2 \right) = \Delta\varepsilon_E + \frac{\mathbf{k}^2}{2m_E^*},\end{aligned}\quad (15)$$

where $\Delta\varepsilon_A \equiv \Delta\varepsilon - tz$ and $\Delta\varepsilon_E \equiv \Delta\varepsilon - tz/2$ are the energies of the states corresponding to $\mathbf{k}=0$, and $m_A^* = m_E^*/2 = 2/tza^2$ are the effective masses of the A and E excitons.

3. INCLUSION OF THE CORRELATIONAL ORDERING

If there is no long-range (including 2D) order in the system, it becomes impossible simply to find the energy of the excitonic excitations. One can, however, find the spectral density (spectral function) describing, in particular, the absorption spectrum in the region of an excitonic transition. For this it is necessary to calculate (see Ref. 33) the exciton Green function G_{ex} .

The explicit expression for the Green function is determined by the form of the operator $W(t)$ of the interaction of β -O₂ with an incident electromagnetic wave with frequency ω and wave vector \mathbf{Q} . Since in the O₂ molecule all of the lowest one-electron transitions are dipole-forbidden as a consequence of the intercombination forbiddenness, to make them allowed it is necessary to invoke the spin-orbit interaction. Taking the latter into account leads to the following expression for $W(t)$:¹

$$W(t) = \sum_{\mathbf{n}_{\alpha}} h_{\text{eff}}^{+} e^{i(\mathbf{Q}\cdot\mathbf{n}-\omega t)} (\sigma_{\mathbf{n}_{\alpha}}^X - i\sigma_{\mathbf{n}_{\alpha}}^Z) + \text{h.c.}, \quad (16)$$

where h_{eff}^{+} is the effective amplitude of the magnetic field of the wave with a polarization rotating in the basal plane. Then using (7) and the transformation (13), we easily find from (16) that

$$\begin{aligned}W(t) &= h_{\text{eff}}^{+} e^{-i\omega t} \sum_{\mathbf{n}} e^{i\mathbf{Q}\cdot\mathbf{n}} e^{i\varphi_{\mathbf{n}}} (B_{\mathbf{n}1}^{+} + \varepsilon B_{\mathbf{n}2}^{+} + \varepsilon^2 B_{\mathbf{n}3}^{+}) + \text{h.c.} \\ &\equiv h_{\text{eff}}^{+} e^{-i\omega t} \sum_{\mathbf{n}} e^{i\mathbf{Q}\cdot\mathbf{n}} e^{i\varphi_{\mathbf{n}}} B_2^{+}(\mathbf{n}) + \text{h.c.} .\end{aligned}\quad (17)$$

It follows from this expression that in β -O₂ light excites only long-wavelength ($\mathbf{Q} \cdot \mathbf{a} \ll 1$) degenerate states of E symmetry, and each component of the doublet is excited by ‘‘its own’’ — right- or left-polarized — wave (this will allow us to drop the excitonic subband index μ below).

At $T=0$ the absorption spectrum should then have a narrow (in the limit, δ -function-like) peak corresponding to the frequency $\omega = \varepsilon_E(\mathbf{Q}) \approx \varepsilon_E(0)$. But if $T \neq 0$ and the angles

$\varphi_{\mathbf{n}}$ are even slightly different, then expression (17) indicates that the simplest form of conservation law is violated, and it is no longer the case that only the itinerant states with $\mathbf{k} = \mathbf{Q}$ can be excited; consequently, the spectrum should lose its δ -function-like character. As we know (see, e.g., Ref. 33), for calculating the line shape at finite T it is more convenient to use the Matsubara Green functions, which, as applicable to (17), can be determined by the expression

$$\begin{aligned}G_{\text{ex}}(\mathbf{n}, \tau) &= G_{\text{ex}}(\mathbf{n}, \tau + \beta) \\ &= -\langle B(\mathbf{n}, \tau) e^{i\varphi_{\mathbf{n}}(\tau)} B^{+}(0,0) e^{-i\varphi_0(0)} \rangle \\ &\approx G_{\text{ex}}^{(0)}(\mathbf{n}, \tau) D_{\text{cor}}(\mathbf{n}, \tau),\end{aligned}\quad (18)$$

where

$$G_{\text{ex}}^{(0)}(\mathbf{n}, \tau) = -\langle B(\mathbf{n}, \tau) B^{+}(0,0) \rangle \quad (19)$$

is the purely excitonic Green function for the E states in the coordinate representation (τ is the imaginary time, $\beta=1/T$), and

$$D_{\text{cor}}(\mathbf{n}, \tau) = \langle e^{i\varphi_{\mathbf{n}}(\tau)} e^{-i\varphi_0(0)} \rangle \quad (20)$$

is the spin correlation function, the form of which must be chosen from physical considerations. The factorization of the total Green function (18) is approximate and corresponds to neglecting the last term in the Hamiltonian (9); that term describes the mutual conversion of spin and phase fluctuations and can be assumed to be unimportant in the long-wavelength approach used here.

Since the desired Green function (18) is represented by a product, its frequency-momentum representation is transformed into a convolution:

$$\begin{aligned}G_{\text{ex}}(\mathbf{k}, i\Omega_n) &= T \sum_{m=-\infty}^{\infty} \int \frac{d^2p}{(2\pi)^2} G_{\text{ex}}^{(0)}(\mathbf{p}, i\Omega_m) D_{\text{cor}} \\ &\quad \times (\mathbf{k}-\mathbf{p}, i\Omega_n - i\Omega_m),\end{aligned}\quad (21)$$

where

$$G_{\text{ex}}^{(0)}(\mathbf{k}, i\Omega_n) = \frac{1}{i\Omega_n - \varepsilon(\mathbf{k})} \quad (22)$$

is the Fourier transform of the function (19), in which $\Omega_n = 2\pi Tn$ is the Matsubara Bose frequency, $\varepsilon(\mathbf{k})$ is given in (15), and

$$D_{\text{cor}}(\mathbf{q}, i\Omega_n) = \int_0^{\beta} d\tau \sum_{\mathbf{n}} e^{i\Omega_n \tau - i\mathbf{q}\cdot\mathbf{n}} D_{\text{cor}}(\mathbf{n}, \tau) \quad (23)$$

is the Fourier transform of the function (20).

While the expression for $G_{\text{ex}}^{(0)}(\mathbf{n}, \tau)$ can be reconstructed from its known Fourier transform (22), only the asymptotic behavior is known for the function $D_{\text{cor}}(\mathbf{n}, \tau)$ [e.g., relations of the type in (1)]. Its space-time behavior is determined by the structure of the spin ground state of the system. In particular, for the quasiclassical 2D XY model (10) the form of the correlation function (20) is given by the function³⁵

$$D_{\text{cor}}(\mathbf{r}) = \left(\frac{a}{r} \right)^{T/2\pi J s^2} \exp\left(-\frac{r}{\xi_{\text{mag}}(T)} \right), \quad (24)$$

which corresponds to static magnetic spatial fluctuations with a correlation length $\xi_{\text{mag}}(T)$ given by³⁶

$$\xi_{\text{mag}}(T) = \begin{cases} \infty, & T < T_{BKT}; \\ a \exp(b/\sqrt{T - T_{BKT}}), & T \geq T_{BKT}, \end{cases} \quad (25)$$

where a , as above, corresponds to the lattice parameter, b is some constant, and $T_{BKT} \approx (\pi/2)Js^2$ is the Berezinskiĭ–Kosterlitz–Thouless transition temperature, which for the given XY model is related to the dissociation of vortical spin excitations. For $T < T_{BKT}$ these excitations are bound into pairs, so that $\xi_{\text{mag}}(T < T_{BKT}) = \infty$, and the correlations fall off algebraically. As the temperature is raised, however, the vortices depair, leading to an exponential damping of the correlations, and the temperature dependence of ξ_{mag} has the very characteristic form (25).

Since the $\alpha\beta$ transition is not only magnetic but also structural, one is apparently unjustified in assuming that the temperature T_{BKT} (even under the assumption that such a transition exists in the magnetic system of β -oxygen itself) can have anything in common with $T_{\alpha\beta}$. Most likely the temperature T_{BKT} ($< T_{\alpha\beta}$) is of a more abstract arbitrary character, specifying the point at which $\xi_{\text{mag}}(T_{BKT}) = \infty$ for the three-sublattice structure. Of course, the temperature $T_{\alpha\beta}$ has a direct physical meaning, and here $\xi_{\text{mag}}(T_{\alpha\beta})$, which may or may not obey relation (25), is finite, and on further increase in T this length decreases, so that $\xi_{\text{mag}}(T_{\beta\gamma}) < \xi_{\text{mag}}(T_{\alpha\beta})$.

The Fourier transform (22) for the correction function (24) gives the expression

$$\begin{aligned} D_{\text{cor}}(\mathbf{q}, i\Omega_n) &= \delta_{n0} \frac{2\pi}{T} a^{T/2\pi Js^2} \int_0^\infty dr r^{1-T/2\pi Js^2} J_0(qr) \\ &\quad \times \exp\left(-\frac{r}{\xi_{\text{mag}}(T)}\right) \\ &= \delta_{n0} \frac{2\pi}{T} \frac{a^{2(1-\alpha)} \xi_{\text{mag}}^{2\alpha}(T)}{[1 + q^2 \xi_{\text{mag}}^2(T)]^\alpha} \Gamma(2\alpha) F \\ &\quad \times \left(\alpha, -\alpha + \frac{1}{2}; 1; \frac{q^2 \xi_{\text{mag}}^2(T)}{1 + q^2 \xi_{\text{mag}}^2(T)}\right), \end{aligned} \quad (26)$$

in which $J_0(x)$ is the Bessel function of order zero, $\Gamma(x)$ is the gamma function, $F(a, b; c; z)$ is the hypergeometric function, and we have introduced the parameter

$$\alpha = 1 - \frac{T}{4\pi Js^2} \equiv 1 - \frac{1}{8} \frac{T}{T_{BKT}}. \quad (27)$$

Since $F(a, b; c; z)$ in (26) is a slowly varying function of the variable z , we assign that variable the value $z=1$ (which corresponds to $q \rightarrow \infty$). In that case

$$\begin{aligned} D_{\text{cor}}(\mathbf{q}, i\Omega_n) &= \delta_{n0} \frac{D_0}{T} \left[\frac{\xi_{\text{mag}}^2(T)}{1 + q^2 \xi_{\text{mag}}^2(T)} \right]^\alpha, \\ D_0 &\equiv \frac{4\pi\Gamma(\alpha)}{\Gamma(1-\alpha)} \left(\frac{2}{a}\right)^{2(\alpha-1)}. \end{aligned} \quad (28)$$

We emphasize that the use of the argument $z=1$ in the hypergeometric function ensures a physically important correspondence: for $\xi_{\text{max}}^{-1}(T)=0$ expression (28) is the exact Fourier transform of the correlation function (24).

Knowing (28), we can attempt to write a more general phenomenological form than (24) for the correlation function of the spin fluctuations, starting from its frequency–momentum representation. Indeed, let this correlation have the form [cf. Eq. (28)]

$$\begin{aligned} D_{\text{mag}}(\mathbf{q}, i\Omega_n) &= \frac{D_0 c_{\text{mag}}^{2\alpha}}{T [c_{\text{mag}}^2 \mathbf{q}^2 + c_{\text{mag}}^2 \xi_{\text{mag}}^{-2}(T) + \Omega_n^2 + 2\Gamma_{\text{mag}} |\Omega_n|]^\alpha}, \end{aligned} \quad (29)$$

in which c_{mag} and Γ_{mag} are the magnon velocity and damping constant (recall that in view of the continuous degeneracy the spectrum of $\beta\text{-O}_2$, on the assumption that it has long-range magnetic order, contains a Goldstone spin mode³⁷). Then, taking the inverse Fourier transform with respect to frequencies, one can easily obtain an expression for the retarded Green function corresponding to (29):

$$\begin{aligned} D_{\text{cor}}^R(\mathbf{q}, t \rightarrow \infty) &\sim \begin{cases} t^{\alpha-1} e^{-\Gamma_{\text{mag}} t}, & c_{\text{mag}}^2 q^2 > \Gamma_{\text{mag}}^2 - c_{\text{mag}}^2 \xi_{\text{mag}}^{-2}(T) \\ t^{\alpha-1} e^{-\tilde{\Gamma}_{\text{mag}} t}, & c_{\text{mag}}^2 q^2 < \Gamma_{\text{mag}}^2 - c_{\text{mag}}^2 \xi_{\text{mag}}^{-2}(T), \end{cases} \end{aligned} \quad (30)$$

where

$$\tilde{\Gamma}_{\text{mag}} \equiv \Gamma_{\text{mag}} - \sqrt{\Gamma_{\text{mag}}^2 - c_{\text{mag}}^2 [q^2 + \xi_{\text{mag}}^{-2}(T)]} (> 0).$$

We note that this function, which takes into account the temporal dynamics of the spin correlations, agrees with the correlation function proposed in Ref. 38:

$$D_{\text{cor}}^R(\mathbf{r}, t) = \left(\frac{a}{r}\right)^{T/2\pi Js^2} \exp\left(-\Gamma_{\text{mag}} t - \frac{r}{\xi_{\text{mag}}(T)}\right). \quad (31)$$

Expressions (30) and (31), however, are not physically identical; in particular, the first of them indicates that the rate of decay of magnetic correlations depends on \mathbf{q} . It is minimum for $q=0$ and reaches its maximum value Γ_{mag} when $c_{\text{mag}}^2 q^2 > \Gamma_{\text{mag}}^2 - c_{\text{mag}}^2 \xi_{\text{mag}}^{-2}(T)$. This dependence means that at large distances the spin correlations do not “feel” the vortex excitations, and in this sense the form of (29) is phenomenologically the most general, regardless of the concrete structure of the ground state of the disordered magnetic subsystem (we can mention in this connection that for the 2D XY model one has $\Gamma_{\text{mag}}(T \rightarrow T_{BKT}^+) = 0$).³⁸ We also note that the greatest contribution to the sum over frequencies in (21) is from the term with $n=m$, which directly corresponds to taking the static correlation function (28) into account.

4. CALCULATION OF THE SPECTRAL DENSITY FOR EXCITONS

As we know, the excitonic absorption spectrum is directly determined by the excitonic spectral function $A_{\text{ex}}(\mathbf{Q}, \omega)$, which is proportional to the imaginary part of the Green function:³³

$$A_{\text{ex}}(\mathbf{Q}, \omega) = -\frac{1}{\pi} \text{Im} G_{\text{ex}}(\mathbf{Q}, \omega + i0), \quad (32)$$

with

$$G_{\text{ex}}(\mathbf{Q}, i\Omega_n) = \int_{-\infty}^{\infty} d\omega \frac{A_{\text{ex}}(\mathbf{Q}, \omega)}{i\Omega_n - \omega}, \quad (33)$$

$$G_{\text{ex}}^{(0)}(\mathbf{p}, i\Omega_n) = \int_{-\infty}^{\infty} d\omega \frac{A_{\text{ex}}^{(0)}(\mathbf{p}, \omega)}{i\Omega_n - \omega}.$$

By analogy we can define the corresponding spectral function

$$A_{\text{cor}}(\mathbf{q}, \Omega) = -\frac{1}{\pi} \text{Im} D_{\text{cor}}(\mathbf{q}, \Omega + i0), \quad (34)$$

with

$$D_{\text{cor}}(\mathbf{q}, i\Omega_n) = \int_{-\infty}^{\infty} d\Omega \frac{A_{\text{cor}}(\mathbf{q}, \Omega)}{i\Omega_n - \Omega}. \quad (35)$$

It is easy to show that if the correlational ordering is not taken into account, one has

$$A_{\text{ex}}^{(0)}(\mathbf{k}, \omega) = \delta(\omega - \varepsilon(\mathbf{k})) \quad (36)$$

and, in particular, for $\Gamma_{\text{mag}}=0$ (the dynamic case in the absence of damping)

$$\begin{aligned} A_{\text{cor}}(\mathbf{q}, \Omega) = & -\frac{D_0 c_{\text{mag}}^{2\alpha}}{\pi T} \sin(\pi\alpha) \\ & \times [\Omega^2 - c_{\text{mag}}^2 q^2 - c_{\text{mag}}^2 \xi_{\text{mag}}^{-2}(T)]^{-\alpha} \\ & \times \theta[\Omega^2 - c_{\text{mag}}^2 q^2 - c_{\text{mag}}^2 \xi_{\text{mag}}^{-2}(T)] \text{sgn } \Omega, \end{aligned} \quad (37)$$

where $\theta(x)$ is the step function.

Substituting representations (33) and (35) for the ‘‘partial’’ spectral functions into (21) and summing over frequencies, we find that the total spectral density (32) is expressed by the integral

$$\begin{aligned} A_{\text{ex}}(\mathbf{Q}, \omega) = & \int_{-\infty}^{\infty} d\Omega \left[\frac{1}{1 - e^{\Omega/T}} - \frac{1}{1 - e^{(\Omega - \omega)/T}} \right] \\ & \times \int \frac{d^2 p}{(2\pi)^2} A_{\text{ex}}^{(0)}(\mathbf{p}, \Omega) A_{\text{cor}}(\mathbf{Q} - \mathbf{p}, \omega - \Omega). \end{aligned} \quad (38)$$

We note that in the given form, formula (38) takes into account both the static spin correlations, which can be described using only the correlation function (28), and the dynamic spin corrections, which are contained only in its more general form (29). Below we consider the two cases — static and dynamic — separately, since each of them is of definite interest. This is because, e.g., the first of them admits an exact analytical investigation, while the second, being closer to the real situation, requires the use of numerical integration.

4.1. Static correlations

We have said above that the dynamic correlation function (29) goes over to its static counterpart (28) if only the terms corresponding to $n=0$ are taken into account in (29) or the terms with $n=m$ are included in the sum (21) for the Green function. This same result can be arrived at formally if in (38) after a shift of the integration variable $\Omega \rightarrow \Omega + \omega$, the substitution $\Omega \rightarrow c_{\text{mag}} \Omega$ is made and the limit $c_{\text{mag}} \rightarrow 0$ is taken.³⁹ Then expression (38) is brought to the form

$$\begin{aligned} A_{\text{ex}}(\mathbf{Q}, \omega) = & \frac{1}{\pi} D_0 \sin \pi\alpha \int_{-\infty}^{\infty} \frac{d\Omega}{\Omega} \text{sgn } \Omega \int \frac{d^2 p}{(2\pi)^2} \\ & \times \delta(\omega - \varepsilon(\mathbf{p})) \frac{\theta[\Omega^2 - (\mathbf{Q} - \mathbf{p})^2 - \xi_{\text{mag}}^{-2}(T)]}{[\Omega^2 - (\mathbf{Q} - \mathbf{p})^2 - \xi_{\text{mag}}^{-2}(T)]^\alpha}, \end{aligned} \quad (39)$$

where we have used expressions (36) and (37). After doing the integration over frequency, we arrive at the expression

$$\begin{aligned} A_{\text{ex}}(\mathbf{Q}, \omega) = & D_0 \int \frac{d^2 p}{(2\pi)^2} \delta(\omega - \varepsilon(\mathbf{p})) \frac{1}{[(\mathbf{Q} - \mathbf{p})^2 + \xi_{\text{mag}}^{-2}(T)]^\alpha}, \end{aligned} \quad (40)$$

which, after integration over the angle and the variable q^2 (the latter removes the δ function) and the use of the identity

$$F\left(\alpha, 1 - \alpha; 1; \frac{1 - z}{2}\right) = F\left(\frac{\alpha}{2}, \frac{1 - \alpha}{2}; 1; 1 - z^2\right), \quad (41)$$

can be cast into explicit form:

$$\begin{aligned} A_{\text{ex}}(\mathbf{Q}, \omega) = & \frac{\Gamma(\alpha)}{\Gamma(1 - \alpha)} \left(\frac{2}{m^* a^2}\right)^{\alpha - 1} \frac{1}{D^{\alpha/2}} F\left(\frac{\alpha}{2}, \frac{1 - \alpha}{2}; 1; \right. \\ & \left. - \frac{4\mathbf{Q}^2(\omega - \Delta\varepsilon)/2m^*}{D}\right) \theta(\omega - \Delta\varepsilon), \end{aligned} \quad (42)$$

where

$$D \equiv \left(\Delta\varepsilon + \frac{\mathbf{Q}^2}{2m^*} - \omega + \frac{1}{2m^* \xi_{\text{mag}}^2(T)} \right)^2 + \frac{2(\omega - \Delta\varepsilon)}{m^* \xi_{\text{mag}}^2(T)}, \quad (43)$$

and we have used the notation (15).

The spectral density of the form (42) corresponds to a Green function of the nonpole form;⁴⁰ in particular, for $T < T_{BKT}$, when $\xi_{\text{mag}}^{-1}(T) = 0$ and the magnetic order corresponds to algebraic order, we have

$$G_{\text{ex}}(\mathbf{Q}, \omega) \sim \frac{1}{(\omega - \Delta\varepsilon - \mathbf{Q}^2/2m^*)^{2\alpha - 1}}. \quad (44)$$

We see from (44) that such behavior [see Eq. (27)] is wholly determined by the parameter $\alpha \neq 1$. For $T=0$, when $\alpha=1$, we recover the standard (pole) behavior of the Green function, which corresponds to the presence of long-range order in the system and to a δ -function-like [see Eq. (36)] spectral density $A_{\text{ex}}(\mathbf{Q}, \omega) = A_{\text{ex}}^{(0)}(\mathbf{Q}, \omega)$.⁵⁾

It is interesting to note that the nonpole character of the Green function of the electrons in the theory of superconductivity means that the electrons exhibit non-Fermi-liquid behavior. For excitons this is manifested, as we shall see below, in a strong smearing of the spectral line. It is also possible that the nonpole form (44) can affect the collective behavior of a gas of excitons of a higher density, but that question is beyond the scope of this paper. Nevertheless, the aforementioned broadening effect due to $\alpha \neq 1$ cannot in itself lead to the observed loss of the structure of the optical bands at the $\alpha\beta$ transition; that can be achieved only by invoking a finite magnetic correlation length.

It is appropos here to call attention to the fact that on account of the θ function in (42) the excitonic states in the frequency region $\omega < \Delta\varepsilon$ have no spectral weight; in this case $A_{\text{ex}}(\mathbf{Q}, \omega)$ exhibits a jump at the point $\omega = \Delta\varepsilon$, but this jump is eliminated in the more realistic dynamic case.

4.2. Dynamic correlations

As we have said, expression (14) also describes dynamic corrections, provided that after introducing the shifts $\Omega \rightarrow \Omega + \omega$ and $\mathbf{p} \rightarrow \mathbf{p} + \mathbf{Q}$ we omit taking the limit $c_{\text{mag}} \rightarrow 0$ and use the spectral function (35), which corresponds to the most general form (29) of the spin correlation function. As a result, we obtain

$$A_{\text{ex}}(\mathbf{Q}, \omega) = \frac{D_0 c_{\text{mag}}^{2\alpha}}{\pi T} \int_{-\infty}^{\infty} d\Omega \left[\frac{1}{1 - e^{\Omega/T}} - \frac{1}{1 - e^{(\Omega + \omega)/T}} \right] \times \int \frac{d^2 p}{(2\pi)^2} \delta\left(\frac{(\mathbf{Q} + \mathbf{p})^2}{2m^*} + \Delta\varepsilon - \omega - \Omega\right) \times \text{Im} \frac{1}{[c_{\text{mag}}^2 p^2 + c_{\text{mag}}^2 \xi_{\text{mag}}^{-2}(T) - \Omega^2 + 2i\Gamma_{\text{mag}}\Omega]^\alpha}. \tag{45}$$

Expression (45) can also be simplified if, as above, we remove the δ function (by integrating over angles) and do the integration over the ‘‘energy’’ variable $p^2/2m^*$. We thereby arrive at the final result

$$A_{\text{ex}}(\mathbf{Q}, \omega) = -\frac{1}{2\pi T} \frac{\Gamma(\alpha)}{\Gamma(1-\alpha)} \left(\frac{2}{m^* a^2}\right)^{\alpha-1} \times \int_{-\infty}^{\infty} d\Omega \left[\frac{1}{1 - e^{\Omega/T}} - \frac{1}{1 - e^{(\Omega + \omega)/T}} \right] \times I(\mathbf{Q}, \omega, \Omega) \theta(\Omega + \omega - \Delta\varepsilon), \tag{46}$$

where we have used the following notation:

$$I(\mathbf{Q}, \omega, \Omega) = \text{Im} \left[(\omega_- - a_I - ib_I)^{-\alpha} F \left(\frac{1}{2}, \alpha; 1; \frac{\omega_+ - \omega_-}{a_I + ib_I - \omega_-} \right) \right], \tag{47}$$

$$\omega_{\pm} \equiv \left[\left(\frac{\mathbf{Q}^2}{2m^*} \right)^{1/2} \pm \sqrt{\omega + \Omega + \Delta\varepsilon} \right];$$

$$a_I \equiv \frac{1}{2m^*} \left(\frac{\Omega^2}{c_{\text{mag}}^2} - \frac{1}{\xi_{\text{mag}}^2(T)} \right); \quad b_I \equiv \frac{\Gamma_{\text{mag}}\Omega}{m^* c_{\text{mag}}^2}.$$

5. ANALYSIS OF THE RESULTS AND CONCLUSION

As we have said, the absorption spectrum for free excitons has a δ -function-like form, which, when the interaction of the excitons with the low-frequency Bose-type excitations (phonons and magnons) is taken into account acquires a characteristic structure. At sufficiently low temperatures it consists of a main line and accompanying fine-structure lines corresponding to the simultaneous excitation of an exciton and one, two, etc. Bose excitations. The optical absorption of

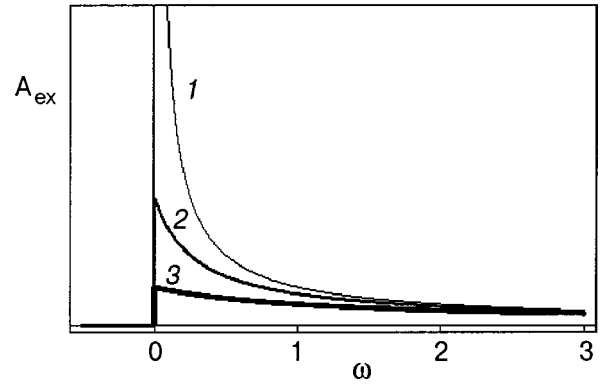


FIG. 1. Transformation of the excitonic spectrum $A_{\text{ex}}(\mathbf{Q}=0, \omega - \Delta\varepsilon)$ when only the static magnetic fluctuations are taken into account, for different $\xi_{\text{mag}}: \infty$ (1), $2a$ (2), and a (3); a is the lattice constant of the magnetic lattice, and the frequency ω is given in units of the width of the excitonic band, $W = 1/2m^*a^2$, and is measured from the bottom of this band. The value of the parameter α was assumed constant and equal to $\alpha(T_{\text{BKT}}) = 7/8$.

the α phase has just such a form throughout its entire existence region in temperature (see, e.g., Figs. 17.4–17.6 and 18.5–18.7 of Ref. 1).

The transition to the β phase from the α phase causes these lines to become so smeared that they lose all visible structure, transforming into broad asymmetric bands with a relatively abrupt long-wavelength wing and an extended short-wavelength wing (see Fig. 17.6 of Ref. 1).

A similar qualitative form is exhibited by the spectrum described by expression (42) (we note that for $\mathbf{Q}=0$ this expression simplifies substantially, since the hypergeometric function goes to 1), which is shown in Fig. 1. Indeed, even algebraic order is sufficient for the short-wavelength wing of the excitonic line to reach 2–3 widths of the excitonic band. In that case, however, the pronounced spectral feature reminiscent of a broadened asymmetric line is preserved. It vanishes completely in the case of finite $\xi_{\text{mag}}(T)$, when the spectrum acquires the form shown in Fig. 1 (curves 2 and 3), where no structure of any kind appears but the long-wavelength absorption edge remains abrupt. Approximately the same shape is observed for the IR spectrum of a crystal containing heavy impurities.⁴¹

This edge becomes smeared when the damping of the spin correlations with time is taken into account. Then (see Fig. 2) the shape of the band shape calculated numerically according to formula (46) practically coincides with the observed shapes of the one- and two-exciton absorption bands of $\beta\text{-O}_2$, where they all have a similar structure:¹ a relatively abrupt red wing and a rather long violet tail. Thus the dynamic spin fluctuations in a medium with correlational ordering indeed lead to the form of the excitonic absorption spectrum observed in the β phase of oxygen and can be considered responsible for the radical change in the absorption spectrum that occurs in this crystal at the $\alpha\beta$ transition.

Our results pertaining to the method of taking into account the absence of long-range spin order and its influence on the spectrum of quasiparticles might have a more general significance. One can in fact give examples for which the correlational ordering can be important. One such example is the recently discovered effect wherein behavior of this kind

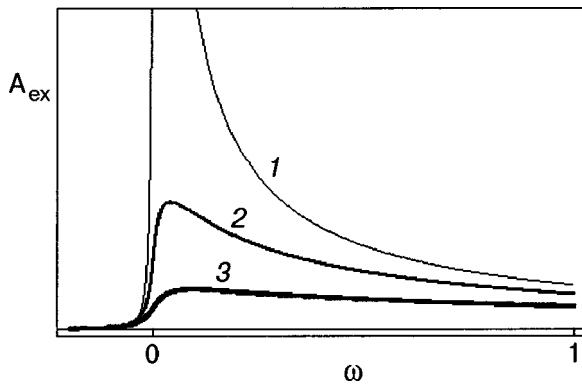


FIG. 2. Transformation of the excitonic spectrum $A_{\text{ex}}(\mathbf{Q}=0, \omega - \Delta \epsilon)$ with allowance for dynamic magnetic fluctuations; 1 — $\xi_{\text{mag}} = 10a$, $\gamma = 0.01W$; 2 — $\xi_{\text{mag}} = 2a$, $\gamma = 0.05W$; 3 — $\xi_{\text{mag}} = a$, $\gamma = 0.1W$. Here ω and α given in the same dimensionless units as in Fig. 1.

— the complete vanishing of structure — occurs in the optical spectrum of α -O₂ under the influence of external pressure.⁴² Without claiming to have reached a final conclusion, let us state the following conjecture. If the pressure is even slightly nonuniform and the temperature is finite, the effect of the pressure will not only be an inhomogeneous broadening of the spectral lines but also to a certain extent the “creation” of a medium which should be described by a suitable correlation length. In accordance with what we have said above, its influence should modify the spectrum.

A more convincing example is the dramatic change in the amplitude of the μ SR signal from electrons injected into the orientationally ordered α phase of solid N₂ in comparison with the same signal from electrons injected into the orientationally disordered cryocrystal N₂-Ar.⁴² Obviously the character (spin or orientational) of the subsystem on which the kinetic characteristics of the quasiparticle depend is not of fundamental importance, and a function of the type [(24) (or (31))] can describe the correlations of the orientations. Here the Anderson localization and, even more so, the self-trapping with the formation of a polaron, which was proposed in Ref. 43, do not seem to be necessary conditions for the observation of the change in μ SR signal and the corresponding change in the kinetic properties of the electron.

Finally, the same method can be used to calculate the Green function of the magnons (their spectral density) for systems of this kind in which, for some reason or other, the long-range ordering is suppressed. If the order itself (of a correlational or other nature) can be described by functions of the type (24) or (31), then in a medium corresponding to it one can scarcely talk of quasiparticles — magnons, excitons, electrons — in the usual meaning of this word. Quasiparticles will not exist once the parameter (27) is no longer equal to unity, and the quasiparticle properties will gradually be recovered as the temperature decreases, when $\alpha \rightarrow 1$. Interestingly, just such a recovery is observed in superconducting copper oxides, where the quasiparticle Fermi excitations begin to be observed only at temperatures substantially below the critical temperature; near the critical temperature and above it, no quasiparticles could be detected.

Here it is necessary to keep in mind that the correlational ordering in high- T_c superconductors pertains, on the one

hand, to the superconducting 2D condensate,⁴⁰ and, on the other hand, to the magnetic subsystem (the spins of the Cu²⁺ ions), which in the metallic phase do not have long-range order. A generalization of the approach developed above to the aforementioned case of magnetic superconducting systems with correlation lengths of different natures and, accordingly, different orderings, which obey conditions of the type (1), will be done separately.

We are grateful to V. P. Gusynin for numerous consultations about the method used in this study and to M. A. Ivanov for a discussion. V. M. L. thanks Prof. H.-J. Jodl and V. G. Storzhak for interest in this study and for encouragement and support. We would also like to thank the referee for extremely constructive criticism that led to improvements in the exposition of the results. This study was supported in part by the Swiss National Science Foundation (SCOPES Project 7UKPJ062150.00/1).

*E-mail: vloktev@bitp.kiev.ua

¹The same changes also occur in the libron spectrum.¹

²It describes the interaction of O₂ molecules only in their ground state, since $S=0$ in the lowest electronic excited states $^1\Delta_g$ and $^1\Sigma_g$ of oxygen.

³This, of course, is not referring to effects such as optical nutation in a strong external electromagnetic field.

⁴Staying within the framework of a Bose representation for the excitonic states, we do not include the mean-field term $\mathcal{H}_{\text{exc}}^{MF} = Js_z \sum_{\mathbf{n}_\alpha} \rho_{\alpha\beta} S_{\mathbf{n}_\alpha}^z \cos(\varphi_{\mathbf{n}_\alpha} - \varphi_{\mathbf{n}_\alpha + \rho_{\alpha\beta}})$ that follows from Eq. (9), which leads only to an exchange shift of the one-electron (or, equivalently, the excitonic) levels.

⁵We note that for $T \rightarrow 0$ expression (42) does not go over to a δ function, since the latter is a generalized function, and obtaining it requires the accurate use of the initial expressions (21) and (38).

¹ B. I. Verkin and A. F. Prikhot'ko (Eds.), *Cryocrystals* [in Russian], Naukova Dumka, Kiev (1983).

² I. N. Krupskii, A. I. Prokhvatilov, Yu. A. Freiman, and A. I. Érenburg, *Fiz. Nizk. Temp.* **5**, 271 (1979) [*Sov. J. Low Temp. Phys.* **5**, 130 (1979)].

³ A. S. Baryl'nik and A. I. Prokhvatilov, *Fiz. Nizk. Temp.* **20**, 912 (1994) [*Low Temp. Phys.* **20**, 716 (1994)].

⁴ R. A. Alikhanov, *JETP Lett.* **5**, 349 (1967).

⁵ V. V. Eremenko and Yu. G. Litvinenko, *Zh. Tekh. Fiz.* **52**, 539 (1967) [*Sic*].

⁶ A. F. Prikhot'ko and O. S. Pakhomova, *Ukr. Fiz. Zh.* **13**, 19 (1968).

⁷ J. E. Cahill and G. E. Leroi, *J. Chem. Phys.* **51**, 97 (1969).

⁸ A. S. Borovik-Romanov, M. P. Orlova, and P. G. Strelkov, *Dokl. Akad. Nauk SSSR* **99**, 699 (1954).

⁹ G. C. Defotis, *Phys. Rev. B* **23**, 4714 (1981).

¹⁰ M. F. Collins, *Proc. Phys. Soc. (London)* **89**, 415 (1966).

¹¹ P. W. Stephens, R. J. Birgeneau, C. F. Majkrzak, and G. Shirane, *Phys. Rev. B* **28**, 452 (1983).

¹² R. J. Meier and R. B. Helmholtz, *Phys. Rev. B* **29**, 1387 (1984).

¹³ V. M. Loktev, *Fiz. Nizk. Temp.* **5**, 295 (1979) [*Sov. J. Low Temp. Phys.* **5**, 142 (1979)].

¹⁴ V. A. Slyusarev, Yu. A. Freiman, and R. P. Yankelevich, *Fiz. Nizk. Temp.* **7**, 536 (1981) [*Sov. J. Low Temp. Phys.* **7**, 265 (1981)].

¹⁵ B. Kuchta, *Phys. Lett. A* **103**, 202 (1984).

¹⁶ R. J. Meier, *Phys. Lett. A* **107**, 275 (1985); *ibid.* **112**, 341 (1985).

¹⁷ E. Rastelli and A. Tassi, *J. Phys. C* **19**, L423 (1986).

¹⁸ M. A. Jansen, *Phys. Rev. B* **33**, 6352 (1986).

¹⁹ I. M. Vitebskii, V. M. Loktev, V. L. Sobolev, and A. A. Chabanov, *Fiz. Nizk. Temp.* **18**, 1044 (1992) [*Low Temp. Phys.* **18**, 733 (1992)]; *Fiz. Nizk. Temp.* **19**, 151 (1993) [*Low Temp. Phys.* **19**, 107 (1993)].

²⁰ I. M. Vitebskii and N. M. Lavrinenko, *Fiz. Nizk. Temp.* **19**, 535 (1993) [*Low Temp. Phys.* **19**, 380 (1993)].

²¹ R. S. Gekht, *Usp. Fiz. Nauk* **159**, 261 (1989) [*Sov. Phys. Usp.* **32**, 871 (1989)].

²² A. F. Prikhot'ko, M. Ruéman, and A. S. Fedoritenko, *Zh. Éksp. Teor. Fiz.* **5**, 712 (1935)].

²³ A. F. Prikhot'ko, *Zh. Éksp. Teor. Fiz.* **7**, 929 (1937)].

- ²⁴ A. F. Prikhot'ko, T. P. Ptukha, and L. I. Shanskiĭ, *Ukr. Fiz. Zh.* **12**, 1166 (1967); *Opt. Spektrosk.* **22**, 373 (1967).
- ²⁵ V. V. Eremenko, Yu. G. Litvinenko, and T. I. Garber, *Phys. Status Solidi* **30**, 49 (1968).
- ²⁶ Yu. G. Litvinenko, V. V. Eremenko, and T. I. Garber, *Ukr. Fiz. Zh.* **14**, 326 (1969).
- ²⁷ M. A. Krivoglaz and G. F. Levenson, *Fiz. Tverd. Tela (Leningrad)* **9**, 457 (1967) [*Phys. Solid State* **9**, 349 (1967)].
- ²⁸ Yu. B. Gaĭdideĭ and V. M. Loktev, *Solid State Commun.* **27**, 37 (1978).
- ²⁹ Yu. B. Gaĭdideĭ and V. M. Loktev, *Fiz. Nizk. Temp.* **7**, 1305 (1981) [*Sov. J. Low Temp. Phys.* **7**, 634 (1981)].
- ³⁰ V. V. Eremenko, *Introduction to the Optical Spectroscopy of Magnets* [in Russian], Naukova Dumka, Kiev (1975).
- ³¹ É. G. Petrov, *Theory of Magnetic Excitons* [in Russian], Naukova Dumka, Kiev (1976).
- ³² Yu. B. Gaĭdideĭ, V. M. Loktev, and A. F. Prikhot'ko, *Fiz. Nizk. Temp.* **3**, 549 (1977) [*Sov. J. Low Temp. Phys.* **3**, 263 (1977)].
- ³³ A. S. Davydov, *Theory of Molecular Excitons* [in Russian], Nauka, Moscow (1968).
- ³⁴ V. M. Loktev and V. S. Ostrovskii, *Fiz. Nizk. Temp.* **20**, 983 (1994) [*Low Temp. Phys.* **20**, 775 (1994)].
- ³⁵ P. Minnhagen, *Rev. Mod. Phys.* **59**, 1001 (1987).
- ³⁶ J. M. Kosterlitz, *J. Phys. C* **7**, 1046 (1974).
- ³⁷ V. M. Loktev, *Ukr. Fiz. Zh.* **24**, 1409 (1979).
- ³⁸ D. L. Huber, *Phys. Lett. A* **68**, 125 (1978).
- ³⁹ V. P. Gusynin, V. M. Loktev, R. M. Quick, and S. G. Sharapov, submitted to *Europhys. Lett.*
- ⁴⁰ V. P. Gusynin, V. M. Loktev, and S. G. Sharapov, *Zh. Éksp. Teor. Fiz.* **117**, 1143 (2000) [*JETP* **90**, 993 (2000)].
- ⁴¹ M. N. Botvinko and M. A. Ivanov, *Fiz. Tverd. Tela (Leningrad)* **22**, 2374 (1980) [*Sov. Phys. Solid State* **22**, 1381 (1980)].
- ⁴² H.-J. Jodl, *Abstracts of Third International Conference on Cryocrystals and Quantum Crystals*, Szklarska Poreba, Poland, July 28–August 4, 2000, p. 30.
- ⁴³ V. G. Storchak, D. G. Eschenko, J. H. Brewer, G. D. Morris, S. P. Cottrell, and S. F. J. Cox, *Phys. Rev. Lett.* **85**, 166 (2000).

Translated by Steve Torstveit

LATTICE DYNAMICS

Lattice constant and coefficient of linear thermal expansion of the silicon crystal. Influence of isotopic composition

A. P. Zhernov*

Institute of Superconductivity and Solid State Physics, Kurchatov Institute Russian Science Center, pl. Kurchatova 1, 123182 Moscow, Russia

(Submitted March 23, 2000; revised July 12, 2000)

Fiz. Nizk. Temp. **26**, 1226–1235 (December 2000)

The features of the temperature behavior of the lattice constant and the coefficient of thermal expansion of silicon crystals are analyzed in the bond-charge model. The coefficient of thermal expansion and the Grüneisen factor for the natural isotopic composition are described to reasonable quantitative accuracy. The influence of the isotopic composition on the value of the lattice constant is discussed in detail. © 2000 American Institute of Physics.
[S1063-777X(00)00812-4]

1. INTRODUCTION

Considerable attention is now being devoted to the study of chemically pure and structurally perfect semiconductor single crystals with different isotopic compositions. There have been many papers on the study of such semiconductors as diamond, germanium, and silicon. Highly isotopically enriched samples of ^{12}C , ^{70}Ge , ^{76}Ge , and ^{28}Si have been synthesized (see, e.g., Refs. 1–5).

As the isotopic composition of the components of the compounds is varied, effects which are linear in the mass difference of the isotopes appear, and there are also effects proportional to the parameter of the mean-square deviation of the atomic masses (in other words, there are effects of first and second orders). The first-order effects can have an appreciable influence on the static and thermodynamic properties, and the effects of both orders are manifested importantly in the features of the behavior of the kinetic parameters and optical spectra (see, e.g., Refs. 6–8).

The influence of the isotopic composition on the lattice constant a and coefficient of linear thermal expansion α has been studied in a number of papers. Experimentally the dependence of the lattice parameter a on the composition was examined for diamond crystals in Ref. 1. For germanium the temperature behavior of the lattice constant a was studied in Ref. 9, and the coefficient of thermal expansion was investigated in Ref. 10. In the case of silicon the corresponding measurements have not been made. The dependence of the parameter a on the composition and temperature for C, Ge, and Si was analyzed in Ref. 11 using the density functional method, and in Ref. 12 the coefficient $\alpha(T)$ was calculated for the natural isotopic composition. The agreement with experiment was only qualitative. Previously we have investigated the behavior of the linear coefficient of thermal expansion of the Ge lattice with the use of the bond-charge model.¹³

Studies of the influence of the isotopic composition on the thermal conductivity of germanium and silicon have also been carried out.^{3–5,14,15}

In the present paper we discuss the features of the change in a and α over a wide range of temperatures for crystals of silicon, the base material for modern electronics, and examine the role of the isotopic composition.

It should be noted that the temperature dependence of the lattice parameters in silicon is nonstandard. First, the values of the partial Grüneisen factors $\gamma(l)$ characterizing the dependence of the phonon mode frequencies $\omega(l)$ (the index l labels the phonon modes) on the volume are perceptibly different at low and high frequencies, and at high temperatures the low-frequency values are noticeably different from the mean values. Because of the features of the dynamic interatomic interaction, the factor $\gamma(l)$ for transverse acoustical modes is negative in sign (see, e.g., the monograph¹⁶ and the review¹⁷). Second, the characteristic frequencies for the transverse acoustical and longitudinal optical modes are substantially different. On the temperature scale their units correspond to values close to 200 and 700 K. We note that the Debye temperature T_D equals 625 K. The maximum frequency of the spectrum is 743 K (see, e.g., the experimental papers^{18,19}).

Analysis of the behavior of the parameters $a(T)$ and $\alpha(T)$ for Si have been carried out in the quasiharmonic Grüneisen–Mie approximation, in which one considers the dependence of the lattice parameter a on the temperature T . Recall that in a harmonic crystal lattice the phonon mode frequencies $\omega(l)$ are determined for a fixed atomic configuration and do not depend on temperature. In reality, because of anharmonicity, the interatomic interaction energy and the related dynamic force parameters and frequencies $\omega(l)$ actually do depend on the volume and on T . In a quasiharmonic approach the potential energy is expanded to second order in the dynamic atomic displacements, but some parts of the anharmonic effects are taken into account through assumptions about the dependence of a on T and the dependence of $\omega(l)$ on $a(T)$.

Since for silicon the mean masses of systems with different isotopic compositions deviates only slightly from the

mass corresponding to the natural composition, in determining the behavior of $a(T)$ and $\alpha(T)$ we consider only effects which are linear in the mass difference of the isotopes. The theory contains the mean values of the atomic masses, M_c , the values of which are varied. In other words, the problem is treated in the virtual crystal approximation.

The case of natural isotopic composition corresponds to an effective mean mass of 28.0855. Masses of 28, 29, and 30 correspond to maximally enriched samples. Here, in relation to the crystal with natural composition, the samples of ^{28}Si and the samples of ^{29}Si and ^{30}Si can be regarded as consisting of “light” and “heavy” isotopes.

Concrete calculations were carried out using the microscopic bond-charge model. This model, which was developed in Refs. 20, is based on the premise that the electron charge which is concentrated at the center of the chemical bond can be treated as a dynamic quantity influencing the interatomic bond. Essentially, the effective dynamic couplings that arise between nearest-neighbor charges on the bonds due to the motion of the atoms in the transverse direction is stronger than the dynamic coupling between an atom and its neighboring charge on the bonds. The application of this model to silicon (germanium) is motivated by the fact that it can describe the large flat part of the dispersion curve for transverse acoustical phonons (and the rest of the spectrum as well).

In Ref. 21 the bond-charge model was generalized to the case when the crystal is strained by external stresses. It was found that in the strained quasiharmonic lattice (with displaced atoms) the force parameters appearing in the dynamic matrix are altered. The case of hydrostatic pressure was considered. Experimental data on the values of the partial Grüneisen factors at the high-symmetry points Γ , X , and L for transverse and longitudinal acoustical and optical modes (they were found from optical experiments) were used to refine the parameters of the model. The values of $\gamma(l)$ were calculated for the symmetric directions.

In the present paper the results obtained in Ref. 21 are used to determine the frequencies $\omega(l)$ and the partial factors $\gamma(l)$. To the author’s knowledge, this is the first time that the behavior of the lattice parameter $a(T)$ and of the coefficient of thermal expansion α has been studied for Si crystals with different isotopic compositions.

In Sec. 2 the basic relations for $a(T)$ and $\alpha(T)$ are set forth for crystals whose unit cell contains atoms of a single element. In Sec. 3 the universal dependences of the parameters $a(T)$ and $\alpha(T)$ on M_c are discussed. In Sec. 4 the case of silicon is analyzed in the framework of the bond-charge model. Attention is devoted primarily to a discussion of the coefficient of thermal expansion and the Grüneisen factor, since for these quantities there are experimental data available for the natural isotopic composition.^{22,23} Then the behavior of the lattice parameter is discussed for single crystals of the natural and enriched compositions.

2. UNIT CELL VOLUME, THERMAL EXPANSION, AND GRÜNEISEN FACTOR IN THE LINEAR APPROXIMATION IN THE ISOTOPIC MASS DIFFERENCE. BASIC RELATIONS

Let us consider the equation of state relating the state variables: the temperature T , volume V , and pressure P . By definition, $P = -(\partial F/\partial V)_T$, where F is the free energy.

The free energy of the crystal is the sum of the energy E_s of the static lattice, in which the atoms occupy equilibrium positions, and the vibrational energy F_v of the atoms:

$$F(V, T) = E_s(V, T) + F_v(V, T). \tag{1}$$

The vibrational energy F_v in the quasiharmonic approximation is defined as (see, e.g., Refs. 6 and 7)

$$F_v = \sum_l \frac{\hbar \omega(l)}{2} + k_B T \sum_l \ln \left[1 - \exp \left(- \frac{\hbar \omega(l)}{k_B T} \right) \right] \\ = k_B T \sum_l \ln \left[2 \sinh \left(\frac{\hbar \omega(l)}{2 k_B T} \right) \right]. \tag{2}$$

In Eq. (2) the index l labels the vibrational modes: $l = \mathbf{f}, j$, where \mathbf{f} is the quasimomentum and j is the polarization of the phonon mode; k_B and \hbar are Boltzmann’s and Planck’s constants. The frequencies $\omega(l)$ in Eq. (2) depend on the volume, on the temperature T , and on the masses of the atoms. For crystals whose unit cell contains atoms of just one element with any isotopic composition, the following relation holds for a specific mode l in the linear approximation in the isotopic mass difference:

$$\frac{d \ln \omega_c^2(l)}{d \ln M_c} = -1 \tag{3}$$

(see Appendix), where $M_c = \sum_i c_i M_i$ is the value of the mean mass of an atom, and c_i and M_i are the concentration and mass of isotope i .

When the crystal is strained, the atoms occupy new equilibrium positions. This changes the energy E_s and frequencies $\omega(l)$. In this paper it is assumed that the change in volume as a result of the strain is isotropic. For a crystal with cubic symmetry, we can write the equation of state, with allowance for (1) and (2), in the form

$$P + \frac{dE_s}{dV} = \frac{1}{V} \sum_l \gamma(l) \varepsilon(l), \tag{4}$$

where $\gamma(l)$ is the partial Grüneisen factor for the l th vibrational mode. This factor takes into account that the frequencies of the different modes depend on the volume in different ways. The factor $\varepsilon(l)$ denotes the contribution of each mode to the thermal energy. Thus

$$\gamma(l) = - \frac{\partial \omega(l)/\partial \Omega}{\omega(l)/\Omega}, \quad \varepsilon(l) = \hbar \omega(l) \left(n(l) + \frac{1}{2} \right). \tag{5}$$

Here $n(l)$ is the Bose–Einstein factor. We note that the quantity $\sum_l \gamma(l) \varepsilon(l)$ is the pressure of noninteracting phonons p_{ph} .

If it is assumed that the partial Grüneisen factors have nearly the same values for all the modes, then in place of (4) we can write the Grüneisen–Mie equation of state:²⁴

$$P + \frac{dE_s}{dV} = \gamma \frac{E_v}{V}, \quad E_v = \sum_l \varepsilon_l. \tag{6}$$

In the case of normal pressure we can set $P = 0$.

Let us assume that we know the parameters of the crystal at the temperature $T_0 = 0$. By definition, $V(T) = N \Omega(T)$, where Ω is the volume of the unit cell of the lattice. Let Ω_0 be the volume of the cell at the temperature $T_0 = 0$. We ex-

pend the terms on the left- and right-hand sides of Eq. (6) in a series in powers of $\Omega - \Omega_0$. To a first approximation we keep the linear term on the left and ignore the volume dependence of $\gamma(l)$ and $\omega(l)$ on the right. As a result, we find that to a first approximation the change in volume of the cell $\Omega - \Omega_0$ as a function of temperature is given by an expression of the form

$$\frac{\Delta\Omega}{\Omega_0} = \frac{\Omega - \Omega_0}{\Omega_0} = \frac{1}{3B_0\Omega_0} \sum_l \gamma(l)\varepsilon(l), \quad \Omega_0 = \Omega(T_0), \quad (7)$$

where $B_0 = \Omega_0(\partial^2 E_s / \partial \Omega^2)_{\Omega_0}$ is the bulk modulus of compression at $T = T_0$.

The volume difference $\Delta\Omega$ can be expressed in terms of the difference $\Delta a = a - a_0$, where a and a_0 are the unit cell parameters at $T \neq T_0$ (with allowance for the distribution of the atomic vibrations) and $T = T_0$ (without allowance for the zero-point atomic vibrations). According to Eq. (7),

$$\tilde{a}_s = \frac{\Delta a}{a_0} = \frac{\Delta\Omega}{3\Omega_0} = \frac{1}{3B_0\Omega_0} \sum_l \gamma(l)\varepsilon(l). \quad (8)$$

When the isotopic composition of the lattice is changed, the mean mass, generally speaking, varies in a continuous manner. Therefore we define a differential parameter of the form

$$f_a = \left(\frac{\partial \ln a}{\partial \ln M} \right)_{M=M_n} = - \frac{1}{6\Omega_0 B_0} \sum_l \gamma(l) \left[\varepsilon(l) - T \frac{\partial \varepsilon(l)}{\partial T} \right], \quad (9)$$

where M_n is the mass in the case of the natural isotopic composition. In addition, let

$$\varepsilon(l) - T \frac{\partial \varepsilon(l)}{\partial T} = \frac{1}{2} \hbar \omega(l) Z(x'(l)), \quad (10)$$

$$Z(x') = \left[\cosh x' - \frac{x'}{\sinh^2 x'} \right], \quad x'(l) = \frac{\hbar \omega(l)}{2k_B T}.$$

We go over to a description in terms of the coefficient of thermal expansion $\alpha(T)$ for the cubic crystal lattice. Using Eq. (8), we obtain (see, e.g., Refs. 6 and 13)

$$\alpha(T) = \frac{\partial}{\partial T} \frac{\Delta a}{a_0} = \frac{1}{B_0} \frac{\partial p_{ph}}{\partial T} = \frac{1}{3\Omega_0 B_0} \sum_l \gamma(l) C_l(T), \quad (11)$$

where $C_l(T)$ is the contribution to the heat capacity from the l th vibrational mode:

$$C_l(T) = \frac{\partial \varepsilon(l)}{\partial T} = k_B x^2(l) n(l) [n(l) + 1],$$

$$x(l) = \frac{\hbar \omega(l)}{k_B T}. \quad (12)$$

Expressions (7)–(11) are given in the first approximation of the theory. We note that in the next approximation it is necessary to take into account the change in volume and bulk modulus due to the thermal expansion and also the anharmonic contributions to the phonon pressure and the corresponding renormalization of the bulk modulus. It is usually

assumed that the renormalization of the bulk modulus due to the dependence of Ω on T can be substantial. The question of the anharmonicity of the phonon modes requires a special analysis.

Together with $\alpha(T)$, we consider the integral Grüneisen factor $\gamma(T)$. By definition it is given by¹⁶

$$\gamma(T) = \frac{\Omega \alpha B_s}{C_p} = \frac{\Omega \alpha B_T}{C_v} = \frac{\Omega}{C_v} \left(\frac{\partial p_{ph}}{\partial T} \right)_{\Omega}. \quad (13)$$

To a first approximation we get

$$\gamma(T) = \sum_l \gamma(l) C_l(T) / \sum_l C_l(T). \quad (14)$$

We note that the function $\gamma(T)$ is the weighted mean of the corresponding contributions of the individual modes.

Let us consider two crystals with mean masses M_c and $M_{c1} = M_c + \Delta M$. The relative change in the coefficient of thermal expansion, $\Delta \alpha_c(T) = \alpha(M_{c1}) - \alpha(M_c)$, in the case $|\Delta M| \ll M_c$, can be written, according to Eqs. (11) and (14), as

$$\Delta \alpha_c \approx \alpha^{(1)}(M_c) + \alpha^{(2)}(M_c), \quad (15)$$

where

$$\alpha^{(1)}(M_c) = \alpha(M_c) \left(\frac{\Delta \gamma_c}{\gamma(M_c)} + \frac{\Delta C_c}{C_L(M_c)} \right), \quad (16)$$

$$\Delta \gamma_c(T) = \gamma(M_{c1}) - \gamma(M_c),$$

$$\Delta C_c(T) = C_L(M_{c1}) - C_L(M_c),$$

and

$$\alpha^{(2)}(M_c) = \alpha(M_c) \left(\frac{R(M_c)}{R(M_{c1})} - 1 \right), \quad R = \Omega_0 B_0. \quad (17)$$

Here

$$\alpha^{(2)}(M_c) \sim -\alpha(M_c) \rho \frac{\Delta M}{M_c}, \quad \rho = \left(\frac{\sum_l \gamma(l) \omega(l)}{2B_0 \Omega_0} \right)_{M=M_c}. \quad (18)$$

Let us briefly discuss relations (15)–(18). First, the character of the dependence of $\Delta \alpha_c^{(1)}$ on T is governed by the difference of the phonon spectra of the crystals with masses M_c and M_{c1} . If the partial Grüneisen factors $\gamma(l)$ on the whole do not differ appreciably from some average values, then the first term in parentheses in Eq. (16) can be neglected. In the general case both terms, $\Delta \gamma_c$ and ΔC_c , are important. Second, for silicon the factor $\rho \approx 2 \times 10^{-3}$, and the parameter $\Delta M/M_c$ can amount to a few percent. Thus in relative units the change in the volume of the unit cell at $T = 0$ due to variation of the isotopic composition amounts to $\sim 10^{-5}$. Concrete estimates show that in the case of silicon the term $\alpha^{(2)}$ can be neglected in comparison with $\alpha^{(1)}$.

We note that in the case of high temperatures $T < T_D/2$ (T_D is the Debye temperature)

$$\varepsilon(l) \approx k_B T \left[1 + \frac{1}{12} x^2(l) - \frac{1}{7200} x^4(l) \right], \quad (19)$$

$$Z(x'(l)) \approx \frac{1}{3}x(l) \left[1 - \frac{1}{30}x^2(l) + \frac{1}{840}x^4(l) \right], \quad (20)$$

$$C_l(T) \approx k_B \left[1 - \frac{1}{12}x^2(l) + \frac{1}{240}x^4(l) \right]. \quad (21)$$

We substitute (19)–(21) into the expressions for \tilde{a}_s (8), f_a (9), and α (11). As a result, we find that for $T > T_D/2$ the lattice parameters a and f_a and the parameters α and γ should be extremely weakly dependent on the isotopic composition.

We call attention to the fact that in the classical limit for $T > T_D$ the sum partition function can be replaced by an integral,

$$Z = \int \exp\left(-\frac{H(\Omega, p_1, \dots, u_N)}{k_B T}\right) dp_1 \dots du_N, \quad (22)$$

where the Hamiltonian function H of the system depends on the atomic momenta and displacements. The factor Z can be written in the form of a product of two integrals I_1 and I_2 . The first of them is due solely to the distribution over the atomic momentum components (the expression for which contains the kinetic energies of the isotopes and their masses) and is easily evaluated: $I_1 = (2\pi M_c k_B T)^{N/2}$. Importantly, I_1 is independent of the volume. The second integral, I_2 , is determined by the form of the potential energy of the dynamic interatomic interaction, i.e., the force parameters. Since the force parameters depend on the values of the atomic coordinates (and interatomic distances), the integral I_2 varies with the volume. However I_2 does not depend on M_c . By definition

$$F_v = -T \ln Z = -T(\ln I_1 + \ln I_2). \quad (23)$$

Consequently, the derivative $(\partial F_v / \partial \Omega)_{\Omega_0}$ is also independent of M_c . Thus in the case of classical statistics the values of the lattice constant and coefficient of thermal expansion are insensitive to the isotopic composition. It can therefore be asserted that the change in $a(T)$ and $\alpha(T)$ on variation of the isotopic composition is a macroscopic quantum effect.

3. UNIVERSAL RELATIONS FOR THE ISOTOPIC DEPENDENCE OF THE LATTICE PARAMETERS

Let us establish how the characteristics of the lattice of a virtual crystal whose unit cell contains atoms of only one element depend on the isotopic composition.

We label the parameters for a particular isotopic composition by the subscript c_0 . For an arbitrary isotopic composition we use the subscript c . We consider the expression (7) for the change in volume as a function of T . Differentiating $\gamma(T)$ with respect to M_c and using (3), we can see that $\gamma(l)$ is independent of M_c . The following quantity for $T < T_D$ does depend on the mass of the crystal, through the dependence of $\omega(l)$:

$$E_c(l, T) = \omega_c(l) \left[n \left(\frac{\hbar \omega_c(l)}{k_B T} \right) + \frac{1}{2} \right]. \quad (24)$$

According to Eq. (3), $\omega_c(l) \sim M_c^{-1/2}$. Hence

$$E_c(l, T) = \sqrt{M_{c_0}/M_c} E_{c_0}(l, T'), \quad T' = T \sqrt{M_c/M_{c_0}}. \quad (25)$$

By virtue of (25) we obtain for the change in volume (7) a universal relation of the form

$$\Delta \Omega_c(T) = \sqrt{M_{c_0}/M_c} \Delta \Omega_{c_0}(T'). \quad (26)$$

Similarly,

$$\alpha_c(T) = \alpha_{c_0}(T'). \quad (27)$$

We note that a relation analogous to (26) holds for the lattice parameter \tilde{a}_s (8).

Relations of a universal type are conveniently used in an analysis of the isotopic composition. Specifically, if the data for the natural composition are known, then one can simply determine theoretically the values of the parameters for enriched compositions and compare the values obtained with the corresponding experimental results.

4. COEFFICIENT OF THERMAL EXPANSION, GRÜNEISEN FACTOR, AND LATTICE PARAMETER FOR SINGLE-CRYSTAL SILICON. THE RESULTS OF NUMERICAL CALCULATIONS FOR THE NATURAL AND MAXIMALLY ENRICHED COMPOSITIONS

Using the results obtained in the previous Section, we now investigate the behavior of the lattice characteristics $\tilde{a}_s(T)$ (8) and f_a (9) and of the coefficients $\alpha(T)$ (11) and $\gamma(T)$ (14) for silicon single crystals. We consider the case of natural composition, with three types of isotopes with a mean mass $M_n = 28.0855$, and the maximally enriched compositions with masses of 28, 29, and 30.

Specific calculations were carried out in the framework of the microscopic theory — the bond-charge model.²¹ We note that the values of the frequencies $\omega(l)$ calculated in the framework of the bond-charge model²¹ and the Born–Karman theory^{25,26} are practically coincident over the entire Brillouin zone. The following values were used for the parameters appearing in the theory: elastic constant $a_0 = 5.4310 \text{ \AA}$, and bulk modulus $B_0 = 0.998 \times 10^{12} \text{ dyn/cm}^2$.

The results of the calculations are presented in Figs. 1–5.

Let us consider the theoretical curves and experimental data for the temperature dependence of the integral Grüneisen parameter $\gamma(T)$ (14) and coefficient of linear thermal expansion $\alpha(T)$ (11) for silicon single crystals of natural composition. They are presented in Figs. 1 and 2, respectively. A comparison of the calculated and experimental^{22,23} data for $\gamma(T)$ and $\alpha(T)$ shows that the microscopic theory is in reasonable quantitative agreement with experiment over a wide range of temperatures.

We note that the dynamic properties of silicon and germanium are very similar. An analysis of $\gamma(T)$ for Ge is given in Ref. 13. We call attention to the fact that the dependence of the coefficient of thermal expansion α on T is in many cases dictated by the temperature behavior of the lattice heat capacity C_L . This is explained by the fact that the partial Grüneisen factors $\gamma(l)$ characterizing the volume dependence of $\omega(l)$, as a rule, differ only slightly from some average values. For silicon (and germanium) crystals, however, the values of $\gamma(l)$ at low and high frequencies are substantially different. As a result, the behavior of $\alpha(T)$ for Si is largely determined by the integral Grüneisen factor $\gamma(T)$ and not by the heat capacity C_L .

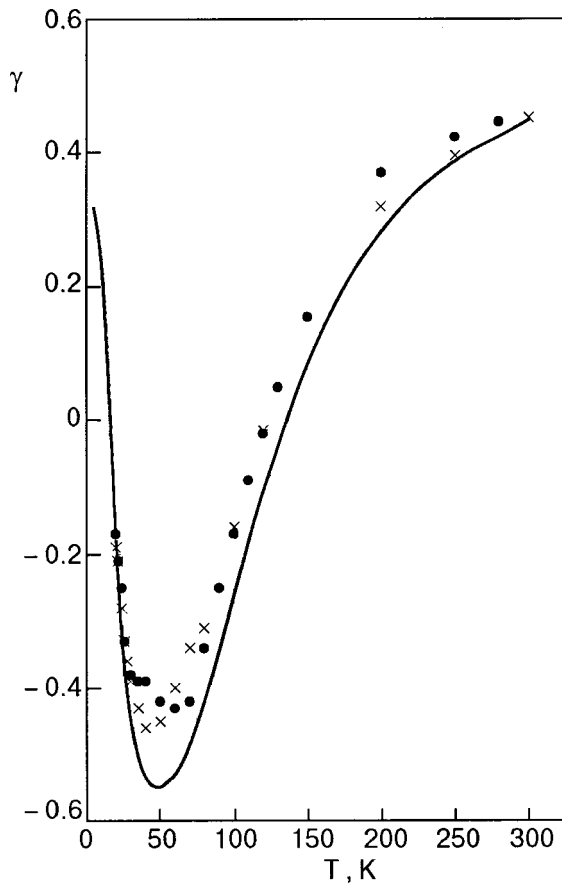


FIG. 1. Temperature dependence of the integral Grüneisen factor γ for silicon in the case of the natural isotopic composition: ● — experimental results obtained in Ref. 22; × — data of Ref. 23.

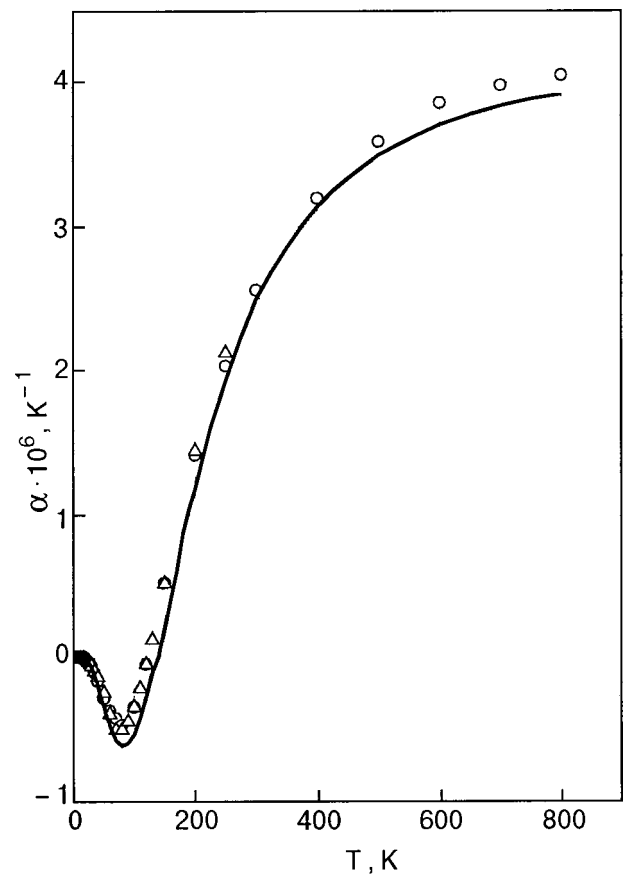


FIG. 2. Temperature dependence of the coefficient of linear thermal expansion α for $M_n=28.0855$; ▲ — results taken from Ref. 22; ○ — data of Ref. 23.

For germanium,¹³ unlike the case of silicon, the agreement with experiment for γ and α is only qualitative. It may be that the experimental values of the partial factors $\gamma(l)$ that were used in Ref. 21 are in need of refinement.

Figure 3 shows the results of calculations of the parameter $\tilde{a}_s(T)$ (8) in the case of the natural composition. Also plotted are the quantities

$$\tilde{a}_j(T) = \frac{4}{3B_0 a_0^3} \sum_f \gamma(\mathbf{f}, j) \varepsilon(\mathbf{f}, j). \quad (28)$$

The partial factors $\tilde{a}_j(T)$ (28) were determined for the transverse (t) and longitudinal (l) acoustical and the optical (o) branches. For the longitudinal acoustical and for the optical branches the factors \tilde{a}_j are positive in sign. For the transverse acoustical t branches the sign of \tilde{a}_t is negative (the negative sign of \tilde{a}_t is explained by the fact that as the distance between atoms decreases, the forces of attraction governing the corresponding transverse modes increase more rapidly than the forces of repulsion). In absolute value \tilde{a}_o is larger than \tilde{a}_t . The contribution of the partial factor \tilde{a}_0 for the optical branches is the determining factor. We emphasize that because the partial Grüneisen factors alternate in sign and because of the features of the phonon spectrum in the temperature interval $T=4.2-300$ K, the lattice constant de-

pends weakly on temperature. At $T=140$ K \tilde{a}_s passes through a minimum. For $T > T_D/2$ the factor $\tilde{a}_s(T)$ varies linearly with temperature.

Let us give the values of \tilde{a}_s at four temperatures, $T = 4.2, 140, 300,$ and 800 K, where the respective values are $\tilde{a}_s \times 10^2 = 0.1721, 0.1695, 0.1894,$ and 0.3649 . Consequently, \tilde{a}_s is larger at 800 K than at 4.2 K by approximately 0.002.

The results of the calculations for the differential factor $f_a = (\partial \ln a(T) / \partial \ln M)_{M_n}$ (9) are presented in Fig. 4. In the entire interval this quantity is mainly determined by the contribution for the optical modes. The corresponding contributions from the longitudinal and transverse acoustical modes are an order of magnitude smaller and to a considerable degree cancel each other out. The presence of a contribution from the transverse modes leads to a nonmonotonic variation of f_a with T . At $T \approx 80$ K the factor f_a passes through a minimum, and then in the classical temperature limit, as we have said, $f_a \rightarrow 0$. According to the calculations, f_a falls off in absolute value by approximately a factor of four as the temperature increases in the interval 0–800 K. The finite values at high T are due to the existence of high-frequency modes in the phonon spectrum of silicon. For $T > T_D/2$ the factor f_a varies as T^{-1} .

Let us give the values of f_a at four temperatures, $T = 4.2, 80, 300,$ and 800 K; the respective values are $f_a \times 10^3 = -0.8703, -0.8877, -0.5834,$ and -0.2554 .

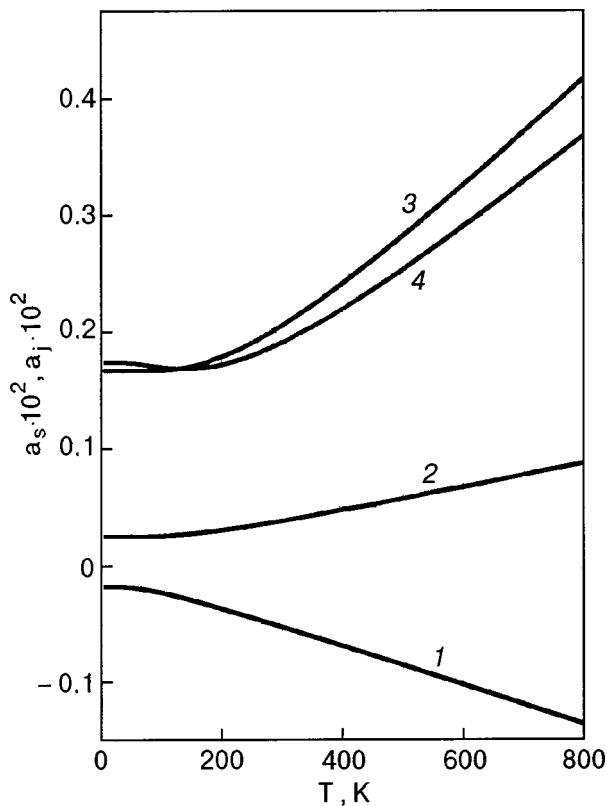


FIG. 3. Plots of $\tilde{a}_s(T)$ and $\tilde{a}_j(T)$ for the natural composition; the latter describes the partial contributions corresponding to the transverse (1) and longitudinal (2) acoustical modes and the optical modes (3). Curve 4 is the total factor \tilde{a}_s .

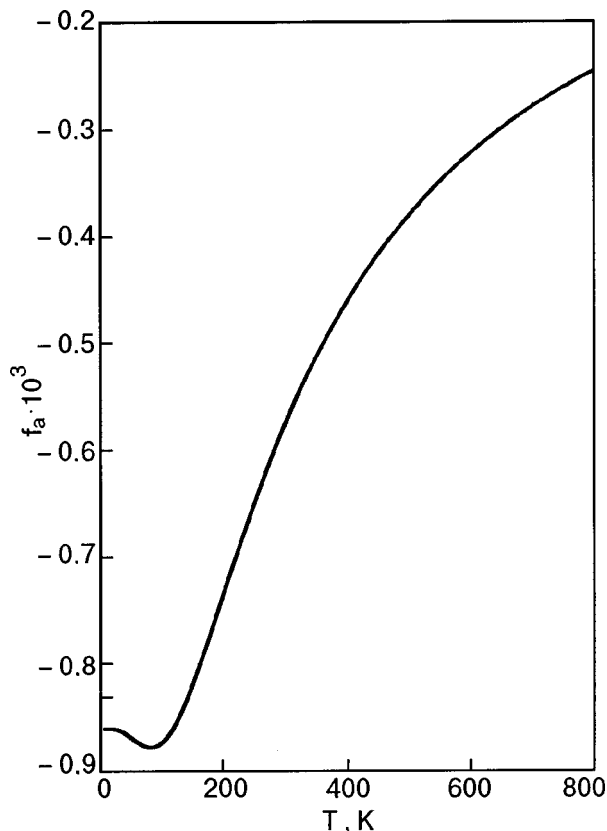


FIG. 4. Temperature dependence of f_a .

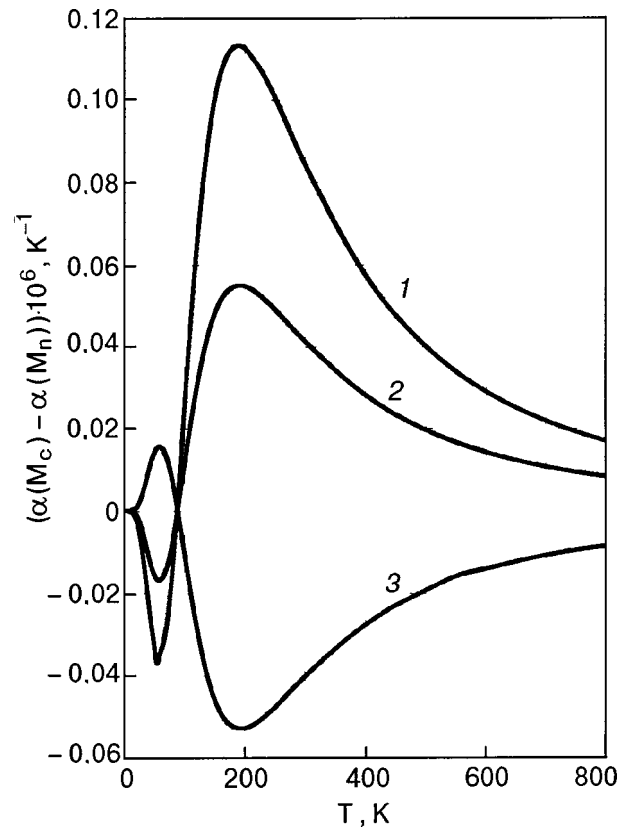


FIG. 5. Temperature dependence of $\alpha(M_c) - \alpha(M_n)$ for the cases of heavy and light isotopes: $M_c = 30$ (1), 29 (2), 28 (3). For the light isotopes the values of $\Delta\alpha_c$ are enlarged by a factor of 10 in comparison with those for the heavy isotopes.

The variations of the lattice constant with isotopic composition are described by the relation

$$a_c(T) - a_n(T) = \frac{M_c - M_n}{M_n} f_a(T) a_n(T). \quad (29)$$

From this relation we find that at $T = 300$ K, in going from the natural composition to the maximally enriched ^{28}Si the lattice constant increases by $\approx 2 \times 10^{-6} a_0$. At the same time, in going from ^{28}Si to ^{30}Si the lattice constant decreases by $3.8 \times 10^{-5} a_0$. If the temperature is comparatively low, $T \approx 0 - 100$ K, then the corresponding changes in the lattice parameter are one-and-a-half times larger.

We note that, according to Ref. 11, for silicon at $T = 298$ K the factor $f_a = -0.533 \times 10^{-3}$. This value is close to that obtained by us. For diamond the experimental value¹ is $f_a = -1.826 \times 10^{-3}$, i.e., it is of the same order of magnitude as for Si. However, in the case of diamond the phonon spectrum does not contain anomalous transverse acoustical modes, and, furthermore, $T_D = 1860$ K. For this reason the factor f_a for C also turns out to be considerably larger than for Si at the same temperature 298 K.

Figure 5 shows curves characterizing the scale of the isotope effects for $\alpha(T)$ in absolute units over a wide temperature interval. First, relation (11) was used to calculate the values of $\alpha(T)$ for crystals with the natural isotopic composition. Then the universal relation (27) was used to calculate the corresponding values for the maximally enriched crystals. The curves represent plots of the quantity $\Delta\alpha_c = \alpha(M_c) - \alpha(M_n)$ versus T , where $M_n = 28.0855$ and M_c

=28, 29, and 30. We recall that in relation to the crystal with the natural isotopic composition, the ^{28}Si and the $^{29,30}\text{Si}$ samples can be regarded as consisting of “light” and “heavy” isotopes.

The values corresponding to the light and heavy isotopes have different signs. The curves are nonmonotonic and have two extrema at $T_{m1} \approx 58$ K and $T_{m2} \approx 190$ K. In the high-temperature region under consideration the isotope effect remains finite because the optical modes are still not completely “frozen out.”

The behavior of the curves is described by formula (16). We note that the values of $\Delta C_c / C_L(M_c)$ have the same sign throughout this temperature interval: negative for the light isotope and positive for the heavy. The second term, $\Delta \gamma_c / \gamma(M_c)$ changes sign at temperatures $T_1 \approx 65$ K and $T_2 \approx 120$ K. For $T \leq T_1$ and for $T > T_2$ the two terms have the same sign and nearly the same order of magnitude. In the interval $T_1 < T < T_2$, on the contrary, the terms in (16) are of different signs.

In view of what we have said, let us consider the extrema on the $\Delta \alpha_c(T)$ curves. At a temperature $T_{m2} \approx 190$ K the main contribution to $\Delta \alpha_c$ is from optical modes. In this case there is a mutual enhancement of the renormalizations due to the changes in the mean mass in the integral Grüneisen parameter (here the contributions of the longitudinal and transverse optical modes are of the same sign) and in the lattice heat capacity.

At a temperature $T_{m1} \approx 58$ K the main contribution to $\Delta \alpha$ is due to the acoustical modes. The contributions to γ from the longitudinal and transverse acoustical modes partially compensate each other. Near T_{m1} the terms $\Delta C_c / C_L(M_c)$ and $\Delta \gamma_c / \gamma(M_c)$ are again of the same sign. However, in comparison with the previous case, the role of the term $\Delta \gamma_c / \gamma(M_c)$ is less important (because of the partial compensation of the contributions of the longitudinal and transverse acoustical branches).

We note that the values of the extrema differ strongly, since $\Delta \alpha_c$ is proportional to α_c . The value of α_c increases with increasing temperature, and the ratio $\alpha_c(T_{m2}) / \alpha_c(T_{m1})$ is close to three.

For semiconductor crystals with two chemically different atoms in the unit cell and with anomalous behavior of the Grüneisen parameter (i.e., like that in silicon) one can in principle determine experimentally the partial contributions to $\Delta \alpha_c$ of the acoustical and optical modes. For this it is necessary that the masses of the atoms of the components be substantially different. Then as the isotopic composition of the atoms of the compound within each sublattice is varied in the given situation there will be an appreciable change in either the acoustical or optical part of the phonon spectrum. For example, for the CsCl crystal, which has the zinc blende structure and anomalous behavior of the thermal expansion, it is predominantly the cesium atoms that vibrate in the acoustical part of the spectrum. As a result, changing the isotopic composition of the cesium will primarily affect the low-temperature part of the $\Delta \alpha_c(T)$ curve.

5. CONCLUSION

We have analyzed the features of the temperature dependence of the lattice constant a , coefficient of linear thermal

expansion α , and integral Grüneisen parameter γ for single crystals of silicon in the quasiharmonic approximation on the basis of the microscopic bond-charge model.^{20,21} We have shown that the experimental data for $\alpha(T)$ and $\gamma(T)$ can be described to reasonable accuracy in the framework of the bond-charge model.²¹ We have determined concrete values for $a(T)$. In the linear approximation in the isotopic mass difference we have considered the influence of the isotopic composition on the lattice constant $a(T)$. We have found values of the parameter $(\partial \ln a(T) / \partial \ln M)_{M_n}$. We have studied the changes in the factor $\alpha(T)$ upon variation of the isotopic composition. We have compared the corresponding values for crystals of the highly enriched and natural isotopic compositions.

The author is grateful to S. M. Stishov for helpful advice and to D. A. Zhernov and A. V. Inyushkin for assistance in this study. Valuable and constructive comments from the referee are also gratefully acknowledged.

6. APPENDIX

Consider two crystals having different isotopic compositions. We denote these as c and $c1$. Let

$$|M_c - M_{c1}| / M_c = |\Delta M| / M_c \ll 1. \quad (\text{A1})$$

We shall assume that the eigenfrequencies $\omega_c(l)$ and the orthonormalized polarization vectors $\mathbf{e}^c(k|l)$ (k labels the atoms in the unit cell) are known for a virtual monatomic crystal of mass M_c . We are to determine the isotope shift of the frequencies on going over to the composition $c1$.

We note that in an approximation linear in the mass difference of the isotopes, generally speaking, the local symmetry properties are not altered and the degeneracy is not lifted. In reality, even in the linear approximation in ΔM a static displacement field arises around the isotopes,^{27,28} but in standard crystals (in distinction to quantum crystals) these displacements are proportional to an additional small parameter $\langle u^2 \rangle / a^2$ ($\langle u^2 \rangle$ is the mean square value of the dynamic atomic displacements) and can be neglected in the problem under consideration. Thus in the framework of perturbation theory one is actually considering a nondegenerate case.

It is known that calculation of the eigenvalues to a definite order of smallness relative to the perturbation requires knowledge of the eigenfunctions to the next lower order. The change in the eigenvalues (square of the frequency) upon a variation of the isotopic composition is to a first approximation equal to the corresponding diagonal element of the energy of the perturbation with respect to the unperturbed states:

$$\left(\frac{\Delta \omega^2(l)}{\Delta M} \right)_c = \sum_{k,\alpha} \sum_{k',\alpha'} e_{\alpha}^{c*}(k|l) \times \left[\frac{\Delta \Phi_{\alpha\alpha'}(kk'|\mathbf{f})}{\Delta M} \right]_c e_{\alpha'}^c(k'|l). \quad (\text{A2})$$

Here $\Phi_{\alpha\alpha'}(kk'|\mathbf{f})$ is the dynamic matrix of the crystal, and α and α' are Cartesian indices. The matrix Φ is given by a relation of the form

$$\Phi_{\alpha\alpha'}^c(kk'|\mathbf{f}) = \frac{1}{NM_c} \sum_{\mathbf{m}\mathbf{m}'} \varphi_{\alpha\alpha'}(\mathbf{m}\mathbf{k}, \mathbf{m}'\mathbf{k}') \times \exp[i\mathbf{f} \cdot (\mathbf{R}_{\mathbf{m}}^{(0)} - \mathbf{R}_{\mathbf{m}'}^{(0)})], \quad (\text{A3})$$

where $\varphi_{\alpha\alpha'}(\mathbf{m}\mathbf{k}, \mathbf{m}'\mathbf{k}')$ is the matrix of second-order force parameters, N is the number of unit cells, $\mathbf{R}_{\mathbf{m}}^0$ is the vector of the equilibrium position of the \mathbf{m} th unit cell.

According to (A3),

$$\left[\frac{\Delta \Phi_{\alpha\alpha'}^c(kk'|\mathbf{f})}{\Delta M} \right]_c = -\frac{1}{2M_c} \Phi_{\alpha\alpha'}^c(kk'|\mathbf{f}). \quad (\text{A4})$$

We substitute (A4) into (A2), and take into account that

$$\omega_c^2(l) e_{\alpha}^c(k|l) = \sum_{k', \alpha'} \Phi_{\alpha\alpha'}^c(kk'|\mathbf{f}) e_{\alpha'}^c(k'|l). \quad (\text{A5})$$

We also take into account the orthogonality condition for the eigenvectors. We note that the value of the mean mass varies in a continuous manner, so that the Δ 's can be replaced by differentials. As a result we obtain

$$\frac{d \ln \omega_c^2(l)}{d \ln M_c} = -1 + O\left[\left(\frac{|\Delta M|}{M_c}\right)^2, \frac{\Delta M}{M_c} \frac{\langle u^2 \rangle}{a^2}\right]. \quad (\text{A6})$$

*E-mail: zhernov@mail.ru

- ¹H. Holloway, K. C. Hass, M. A. Tamor, T. R. Anthony, and W. F. Banholzer, Phys. Rev. B **44**, 7123 (1991).
²H. D. Fuchs, C. M. Grein, R. I. Devien, J. Kuhl, and M. Cardona, Phys. Rev. B **44**, 8633 (1991).
³V. I. Ozhogin, A. V. Inyushkin, A. N. Toldenkov, G. É. Popov, Yu. Kholler, and K. Ito, JETP Lett. **63**, 490 (1996).
⁴W. S. Carpinski, H. J. Maris, E. Bauser, I. Siller, T. Ruf, M. Asen-Palmer,

- M. Cardona, and E. Gmelin, Appl. Phys. Lett. **71**, 2109 (1997).
⁵T. Ruf, R. W. Henn, M. Asen-Palmer, E. Gmelin, M. Cardona, H. J. Pohl, G. G. Devyatych, and P. G. Sennikov, Solid State Commun. **115**, 243 (2000).
⁶H. Bettger, *Principles of the Theory of Lattice Dynamics*, Akademie-Verlag, Berlin (1983).
⁷G. Leibfried, *Microscopic Theory of Mechanical and Thermal Properties of Crystals*, GIL, Moscow (1963).
⁸M. Cardona, Physica B **263–264**, 376 (1999).
⁹A. Kazemirov and M. Cardona, Science **282**, 930 (1998).
¹⁰V. I. Ozhogin, N. A. Babushkina, A. P. Belova, and A. P. Zhernov, Zh. Éksp. Teor. Fiz. **115**, 230 (1999) [JETP **88**, 135 (1999)].
¹¹P. Pavone and S. Baroni, Solid State Commun. **90**, 295 (1994).
¹²G. M. Rignanes, J. P. Michenaud, and X. Gonze, Phys. Rev. B **53**, 4488 (1996).
¹³A. P. Zhernov, Zh. Éksp. Teor. Fiz. **114**, 654 (1998) [JETP **87**, 357 (1998)].
¹⁴M. A. Asen-Palmer, N. Bartcovsky, E. Gmelin, M. Cardona, A. P. Zhernov, A. V. Inushkin, A. N. Toldenkov, V. I. Oghogin, K. M. Itoh, and E. E. Haller, Phys. Rev. B **56**, 9431 (1997).
¹⁵W. S. Carpinski and H. J. Maris, and S. Tamura, Phys. Rev. B **99**, 10105 (1999).
¹⁶S. I. Novikova, *Thermal Expansion of Solids* [in Russian] Nauka, Moscow (1979).
¹⁷T. H. Barron, J. G. Collins, and G. K. White, Adv. Phys. **29**, 609 (1980).
¹⁸G. Nilsen and G. Nelin, Phys. Rev. B **6**, 3772 (1972).
¹⁹G. Dolling and R. A. Cowley, Proc. Phys. Soc. (London) **88**, 463 (1966).
²⁰W. Weber, Phys. Rev. Lett. **33**, 371 (1974); Phys. Rev. B **15**, 4789 (1977).
²¹Resul Eryigit and Irving P. Herman, Phys. Rev. B **53**, 7775 (1996).
²²R. H. Carr, R. D. McCammon, and G. K. White, Proc. Phys. Soc. (London) Sect. A **280**, 72 (1964).
²³H. Ibach, Phys. Status Solidi **31**, 625 (1969).
²⁴E. Grüneisen, Handb. Sens. Physiol. **10**, 22 (1926).
²⁵F. Herman, J. Phys. Chem. Solids **8**, 405 (1959).
²⁶A. D. Zdetsis and C. S. Wang, Phys. Rev. **19**, 2999 (1979).
²⁷H. Jones, Phys. Rev. A **1**, 71 (1970).
²⁸A. P. Zhernov, Zh. Éksp. Teor. Fiz. **114**, 2153 (1998) [JETP **87**, 1172 (1998)].

Translated by Steve Torstveit

Anomalous low-temperature field evaporation and atomic relaxation of the tungsten surface

T. I. Mazilova and I. M. Mikhailovskij*

Kharkov Institute of Physics and Technology, National Science Center, ul. Akademicheskaya 1, 61108 Kharkov, Ukraine

N. Wanderka

Hahn-Meitner-Institut Berlin, Glinickertstrasse 100, D-14109 Berlin, Germany

(Submitted May 25, 2000)

Fiz. Nizk. Temp. **26**, 1236–1240 (December 2000)

The anomalous low-temperature field evaporation of atomic complexes on the (211) face of single-crystal tungsten is investigated by the methods of field ion microscopy. It is shown that as the size of the close-packed atomic islands decreases, the tangential rate of evaporation at 21 K increases by 2–3 orders of magnitude. The experimental results can be used to reveal and investigate atomic relaxation effects at steps on faces with low Miller indices. A method is proposed for determining the subatomic displacements of atoms on the steps as the size of the islands decreases. The observed relaxation effects can be described in a consistent manner in a model of linearly distributed surface forces. The observed size relaxation effect is treated as a response to an increase in the energy of the elastic stresses as the diameter of the atomic islands decreases. © 2000 American Institute of Physics. [S1063-777X(00)00912-9]

INTRODUCTION

The low-temperature evaporation of metals in high electric fields underlies the high-resolution methods of field ion microscopy, mass spectroscopy, and a number of promising trends in modern nanotechnology.^{1–4} Measurements of the threshold electric field and rate of evaporation at temperatures far below the Debye temperature can reveal the contribution of quantum effects in the vibrations of atoms on atomic steps.^{1,5} In the present paper we show that the previously observed anomalous low-temperature field evaporation of atomic complexes^{6,7} can be used to reveal and investigate atomic relaxation effects on the steps of faces with low Miller indices. Steps are a little-studied but important elements of surface morphology, having a substantial influence on the occurrence of chemical reactions,⁸ surface diffusivity,⁹ desorption kinetics,¹⁰ the formation of technically interesting surface nanostructures,¹¹ and so on.

EXPERIMENTAL TECHNIQUES

We investigated the kinetics of field evaporation of the (211) surface of tungsten in the temperature interval 21–78 K. Needle-shaped samples having a radius of curvature at the tip in the range of 6–50 nm were prepared by the electrochemical etching of 99.98% pure tungsten wires. The studies were carried out in the two-chamber field ion microscope at Kharkov Physics and Engineering Institute, with the samples cooled by liquid hydrogen and nitrogen. In the case of hydrogen cooling the residual gas pressure was 10^{-7} Pa. Experiments at intermediate temperatures were done on the ultrahigh-vacuum atom probe field ion microscope at the Hahn-Meitner-Institut in Berlin at a pressure of the active gases below 10^{-10} Pa. Helium at a pressure of $(1–2) \times 10^{-3}$ Pa was used as an imaging gas. The rate of evap-

ration was determined on the basis of a comparison of the successively obtained images of the evaporating surface of the needle-shaped tungsten single crystals.

During the evaporation the electric field was maintained constant at a level of $(5.6–5.7) \times 10^8$ V/cm. During the exposure of the images the electric field was reduced to the level of the best-image field (4.5×10^8 V/cm). At such fields an ionization barrier is created near the surface,² preventing the residual gas atoms, which are characterized by relatively low ionization potentials, from reaching the investigated part of the sample. Thus the ultrahigh-vacuum conditions and the presence of a field ionization barrier prevented the residual gas atoms from striking the surface under study. The migration of residual gases adsorbed on the surface of the shank of the sample, which was not shielded by the ionization barrier, was insignificant, at least at 21 K, and likewise did not lead to contamination of the investigated part of the sample.

RESULTS AND DISCUSSION

Figure 1a–1e shows a series of ion-microscope images of the (211) face, obtained at 21 K during field evaporation of a single atomic layer of a sample with a radius of curvature near the tip $R=25$ nm. The maximum radius of the two-dimensional atomic complexes (islands) was 2.1 nm (a), and the minimum was 1.7 nm (d). The experimental dependence of the evaporation rate dr/dt on the mean radius of curvature $\langle r \rangle$ of the atomic complex is shown in Fig. 2 (curve 1). When in the course of the field evaporation an island reaches a certain minimum (critical) radius r_c , the tangential evaporation rate increases anomalously by 2–3 orders of magnitude. As in the case of the anomalous low-temperature field evaporation of atomic complexes on the (110) face,⁶ the evaporation of complexes at $r < r_c$ occurred

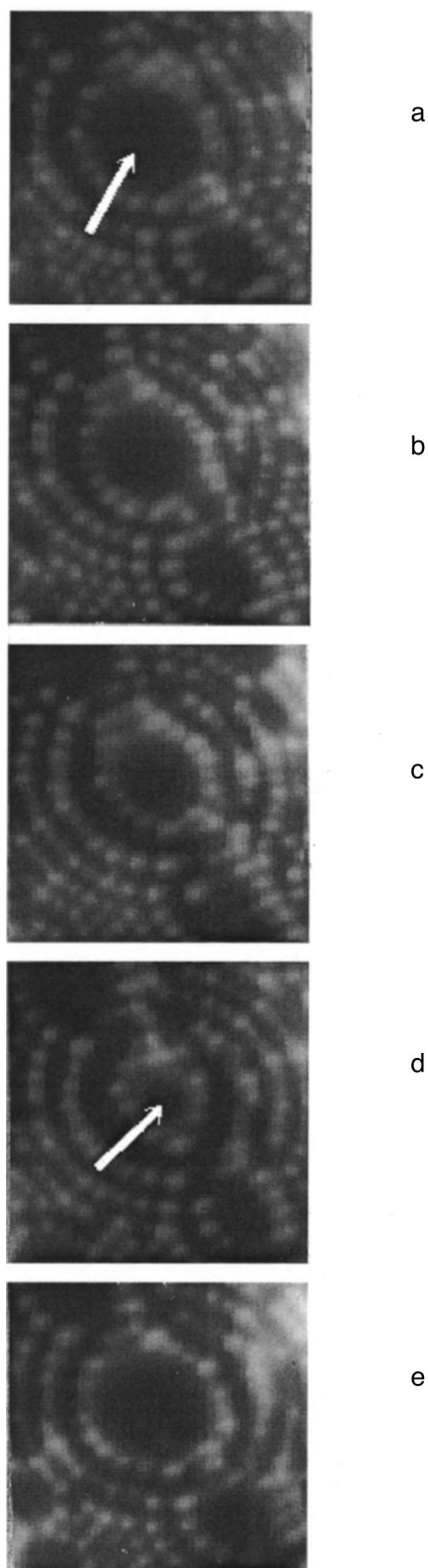


FIG. 1. Ion microscope images of an atomic island at the center of the (211) face of tungsten, obtained in the course of field evaporation at 21 K immediately after removal of the previous atomic layer (a) and after various times [min]: 6 (b), 12 (c), 18 (d), and 24 (d). The arrows indicate the centers of the atomic complexes of maximum (a) and minimum (d) sizes.

over a time equal in order of magnitude to the mean lifetime of a single atom on the (211) step for $r > r_c$. For this reason the evaporation of two-dimensional islands at $r < r_c$ in the investigated temperature interval 21–78 K can be regarded

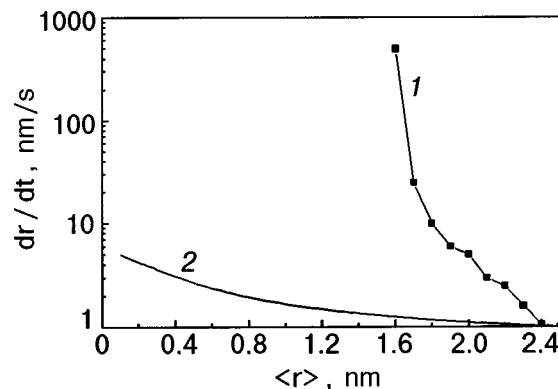


FIG. 2. Dependence of the evaporation rate on the mean radius of the atomic island: 1 — experimental curve, 2 — calculated curve obtained in the approximation of a rigid, unrelaxed lattice.

as a collective process. Unlike the field evaporation of the (110) face, however, the anomalous increase in the rate of evaporation of the islands was observed over the entire investigated range of values of the radius of curvature of the samples, 6–50 nm.

Despite the absence of a consistent model of the thermal activation and quantum-mechanical processes governing the evaporation of metals in high electric fields, for a quantitative analysis of the formation of the atomic topography of a surface in the course of field evaporation the problem is customarily treated geometrically, in particular, by the “shell model.”^{1,3} It is assumed that the atoms to be imaged by the ion microscope are located within a hemispherical shell 0.05–0.1 lattice parameters thick on the surface of the sample. The evaporation process is modeled as an inward displacement of the shell along an axis into the sample. Atoms are evaporated when they are displaced outward from the shell. The geometric model not only gives a satisfactory description of the atomic topography of the surface of ideal crystals but also permits one to analyze subatomic displacements on the ion-microscope images of dislocations, grain boundaries, twins, and other lattice defects. The accuracy of determination of the local subatomic displacements by means of one of the modifications of the geometric model — the method of indirect magnification — reaches 0.006 nm in the direction normal to the surface.¹² Curve 2 in Fig. 2 shows the dependence of the tangential evaporation rate on the radius r of the atomic step, according to a calculation by the indirect magnification method. According to that method, in the approximation of a rigid unrelaxed lattice for atomic islands with $r \ll R$ the tangential evaporation rate is given by

$$dr/dt = d_{hkl} K_e (R/2r)^{1/2}, \tag{1}$$

where d_{hkl} is the interplanar distance, and K_e is the normal rate of evaporation. In accordance with the experimental data, curve 2 in Fig. 2 was calculated for $R = 25$ nm, $K_e = 5.5 \times 10^{-4}$ atomic layers (211) per second, and $d_{hkl} = 0.129$ nm. It follows from Fig. 2 that the increase in the tangential evaporation rate with decreasing size of the atomic islands according to the geometric model without relaxation is substantially more gradual than the experimentally ob-

served effect and becomes appreciable only at island radii much smaller than r_c .

Quantitative agreement with the experimental data can be achieved in the framework of the geometric model for a relaxed lattice, on the assumption that the value of the atomic displacement U_z on steps in the [211] direction is a function of the radius r . In this approximation, for atomic islands with $r \ll R$ the change of the relaxation displacement of the atoms on the steps in the direction normal to the surface in the course of the evaporation process is expressed by the relation

$$\Delta U_z(r) = d_{hkl}(1 - K_e t) - r^2(t)/(2R), \quad (2)$$

where t is the evaporation time counted from the instant of evaporation of the previous complex. That instant corresponds to the maximum value of the radius of the atomic complex, $r = r_0$ (Fig. 1a), and the size-dependent part of the component of the displacements normal to the surface is defined as $\Delta U_z(r) = U_z(r) - U_z(r_0)$.

A calculation of the size dependence of the component of the atomic displacements normal to the surface on (211) steps according to formula (2) shows that a decrease in the radius of the atomic islands is accompanied by an outward displacement of the atoms of the steps. The value of the displacement corresponding to the critical radius of the island, $r_c = 1.9$ nm, is equal to 0.021 nm, or 16% of the interplanar distance d_{211} . Thus an analysis of the kinetics of the low-temperature evaporation of the (211) face of tungsten shows that the decrease in the radius of the islands in the course of the evaporation is accompanied by an increase in the height of the atomic steps. Within the limits of accuracy of the method of indirect magnification¹² these values are independent of temperature in the investigated interval 21–78 K. The observed size relaxation effects on the atomic steps of the islands are characterized by a high reproducibility. An anomalous growth in the rate of low-temperature field evaporation on reaching the critical radius was observed in all of the experiments done (more than 10^3). In control experiments done in the ultrahigh-vacuum atom probe field ion microscope, no features attributable to a change in the vacuum conditions were observed in the kinetics of the low-temperature evaporation of tungsten. This confirms the conclusion that the field ionization barrier is effective in preventing residual gas atoms from reaching the investigated part of the sample. The authors could not find any published data on the measurement of the relaxation of atoms at steps on the faces of metal surfaces. At present there are only data on the displacement of the atoms on the faces (terraces) with low Miller indices.¹³ It should be noted that the value of the size-dependent part of the component of the atomic displacements normal to the surface on the steps, $\Delta U_z(r)$, observed in this paper, is close in modulus to the values of the atomic relaxation determined previously by the methods of low-energy electron diffraction and computer simulation¹³ for atoms on terraces of the (211) face, but the displacements had the opposite sign.

Thus the anomalous growth of the rate of low-temperature field evaporation can be described quantitatively with allowance for the size dependence of the relaxational

displacements of surface atoms. We know of no published data on the experimental study of size-dependent relaxation effects on the surface of metals. Meanwhile, they have been analyzed with the use of a surface relaxation model proposed by Marchenko and Parshin,¹⁴ which satisfactorily describes a number of fine morphological effects on the surface of a wide class of solids — from cryocrystals¹⁵ to refractory metals.¹⁶ The authors of Ref. 14 showed that relaxation can be treated as a response of the subsurface layers to the action of rows of linearly distributed forces oriented along the atomic steps. The interaction of the steps on the surface is the result of a superposition of the elastic stress fields and, consequently, is of a long-range character. It is easy to show that in the framework of this model the energy of a circular step of radius r , treated as the interaction energy between all of the elements of the step, can be represented in the form

$$W_i(r) = (1 - \nu^2)\beta(f_s^2 - f_t^2)/(2rE), \quad (3)$$

where E is Young's modulus, ν is Poisson's ratio, β is a coefficient of the order of unity, f_s and f_t are linearly distributed surface forces of local tension and normal pressure. It is difficult to determine the values of $W_i(r)$ because of the lack of data on the surface forces f_s . However a recent analysis of the interaction of steps on the surface of platinum¹⁶ showed that the modulus of the ratio f_s/f_t is greater than unity, and thus, according to formula (3), one would expect a mutual repulsion of the steps, independently of their signs.

In addition to the force interaction of the steps there should also be an entropic repulsion due to the restriction on the number of possible configurations of the steps. The configurational repulsion should lead to an increase in the free energy of the stepped surface. However the entropic repulsion of surface steps usually becomes noticeable only at comparatively high temperatures. The displacement of the atoms on the steps as the size of the island decreases should be treated, in the framework of the model of Ref. 14, as a response to an increase in the energy of elastic stresses. Indeed, the nature of the atomic relaxation and the configuration of the elastic strain fields are determined almost entirely by the atomic displacements of the first surface layer.¹⁷ Thus the size relaxation effect observed in the present study leads to a decrease of the displacement of the first atomic plane into the crystal, lowering the density of surface forces and thereby compensating the growth of the energy of the steps as the size of the atomic islands decreases. This effect can play an important role in the nucleation and growth of crystals from the gas phase, heterogeneous catalysis, and other processes on nanostructured surfaces.

CONCLUSIONS

The application of the indirect magnification method of field ion microscopy, which makes it possible to achieve subatomic resolution, for analysis of the atomic morphology of the surface and the kinetics of low-temperature field evaporation has made it possible for the first time to obtain information about the relaxation processes occurring on atomic steps of close-packed faces.

1. We have observed experimentally the anomalous low-temperature evaporation of two-dimensional atomic islands on the (211) face of tungsten.

2. We have shown in the framework of the geometric model of the formation of atomic topography of a surface during field evaporation that the anomalous growth of the evaporation rate is due to a change in the state of relaxation of the surface layer.

3. We have shown that the decrease in the size of the two-dimensional islands on a metal surface is accompanied by an outward displacement of the atoms on the steps and by an increase in the height of the atomic steps.

4. In the framework of a model of linearly distributed surface forces, the displacement of the atoms on the steps as the size of the island decreases can be regarded as the response to an increase in the elastic stress energy.

The observed relaxation effects can have a substantial influence on surface chemical reactions, the kinetics of nucleation and growth of crystals from the vapor phase, surface diffusion, and other processes that are governed by the interaction of atoms with the steps of close-packed faces.

In closing the authors thank C. Abromeit, A. S. Bakayu, M-P. Macht, and V. Naundorf for a discussion of the results and for helpful advice.

*E-mail: mikhailovskij@kipt.kharkov.ua

- ¹R. Forbes, *Appl. Surf. Sci.* **87/88**, 1 (1995).
- ²M. K. Miller, L. Cerezo, M. G. Hetherington, and G. D. W. Smith, *Atom Probe Field Ion Microscopy*, Clarendon Press, Oxford (1996).
- ³I. M. Mikhaïlovskii, V. A. Ksenofontov, and T. I. Mazilova, *JETP Lett.* **65**, 537 (1997).
- ⁴T. I. Mazilova, *Fiz. Nizk. Temp.* **24**, 902 (1998) [*Low Temp. Phys.* **24**, 679 (1998)].
- ⁵I. M. Mikhaïlovskii and Zh. I. Dranova, *JETP Lett.* **22**, 125 (1975).
- ⁶I. M. Mikhaïlovskii, Zh. I. Dranova, V. A. Ksenofontov, and V. B. Kul'ko, *Zh. Eksp. Teor. Fiz.* **76**, 1309 (1979) [*Sov. Phys. JETP* **49**, 664 (1979)].
- ⁷A. L. Suvorov, *Structure and Properties of Surface Layers of Metals* [in Russian], Énergoatomizdat, Moscow (1989).
- ⁸D. S. Sholl and R. T. Skodje, *Surf. Sci.* **345**, 173 (1996).
- ⁹S. C. Wang and G. Ehrlich, *Phys. Rev. Lett.* **70**, 41 (1993).
- ¹⁰M. A. Henderson, A. Szabo, and J. T. Yates Jr., *J. Chem. Phys.* **91**, 7245 (1989).
- ¹¹S. H. Brongersma, M. R. Castell, D. D. Perovic, and M. Zinke-Allmann, *Phys. Rev. Lett.* **80**, 3795 (1998).
- ¹²I. M. Mikhaïlovskii, *Fiz. Tverd. Tela (Leningrad)* **24**, 3210 (1982) [*Sov. Phys. Solid State* **24**, 1822 (1982)].
- ¹³W. Xu and J. B. Adams, *Surf. Sci.* **319**, 45 (1994).
- ¹⁴V. I. Marchenko and A. Ya. Parshin, *Zh. Eksp. Teor. Fiz.* **79**, 257 (1980) [*Sov. Phys. JETP* **52**, 129 (1980)].
- ¹⁵V. I. Marchenko, *Zh. Eksp. Teor. Fiz.* **81**, 1140 (1981) [*Sov. Phys. JETP* **54**, 605 (1981)].
- ¹⁶K. Swamy, E. Bertel, and I. Vilfan, *Surf. Sci. Lett.* **425**, L369 (1999).
- ¹⁷D. J. Srolovitz and J. P. Hirth, *Surf. Sci.* **255**, 111 (1991).

Translated by Steve Torstveit

Fine structure of coherent twin boundaries in metals

T. I. Mazilova, I. M. Mikhailovskij,* and E. I. Lygovskaja

Kharkov Institute of Physics and Technology, National Science Center, ul. Akademicheskaya 1, 61108 Kharkov, Ukraine

(Submitted May 25, 2000)

Fiz. Nizk. Temp. **26**, 1241–1244 (December 2000)

The oscillatory features of the atomic relaxation on coherent twin boundary in tungsten are studied by the methods of molecular dynamics. A nonmonotonic character of the variation of the atomic density in the near-boundary region is established. It is shown that the relaxation near twin boundaries can be described satisfactorily in the framework of a continuum model of linearly distributed surface forces. © 2000 American Institute of Physics.
[S1063-777X(00)01012-4]

Mechanical twinning is an important form of low-temperature plastic deformation of metals with the bcc lattice. The development of high-resolution methods of field ion and transmission electron microscopy and computer simulation has yielded substantial progress in our understanding of the features of the atomic structure of coherent twin boundaries.^{1,2} Particular attention is being paid to the study of the structure of twin boundaries, since such boundaries can be regarded as the simplest example of special large-angle grain boundaries.² The introduction of the concept of a twinning dislocation by Vladimirskii³ has served as a starting point for the development of a dislocation model for twinning. Twinning dislocations compensate the deviation of the twin boundary from the symmetric orientation, which localizes the disruption of coherence at monatomic steps. These steps in a long-wavelength treatment are complete grain-boundary dislocations with Burgers vectors equal to the translation vector of the displacement shift complete lattice of superpositions² of the misoriented lattices of the matrix and twin. The objects of study in the continuum theory of twins were macroscopic pileups of twinning dislocations, found in equilibrium in an crystal stress field and with the drag forces of the crystal lattice. The Peierls relief of the lattice forces governing the mobility of the twinning dislocations was determined as a result of a microscopic treatment by the methods of molecular dynamics. A theoretical analysis of the structure of the twin boundaries on the basis of the continuum theory of dislocations made it possible to describe the basic features of the mechanical twinning processes.¹

Meanwhile, the theoretical treatment of the phenomenon of superconductivity localized near symmetric (dislocation-free) twin boundaries is largely based on the assumption that there exists a rather extended near-boundary region characterized by increased values of the electron–phonon interaction constant.^{4,5} The presence of elastic stresses of a nondislocational origin is also evidenced by the results of an analysis of the near-boundary strain field of the twins. In a microscopic determination of the elastic stress fields in the neighborhood of twins and symmetric grain boundaries^{1,6} one observes some features which cannot be described in terms of the continuum theory of dislocations. For this rea-

son, in the present study we use the methods of molecular dynamics to study the atomic structure and displacement field of atoms in the core of a coherent twin boundary in metals with the bcc lattice. A near-boundary atomic relaxation of the oscillatory type was observed, and it was shown that this sort of relaxation can be described in the framework of the continuum theory of elasticity.

The model crystallite had a bcc lattice containing 1385 atoms interacting with one another and with 5540 image atoms. As the interatomic potential we used the Johnson central pair potential determined for tungsten in Ref. 7. The influence of the medium was modeled by the boundary conditions at the external surface. For this, elastic forces proportional to the displacement and viscous forces proportional to the velocity of the surface atoms were specified. Cyclic boundary conditions were imposed at the faces normal to the plane of the boundary. As the initial structure we took an unrelaxed mirror-symmetric structure for the twin.

We found that the “energy” width of the twin boundary is substantially greater than the structural width. The atoms lying a distance r greater than one lattice constant a away from the central atomic plane $\{211\}$ have an energy that is 5 orders of magnitude above the 10^{-6} eV/atom background that arises on account of the approximate character of the potential and the presence of small atomic displacements due to the insufficiently complete relaxation of the structure. For $a < r < 2a$ the energy of the atoms exceeds the background by 2–3 order of magnitude, and for $r > 3.5a$ the atoms have essentially the background energy. The character of the decline in energy is described satisfactorily by a dependence $W = W_0 \exp(-r/r_0)$, where r_0 is the decay parameter for the energy, equal to 0.85 Å. In accordance with the results given in Ref. 6, the average values of the normal stress $1/3(\sigma_{xx} + \sigma_{yy} + \sigma_{zz})$ increased with decreasing r , reaching a value of 0.1μ where μ is the shear modulus. The maximum values of the stress corresponded to positions of the mutually repelling atoms in the planes closest to the plane of the boundary.

As a result of relaxation a displacement of the (211) atomic planes normal to the boundary occurred. There was no rigid shift in the direction normal to the axis of misorientation, and so the mirror-symmetric configuration was preserved. It follows from Fig. 1 that the near-boundary relax-

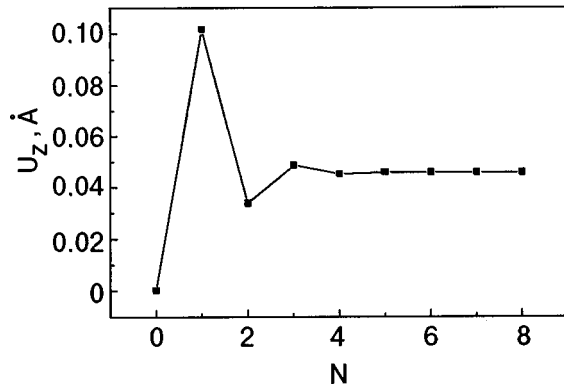


FIG. 1. Relaxation of the atomic planes near a coherent twin boundary in tungsten.

ation of the atomic planes has an oscillatory character. The oscillatory displacements of the atomic planes decays exponentially into the interior of the metal. An analogous character of the displacements of the atomic planes has been observed in the neighborhood of certain special symmetric boundaries in metals with the bcc and fcc lattices.^{2,8}

The origin of the oscillations of the interplanar distances in the neighborhood of special grain boundaries in some cases is due to the features of the local bending of the atomic planes in the neighborhoods of the cores of grain-boundary dislocations.² In the framework of the dislocation model of relaxation one can obtain a qualitative description of the density oscillations and the grain-boundary coalescence of atomic planes. However, there are no structural grain-boundary dislocations present at the twin boundary considered in the present paper, $\Sigma 3 \{112\} 70.32^\circ [110]$ nor at other symmetric commensurate grain boundaries with a high density of coincident sites. Analysis of the features of the stress field in the neighborhood of a twin boundary allows one to replace the complex pattern of interaction of adjacent crystallites by periodic rows of parallel line forces for describing the strain field. Linearly distributed forces are localized along the $\langle 111 \rangle$ directions, which have the maximum packing density at the twin boundary and are characterized by an increased stress level (up to 0.1μ). Here the adjacent crystallites are treated as elastic continua bounded by the plane of the surface. The distance L between the lines of application of the forces along the x axis for this type of boundary is equal to the lattice period in the direction normal to the axis of misorientation. The forces P_z , uniformly distributed along the misorientation axis y , are directed along the z axis, normal to the boundary.

The linearly distributed force P_z acting on the plane of the surface bounding the elastic half space generates a strain field⁹

$$\begin{aligned}
 e_{xx} &= \frac{2P_z(1+\sigma)}{\pi E} \frac{z}{x^2+z^2} \left(\sigma - \frac{x^2}{x^2+z^2} \right); \\
 e_{zz} &= \frac{2P_z(1+\sigma)}{\pi E} \frac{z}{x^2+z^2} \left(\sigma - \frac{z^2}{x^2+z^2} \right); \\
 e_{yy} &= 0,
 \end{aligned}
 \tag{1}$$

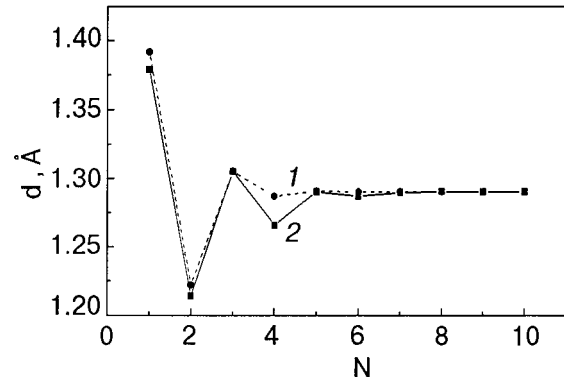


FIG. 2. Oscillations of the (112) interplanar distances near a symmetric twin boundary: 1 — continuum model, 2 — calculation by the molecular dynamics method.

where P_z is the value of the force per unit length, σ is Poisson's ratio, and E is Young's modulus.

The rows of linearly distributed forces for $z \gg L$ cause a uniform compression of the crystal. At the same time, as follows from the results of a computer simulation, at these distances from the twin boundary all components of the stress tensor go to zero. To ensure that the stresses equal zero at large z it is necessary to subtract from the displacement field created by the system of parallel line forces those displacements that give rise to a long-range stress field:¹⁰

$$\begin{aligned}
 U_z &= \frac{P_z(1+\sigma)}{2\pi E} \left\{ Z \left[\frac{\sinh(Z)}{\cosh(Z) - \cos(X)} - 2\sigma + 1 \right] \right. \\
 &\quad \left. - 2(1-\sigma) \ln[\cosh(Z) - \cos(X)] \right\},
 \end{aligned}
 \tag{2}$$

where $X = 2\pi x/L$ and $Z = 2\pi z/L$.

At the boundary under consideration, $\chi 3 \{112\}$ the displacements of the atoms of the i th (112) plane can be represented in the form

$$x_i - x = ia/2[110].
 \tag{3}$$

The local values of the interplanar distances between the i th and the $(i+1)$ -th atomic layers was determined from Eqs. (2) and (3) as $d_i = d + (U_{i+1} - U_i)$. Curve 1 in Fig. 2 shows the dependence of the interplane distances (112) on the distance away from the twin boundary, expressed as a number of atomic layers, according to a calculation in the continuum model. Also shown for comparison are the results calculated by the method of molecular dynamics (curve 2). The model of linearly distributed forces is of a semi-microscopic character, since it contains the phenomenological parameter P_z , the value of which cannot be determined in the framework of the theory of elasticity. For this reason the value of P_z , which is needed for calculating the absolute values of the distances between atomic layers, was determined from a best fit of the calculated and experimental curves. It follows from Fig. 2 that the periods and phases of the oscillations determined in the computer simulations agree with those calculated in the continuum model. The character of the damping in both cases is close to exponential. At comparatively large distances from the boundary, U_z falls off as $z \exp(-z/z_0)$, where z_0 is the damping parameter. However, the damping rate of the oscillations in the computer simulations was ap-

proximately 20% lower than the rate calculated in the continuum model. The damping parameter z_0 determined by the molecular dynamics method is 0.92 Å. In the continuum model of linearly distributed surface forces one has $z_0 = a[110]/2\pi = 0.71$ Å. On the whole it can be concluded that the continuum model of linearly distributed forces can give a satisfactory quantitative description of the oscillatory character of the atomic relaxation at a twin boundary.

*E-mail: mikhailovskij@kipt.kharkov.ua

¹V. S. Boiko, R. I. Garber, and A. M. Kosevich, *Reversible Plasticity of Crystals* [in Russian], Nauka, Moscow (1991).

²A. P. Sutton and R. W. Balluffi, *Interfaces in Crystalline Materials*, Clarendon Press, Oxford (1995).

³K. V. Vladimirov, *Zh. Eksp. Teor. Fiz.* **17**, 530 (1947).

⁴I. N. Khlyustikov and A. I. Buzdin, *Usp. Fiz. Nauk* **155**, 47 (1988) [*Sov. Phys. Usp.* **31**, 409 (1988)].

⁵V. I. Sokolenko and Ya. D. Starodubov, *Fiz. Nizk. Temp.* **19**, 951 (1993) [*Low Temp. Phys.* **19**, 675 (1993)].

⁶V. S. Boiko, T. I. Mazilova, and A. N. Orlov, *Vopr. At. Nauki Tekh. Ser. Fiz. Radiats. Povrezhd. Radiats. Materialoved. (Kharkov)* **2**(44), 3 (1988).

⁷R. A. Johnson, *Phys. Rev. B* **27**, 2014 (1983).

⁸P. A. Bereznyak, O. A. Velikodnaya, T. I. Mazilova, and I. M. Mikhailovskii, *JETP Lett.* **59**, 542 (1994).

⁹L. D. Landau and E. M. Lifshitz, *Theory of Elasticity*, 2nd ed. [Clarendon Press, Oxford (1970); Nauka, Moscow (1965)].

¹⁰D. J. Sroloviz and J. P. Hirth, *Surf. Sci.* **255**, 111 (1991).

Translated by Steve Torstveit

LOW-TEMPERATURE PHYSICS OF PLASTICITY AND STRENGTH

Low-temperature strain aging in In–Pb alloys under conditions of stress relaxation

L. S. Fomenko*

B. Verkin Institute for Low Temperature Physics and Engineering, National Academy of Sciences of Ukraine, pr. Lenina 47, 61164 Kharkov, Ukraine

(Submitted April 26, 2000; revised June 27, 2000)

Fiz. Nizk. Temp. **26**, 1245–1255 (December 2000)

In the stress-relaxation regime the dynamic strain aging (DSA) in single crystals of the substitutional solid solutions of substitution In–Pb with 6 and 8 at. % Pb is investigated at temperatures of 77–205 K. It is determined how the DSA-related post-relaxation hardening depends on the duration of the stress relaxation, the rate of change of the stress at the end of the relaxation, the temperature, the concentration of the alloy, the flow stress, and the degree of deformation. It is shown that the DSA kinetics is described by an equation of the Harper type with an exponent of 1/3 and a low value of the activation energy for the process (0.3–0.34 eV), which makes for a low temperature for the onset of DSA ($\sim 0.17 T_m$, where T_m is the melting temperature) and is indicative of a pipe character of the diffusion. It is assumed that the obstacles to the motion of dislocations in these crystals are impurity complexes, the strength of which increases during DSA as a result of the pipe diffusion of impurity atoms along dislocations. © 2000 American Institute of Physics.
[S1063-777X(00)01112-9]

INTRODUCTION

At sufficiently low temperatures the diffusion of impurities in a solid solution is difficult, and individual impurity atoms create local static potential barriers for the motion of dislocations.^{1,2} As the temperature increases, an important role in the development of plastic deformation comes to be played by processes related to the diffusion mobility of the impurities.^{1–4} The diffusion of dissolved atoms toward moving dislocations increases the effective resistance to their slip. This effect, which has been given the name “dynamic strain aging” (DSA),^{5–8} leads to such specific features in the kinetics of plastic flow of alloys in the active deformation regime as the Portevin–Le Chatelier effect (unstable or intermittent plastic flow).²

One of the macroscopic manifestations of DSA is the post-relaxation effect, which will be the subject of this paper. This effect consists in the elevation of the flow stress upon repeated loading of a sample after stress relaxation and is detected as the presence of a “yield point.”^{7,9–13}

It should be noted that DSA, which is directly related to diffusion processes in the alloy, can be observed at rather low temperatures $T \approx (0.1–0.2)T_m$ (T_m is the melting temperature of the alloy),^{9,13} whereas the bulk diffusion is activated only at $T \geq (0.4–0.5)T_m$. The causes of the low-temperature onset of DSA are discussed below.

To elucidate the concrete mechanism of DSA and for understanding the nature of plastic deformation in alloys, it is important to study the kinetics and to determine the parameters of the process. In this paper we study the DSA kinetics under conditions of stress relaxation in single crystals of In–Pb solid solutions and investigate the influence of the flow stress, the degree of deformation, the temperature,

and the impurity concentration on the parameters of the DSA. The DSA kinetics in In–Pb alloys has substantially different behavior from that predicted by a theory in which individual impurity atoms diffusing from the bulk of the crystal are assumed to segregate on individual dislocations.^{1,2} The results argue in favor of a pipe mechanism of diffusion of the impurity atoms.

1. EXPERIMENTAL PROCEDURE

We studied single crystals of In–Pb substitutional solid solutions with 6 and 8 at. % Pb (the solubility limit of Pb in In is ~ 12 at. %). The techniques of crystal growth and sample preparation are described in detail in Ref. 14. Single crystals having a [001] axis after growth¹ were transformed by twinning to an orientation with an axis close to [100] (the twinning occurred at a stress which is a factor of 20 smaller than the yield stress for slip).

Samples with dimensions of $5 \times 5 \times 15$ mm were deformed by compression along the [100] direction at a rate of $\sim 10^{-4} \text{ s}^{-1}$ in the interval 77–205 K (in this temperature interval the post-relaxation effect was especially pronounced). The plastic flow was realized through slip, as twinning was geometrically forbidden. The aging experiments were done at a fixed temperature in the stress relaxation regime (a static strain aging scheme⁷). Under these conditions the dislocations execute only small displacements with a decaying velocity and so provide only an insignificant deformation of the sample, $\sim 0.1\%$. After the sample is held in the stress relaxation regime for a specified time interval the straining machine was again engaged and the straining of the sample continued at the previous rate. Starting at a deformation of $\sim 1–2\%$, upon repeated loading of the sample

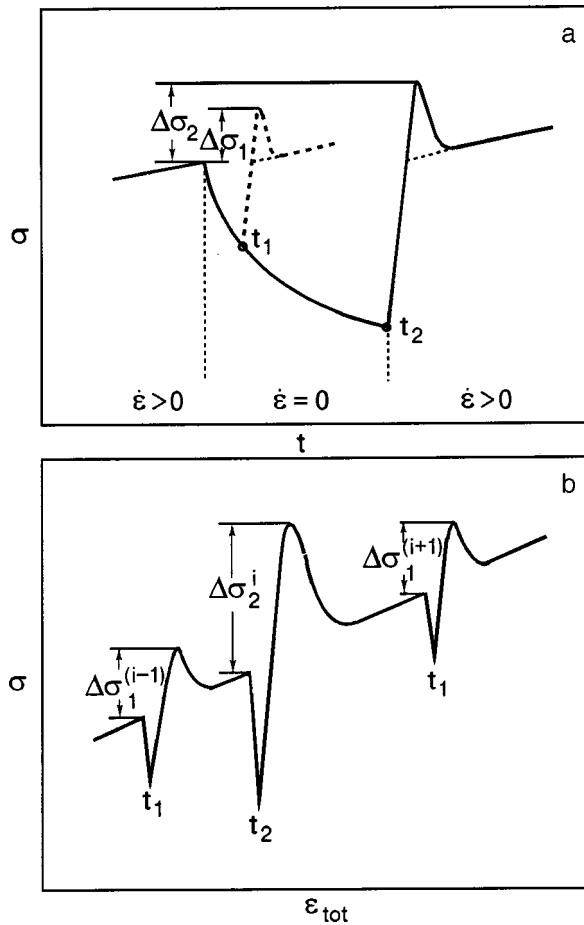


FIG. 1. Schematic illustration of the parts of the deformation curves (the regime of active deformation with a constant rate $\dot{\epsilon} > 0$) and the relaxation curves ($\dot{\epsilon} = 0$) in the coordinates of stress σ versus the time t (a) and stress σ versus total deformation ϵ_{tot} of the sample-machine system (b). $\Delta\sigma_1$, $\Delta\sigma_2$, $\Delta\sigma_1^{i-1}$, $\Delta\sigma_1^{i+1}$, $\Delta\sigma_2^i$ are the values of the post-relaxation hardening (the subscript indicates the duration of the stress relaxation, t_1 or t_2 , and the superscript is the number of the stress relaxation episode).

following relaxation a yield platform or yield point appeared, after which the deformation continued with the initial hardening coefficient, as can be seen in Fig. 1. The observed effect was characterized by the value of the post-relaxation hardening $\Delta\sigma$. This quantity is equal to the difference between the stress corresponding to the tip of the yield point or yield platform and the stress at the start of the relaxation. The post-relaxation hardening increases with increasing hold time of the sample in the stress relaxation regime (the duration of the stress relaxation): $\Delta\sigma_2 > \Delta\sigma_1$ if $t_2 > t_1$ (see the diagram in Fig. 1a). In this study we have obtained the dependence of $\Delta\sigma$ on the duration t of the stress relaxation, the rate of change of the stress at the end of the stress relaxation ($-\dot{\sigma}_r$), the temperature T , the value of the flow stress σ , and the degree of plastic deformation ϵ of the sample.

To avoid scatter due to the specific defect structure of the different samples, the entire $\Delta\sigma(t)$ curve was obtained on the same sample. No fewer than 15–20 experiments with stress relaxation of different durations were carried out. Owing to the strain hardening, the value of the flow stress did not remain constant. To minimize the distortions of the $\Delta\sigma(t)$ curve from these circumstances, the measurements were made in a deformation interval in which the flow stress

(degree of deformation) had only an insignificant effect on the post-relaxation hardening. This interval amounted to approximately 5% and began at the deformation corresponding to where the deformation curve goes out to the minimum hardening coefficient (see Sec. 2.4 for details).

To determine the dependence of the DSA parameters on the value of the flow stress (degree of deformation) we used the following procedure. Along the whole deformation curve we measured the value of the post-relaxation hardening at two alternating fixed relaxation durations t_1 and t_2 (see Fig. 1b). The durations t_1 and t_2 were chosen so that t_2 corresponded to the transition to the saturation region of the effect, and t_1 was a factor of 8 shorter than t_2 . Each flow stress σ_i (degree of deformation ϵ_i) at which the i th stress relaxation was carried out was placed in correspondence with two values of the post-relaxation hardening. One of these values, the parameter $\Delta\sigma_1^i$ (the superscript indicates the number of the stress relaxation episode, and the subscript corresponds to the relaxation duration t_1 or t_2), actually corresponded to a given stress (degree of deformation ϵ_i), while the other value $\Delta\sigma_2^i$ was taken as the arithmetic mean between the preceding ($\Delta\sigma_2^{i-1}$) and succeeding ($\Delta\sigma_2^{i+1}$) values. Then for each chosen flow stress σ_i (degree of deformation ϵ_i) there are two pairs of points: $(\Delta\sigma_1^i, t_1)$ and $(\Delta\sigma_2^i, t_2)$. Solving the system of two equations of the type in (1) (see below), we find the parameters $\Delta\sigma_{max}$ and t_c corresponding to the given flow stress σ_i (degree of deformation ϵ_i).

2. EXPERIMENTAL RESULTS

2.1. Influence of the duration of the stress relaxation

The data obtained on the dependence of the post-relaxation hardening $\Delta\sigma$ on the duration t of the stress relaxation are well described by the equation

$$\Delta\sigma = \Delta\sigma_{max} \{1 - \exp[-(t/t_c)^{1/3}]\}, \quad (1)$$

and in the early stages of the process, for $t \ll t_c$, by the power-law function

$$\Delta\sigma = At^{1/3}, \quad (2)$$

where $\Delta\sigma_{max}$ is the value of the hardening at $t \rightarrow \infty$, $A = \Delta\sigma_{max}/t_c^{1/3}$, and t_c is the characteristic time. Figure 2 shows the $\Delta\sigma(t)$ data obtained for the In-6 at. % Pb alloy at $T = 120$ K in comparison with the curves calculated according to Eqs. (1) and (2). Each point on the $\Delta\sigma(t)$ plot corresponds to an individual experiment on stress relaxation with a duration t and a final depth $\Delta\sigma_r(t) = \sigma_r(0) - \sigma_r(t)$, where $\sigma_r(0)$ and $\sigma_r(t)$ are the values of the stress at the beginning and end of the relaxation. From the $\Delta\sigma_r(t)$ plot shown in Fig. 2 it is seen that the relaxation depth remains practically constant ($\Delta\sigma_r \leq 0.4$ MPa) for $t \geq 30$ s. This indicates that the observed post-relaxation effect cannot be explained by strain hardening in the course of the stress relaxation.¹⁵ Indeed, when the relaxation curves go to saturation the dislocations in the crystal are practically immobile, and strain hardening does not occur. At the same time, the value of the post-relaxation hardening continues to grow by the law in Eq. (1), in agreement with the hypothesis that the observed effect is due to a DSA process.

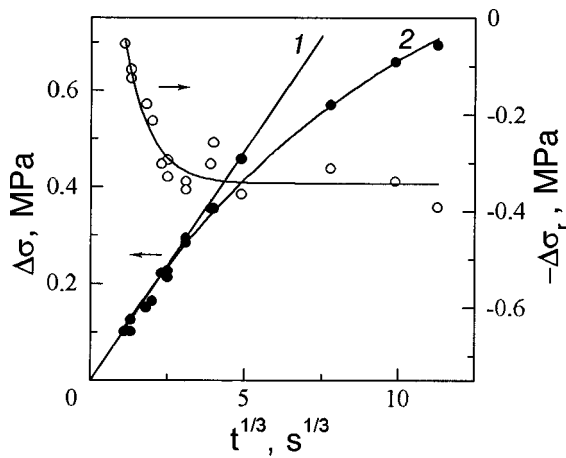


FIG. 2. Influence of the duration t of the stress relaxation on the value of the post-relaxation hardening $\Delta\sigma$ (●) and on the relaxation depth $\Delta\sigma_r$ (○). A crystal of In-6 at. % Pb, $T=120$ K. The straight line 1 corresponds to the equation $\Delta\sigma=At^{1/3}$, curve 2 to $\Delta\sigma=\Delta\sigma_{\max}\{1-\exp[-(t/t_c)^{1/3}]\}$ for the following parameter values: $\Delta\sigma_{\max}=1.02$ MPa, $t_c=864$ s, $A=0.1$ MPa·s $^{1/3}$.

2.2. Influence of the rate of change of the stress at the end of the relaxation

According to commonly accepted ideas, the aging of a dislocation occurs at the time when it is stopped in front of an obstacle. The aging time is equal to the waiting time t_w for thermal activation of the dislocation for overcoming of the barrier.³⁻⁸ The waiting time increases with decreasing rate of stress relaxation according to the law⁹

$$t_w = N / (-\dot{\sigma}_r), \tag{3}$$

where N is proportional to the density of mobile dislocations. If the density of mobile dislocations remains constant over the course of the relaxation, then it would be more correct to analyze the dependence of the post-relaxation hardening not on the duration of the stress relaxation but rather on the rate of change of the flow stress at the end of the relaxation $(-\dot{\sigma}_r)$.⁹ The rates $(-\dot{\sigma}_r)$ measured in our experiments corresponded, as a rule, to short times $t \ll t_c$, so that the equation describing the beginning state of DSA was valid:

$$\Delta\sigma = B(-\dot{\sigma}_r)^{-1/3}, \tag{4}$$

where B is a quantity that depends on the temperature, the impurity concentration, and the flow stress (degree of deformation).

Obtaining the dependence $\Delta\sigma(-\dot{\sigma}_r)$ over a wide interval of rates of change of the stress is complicated by the fact that it is difficult to measure $(-\dot{\sigma}_r)$ values lower than 10^{-4} MPa/s. Only for $T \geq 150$ K do the $\Delta\sigma(-\dot{\sigma}_r)$ curves show a deviation of the experimental data from relation (4) in the region of small $(-\dot{\sigma}_r)$ (see Fig. 3). It follows from a comparison of Eqs. (2) and (4) with allowance for Eq. (3) that under the particular conditions of the experiment on In-Pb alloys that the waiting time t_w for dislocations stopped at obstacles is proportional to the duration t of the stress relaxation, specifically: $t_w \approx (A/B)^3 N t$. From here an analysis of the dependence of the post-relaxation hardening on the duration of the stress relaxation seems within reach. It must

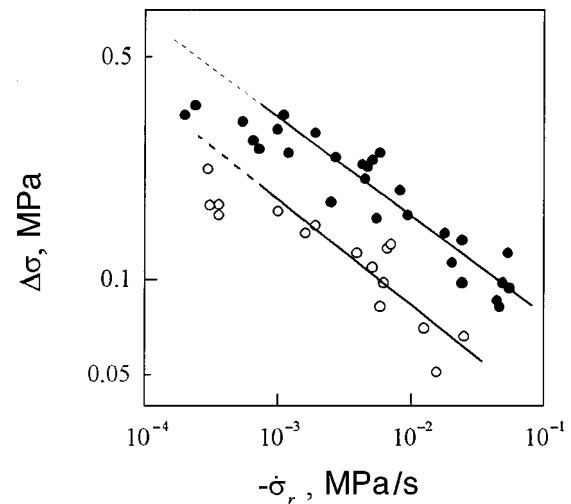


FIG. 3. Dependence of the post-relaxation hardening $\Delta\sigma$ on the rate of change of the flow stress at the end of the relaxation $(-\dot{\sigma}_r)$. Crystal of the alloy In-6 at. % Pb, $T=150$ K (●) and 170 K (○). The slope of the straight lines (representing a least-squares fit to the data) corresponds to an exponent n in the power law $\Delta\sigma=B(-\dot{\sigma}_r)^n$ equal to 0.31 (●) and 0.33 (○).

only be kept in mind that the characteristic time determined from these relations is larger than the actual time by a factor of $(B/A)^3/N$.

2.3. Influence of temperature

Starting from the $\Delta\sigma(t)$ curves obtained for different temperatures, we determined the temperature dependence of the DSA parameters, namely $t_c(T)$, $\Delta\sigma_{\max}(T)$, and $A(T)$, using Eqs. (1) and (2).

The characteristic time t_c and the maximum hardening $\Delta\sigma_{\max}$ increased as the temperature was lowered (Figs. 4 and 5). The parameter A found from the initial slope of the $\Delta\sigma(t)$ curves varies nonmonotonically with temperature, exhibiting a maximum at $T \approx 130-140$ K (Fig. 6).

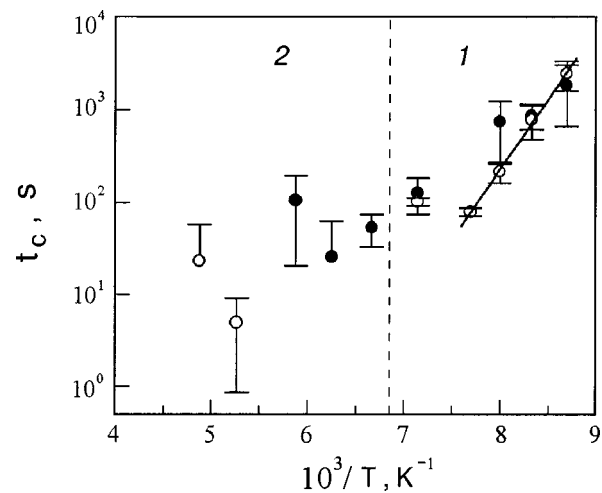


FIG. 4. Temperature dependence of the characteristic time t_c in crystals of In-6 at. % Pb (●) and In-8 at. % Pb (○). In region 1 the deformation curves are smooth, while in region 2 they are intermittent.

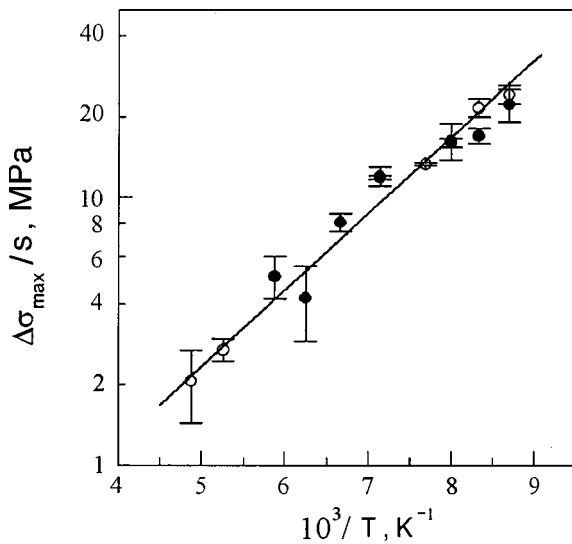


FIG. 5. Temperature dependence of the maximum hardening $\Delta\sigma_{\max}$ divided by the impurity concentration c , in crystals of In-6 at. % Pb (●) and In-8 at. % Pb (○).

In the temperature interval 115–130 K (region 1 in Fig. 4) the $t_c(T)$ curves for both alloys can be described approximately by a single expression:

$$t_c = t_{c0} \exp(\Delta H/kT), \quad (5)$$

where the activation energy $\Delta H \approx 0.3$ eV. At temperatures $T \geq 140$ K (region 2 in Fig. 4) one observes a marked weakening of the temperature dependence of the characteristic time and a large error in the determination of t_c . For this same interval (150–205 K) the deformation curves begin to have a jumplike character (the Portevin–Le Chatelier effect).

Unlike the characteristic time, the maximum hardening is proportional to the impurity concentration, so that a unified temperature dependence of the maximum hardening per unit impurity concentration, $\Delta\sigma_{\max}/c$, was obtained for the

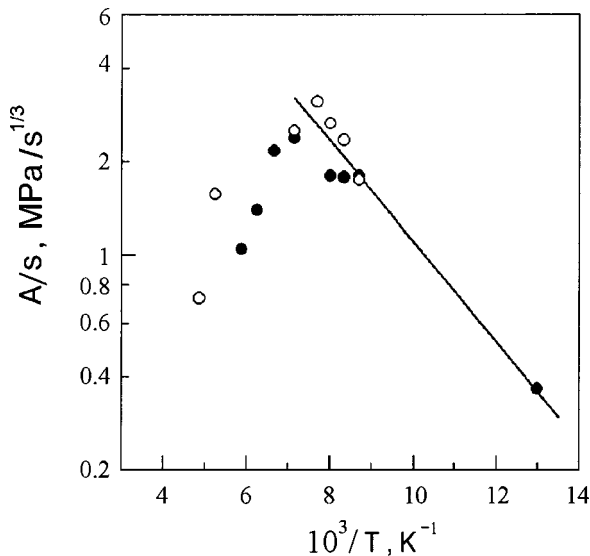


FIG. 6. Temperature dependence of the coefficient A in Eq. (2) divided by the lead concentration c , in crystals of In-6 at. % Pb (●) and In-8 at. % Pb (○).

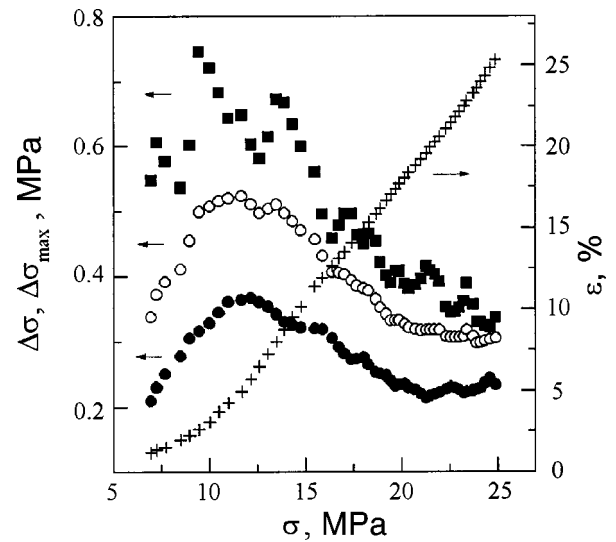


FIG. 7. Influence of the flow stress σ on the value of the post-relaxation hardening $\Delta\sigma$ for relaxation durations $t_1=60$ s (●) and $t_2=480$ s (○) and on the maximum hardening $\Delta\sigma_{\max}$ (■); crystal of In-6 at. % Pb; + — the deformation curve $\sigma(\varepsilon)$; $T=125$ K.

two alloys (Fig. 5). It is seen in the figure that when the temperature is reduced from 205 to 115 K the maximum hardening increases by more than an order of magnitude. The plot of $\Delta\sigma_{\max}(T)/c$ is well described by an exponential function with an activation energy $W=0.057$ eV. This value can be interpreted as the binding energy of a dislocation to an impurity atom (see below).

2.4. Influence of the flow stress (degree of deformation)

The value of the post-relaxation hardening corresponding to the same relaxation time varies considerably along the deformation curve. We therefore obtained and analyzed the dependence of $\Delta\sigma$ on the flow stress σ and deformation ε for two temperatures, 115 and 125 K. The following values of the duration of the stress relaxation were chosen: $t_1=180$ s, $t_2=1440$ s at $T=115$ K, and $t_1=60$ s, $t_2=480$ s at $T=125$ K. Figure 7 shows a plot of $\Delta\sigma(\sigma)$ obtained at $T=125$ K for the alloy In-6 at. % Pb. Also shown here is the corresponding deformation curve. There is typically a sharp increase in $\Delta\sigma$ in the initial stage of deformation (up until the start of the steady plastic flow with a nearly constant strain hardening coefficient), which as the deformation develops gives way to a falloff of $\Delta\sigma$ to roughly the initial level. A similar plot of $\Delta\sigma(\sigma)$ was obtained at $T=115$ K for the alloy with 6 at. % Pb. For the alloy with 8 at. % Pb the decrease of $\Delta\sigma$ is not as strong, so that the maximum value reached falls off by 20–25% instead of the 40–45% in the alloy with 6 at. % Pb.

The values estimated for the strain aging parameters t_c and $\Delta\sigma_{\max}$ by the procedure described above also vary substantially along the deformation curve. The behavior of $\Delta\sigma_{\max}$ qualitatively repeats the behavior of $\Delta\sigma$: growth on the part of the $\sigma(\varepsilon)$ curve up to the start of the steady plastic flow, and a falloff with further deformation of the sample (Fig. 8). In the interval of deformations from 5 to 15% prac-

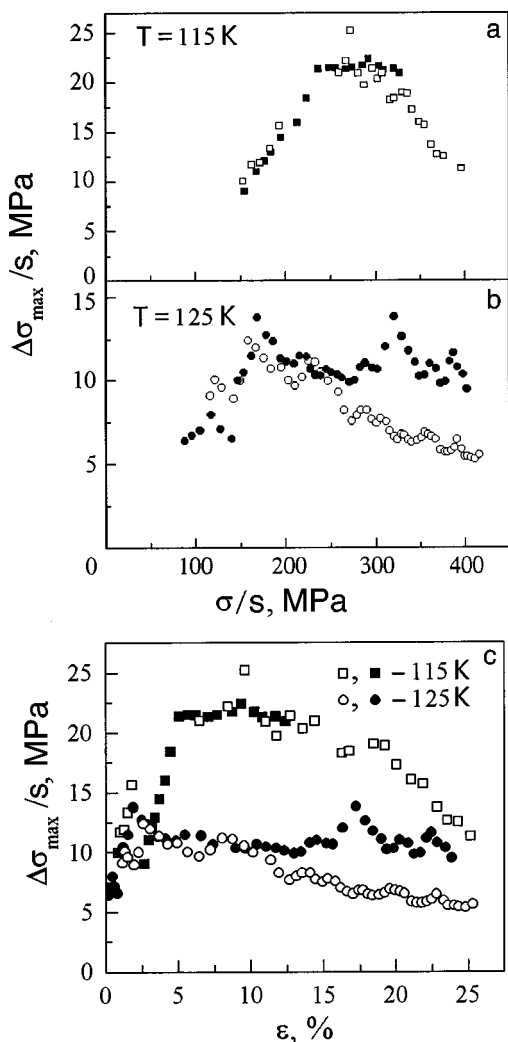


FIG. 8. Maximum hardening $\Delta\sigma_{\max}$ divided by the lead concentration c , versus the flow stress σ divided by the lead concentration c (a,b) and versus the deformation ε (c). The unfilled symbols are for the In-6 at. % Pb crystal, the filled symbols are for In-8 at. % Pb.

tically independent of the deformation (see Fig. 8c). The characteristic time behaves in a complicated way on the initial part of the deformation curve and at large degrees of deformation (Fig. 9). However, one can discern a considerable interval of deformations (from 5% to 15% at 115 K and from 5% to 23% at 125 K) in which t_c remains practically constant. In that region of deformations the characteristic time does not depend on the concentration of the alloy but varies substantially with temperature. The activation energy calculated according to formula (5) for the region in which the characteristic time is independent of the degree of deformation is approximately equal to 0.34 eV, which is close to the value given previously.

3. DISCUSSION

The measured dependence of the value of the post-relaxation hardening on the duration of the stress relaxation and temperature [Eqs. (1), (2), (4), and (5)] indicates that the process is of a diffusional nature. The post-relaxation effect is not observed in pure indium, and its value increases with increasing impurity concentration, so that there is every rea-

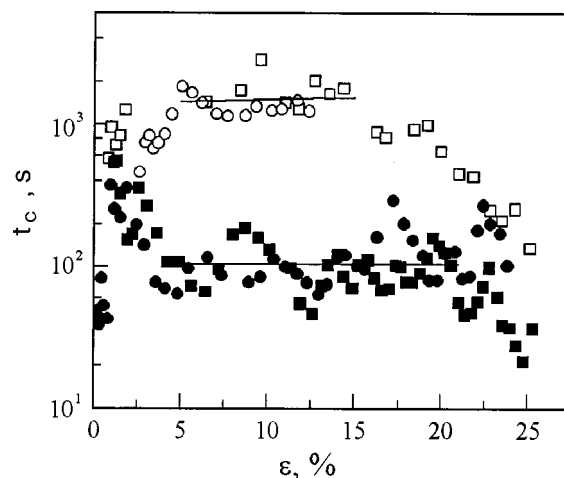


FIG. 9. Influence of the degree of deformation ε on the value of the characteristic time t_c in alloys with 6 at. % Pb (\square, \blacksquare) and 8 at. % Pb (\circ, \bullet) at temperatures of 115 K (\square, \circ) and 125 K (\blacksquare, \bullet). The straight lines represent a linear approximation of the experimental points for the corresponding deformation intervals.

son to assume that it is due to a DSA process. This is also indicated by the Portevin–Le Chatelier effect, which is manifested in the temperature interval 150–205 K in the active deformation regime. The results will be analyzed in terms of the known models for DSA.

The first quantitative model of DSA, the impurity drag model proposed by Cottrell,¹ considers the interaction of mobile impurities with continuously moving dislocations. In the framework of this model: 1) it was shown that dislocations with velocities not exceeding a critical velocity are surrounded by impurity atmospheres that are dragged by the dislocations; 2) the drag force exerted on a dislocation by the impurity atmosphere was analyzed as a function of temperature and the dislocation velocity; 3) the interval of velocities corresponding to a negative velocity sensitivity of the drag force (because of a decrease in the size of the impurity atmosphere as the dislocation velocity increases) was determined. The unstable motion of dislocations in this velocity interval might be the cause of the instability of the plastic flow of the crystal (the Portevin–Le Chatelier effect). The Cottrell model was able to explain qualitatively the experimental temperature and velocity dependence of the critical deformation ε_c , beginning with which the plastic flow becomes intermittent. However, the model does not predict an influence of the alloy concentration on ε_c or on DSA in general, and the calculated values of ε_c are many orders of magnitude greater than the values observed experimentally.⁴

In for this reason, a number of other models have been proposed to explain the effects due to DSA and which occur in a region of temperatures that is low in comparison with the characteristic temperatures for bulk diffusion processes. These models have nevertheless used some ideas developed by Cottrell, primarily that of taking into account the role of nonequilibrium vacancies formed as a result of the plastic deformation of the crystal and which correspond to growth of the bulk diffusion coefficient D :

$$D \propto C_v \exp(-Q_m/kT), \tag{6}$$

where C_v is the concentration of nonequilibrium vacancies, and Q_m is the activation energy for migration of the impurity atoms. In addition, Cottrell and Bilby solved the problem of the segregation of point defects on a rectilinear edge dislocation and obtained an expression for the increment of the linear density of impurity atoms on a dislocation over the course of the aging time t_a :¹

$$\Delta C \propto c(Dt_a)^{2/3}. \quad (7)$$

In solving this problem, Cottrell and Bilby took into account only the drift flux of the impurity atoms. Because the flux due to concentration gradients was neglected and boundary conditions treating a dislocation as an ideal sink for impurity atoms were used, Eq. (7) describes only the early stages of the segregation of dissolved atoms on dislocations. The later stages of the process are well described by the semiempirical Harper equation:¹⁶

$$\Delta C = \Delta C_{\max} \{1 - \exp[-(t_a/t_c)^{2/3}]\}, \quad (8)$$

which at aging times $t_a \ll t_c$ goes over to the Cottrell–Bilby equation. We note that Cottrell and Bilby’s expression (7) is still widely used today.

The modern DSA models^{3–9,17–21} (these are listed in Table I for convenience) proceed from the idea of intermittent (jumplike) motion of the dislocations during the deformation process, as is characteristic for thermally activated plastic deformation. Here it is assumed that the DSA occurs not at the time of the actual motion of the dislocations but during the waiting time t_w for thermal activation at local obstacles. For this reason these models are often called static models⁴ in distinction to the dynamic model of Cottrell. According to the static models, the aging process consists of either a decrease in the distance between obstacles (along the dislocation line) at a constant dislocation strength (models 1.1 and 1.2; see Table I),^{4,5,8,17} or of an increase in the strength of the obstacles in front of which the dislocations are stopped, at a constant distance between them (models 1.3, 1.4, 2.1, and 2.2).^{3,6–9,18–21} As obstacles for the motion of dislocations, single impurity atoms or their complexes (models 1.1–1.4)^{4,5,8,9,17,18} and also “forest” dislocations (models 2.1 and 2.2).^{3,6,7,19–21}

It follows from an analysis of column 6 of Table I that the experimental dependence of the DSA parameters on the value of the flow stress (degree of deformation) can serve as the deciding factor in the choice of a specific DSA model (more precisely, of a specific type of obstacle). Indeed, according to Refs. 6 and 7 (models 2.1 and 2.2), $\Delta\sigma$ (and also $\Delta\sigma_{\max}$ when the Harper equation holds) increases linearly with increasing flow stress if the main obstacles that change their strength during DSA are forest dislocations. Such a dependence is a consequence of a deformation-induced growth in the number of obstacles, i.e., forest dislocations. If, on the other hand, the obstacles are impurity atoms, whose concentration remains constant during the deformation, then $\Delta\sigma_{\max}$ should not depend on the value of the flow stress (degree of deformation). In that case, however, the influence of the degree of deformation can be manifested through a dependence of the characteristic time t_c on the diffusion co-

efficient, which is proportional to the nonequilibrium concentration of vacancies formed in the plastic deformation process [see Eq. (6)].^{5,8} Hence it is important in principle in choosing a specific DSA model to obtain and analyze the experimental dependence on the flow stress (degree of deformation) for each parameter $\Delta\sigma_{\max}$ and t_c individually, and not for the total quantity $\Delta\sigma$. We note that such separate dependences have been obtained before only for In–Sn alloys, in a previous paper by the author.¹³

In In–Pb alloys the maximum value of the post-relaxation hardening increases in the initial stage of deformation (up to ~ 3 –5%), upon a transition from the elastic part to the stage of steady flow. At such deformations the post-relaxation yield point is not very clearly expressed, and the strong change of the hardening coefficient is indicative of a sharp change in the rate of plastic deformation, which makes it hard to interpret the results. At deformations of 5% and higher, $\Delta\sigma_{\max}$ either changes slowly or decreases (Fig. 8c), which is at odds with the model concepts.^{6–8} Such behavior of $\Delta\sigma_{\max}$ allows one to rule out forest dislocations as a possible type of obstacle whose strength changes during DSA and suggests impurity atoms instead. This is also suggested by an estimate, based on the value of the activation volume γ , of the density of obstacles that must be overcome by the dislocations in a thermally activated manner. For example, for the alloy with 8 at. % Pb at $T = 115$ K one has $\gamma \approx 10^{-20}$ cm³, from which we find that the density of obstacles is approximately equal to 10^{10} cm⁻², which is too large for the density of forest dislocations at the yield stress. The given value of the activation volume also suggests that the obstacles that change their characteristics during DSA are not individual impurity atoms but their complexes, as is characteristic for highly concentrated alloys. If the main obstacles were individual impurity atoms, then the value of the activation volume at the given concentrations of lead would be several orders of magnitude smaller.

The value of the characteristic time remains constant over a wide range of deformations, from 5% to 15%, as can be seen in Fig. 9; this indicates that nonequilibrium vacancies do not play an important role in the DSA process at such deformations.

Analysis of column 5 of Table I shows that the DSA kinetics is governed by the kinetics of the migration of impurity atoms toward the dislocations (dependence of ΔC on the aging time). The kinetics of the DSA process in In–Pb alloys is described by an equation of the Harper type [Eq. (1)], which at short times goes over to an equation of the Cottrell–Bilby type [Eq. (2)]. A feature of the results is that the power-law exponent in Eqs. (1) and (2) is not equal to 2/3, as would follow from the solution of the Cottrell–Bilby problem of the segregation of impurity atoms from the bulk of the crystal [see Eq. (7)], but is a smaller by a factor of two. The same feature was observed earlier by the author in In–Sn alloys¹³ and by other investigators in copper^{19–21} and aluminum^{22,23} alloys in experiments on the study of the dependence of the rate sensitivity of the flow stress on the value of that stress. The two-dimensional Cottrell–Bilby problem reduces to a one-dimensional problem if the diffusion of impurity atoms is of a pipe rather than a bulk

TABLE I. Models of dynamic strain aging.

Model No.	Authors	Type of obstacles	Model of DSA	Kinetic law $\Delta\sigma(t)$	$\Delta\sigma(\varepsilon)$ or $\Delta\sigma(\sigma)$
1.1	McCormick (1972) 4; Beukel (1975) 5, (1982) 8	Impurity atoms	Decrease of the mean distance between impurity atoms along the dislocation line at a fixed strength of the obstacles	Initial assumptions: 1. $\Delta\sigma \equiv \Delta\sigma_f \propto \Delta C$, 2. $\Delta C \propto c(Dt_w)^{2/3}$ (Cottrell–Bilby equation). Result: $\Delta\sigma \propto c(Dt_w)^{2/3}$	Determined by the dependence of the bulk diffusion coefficient on ε , $\Delta \propto \varepsilon^m$. Result: $\Delta\sigma \propto \varepsilon^{2m/3}$
1.2	Malygin (1982) 17	Impurity atoms	See model 1.1 (the kinetics of the process is considered for long aging times)	Initial assumptions: 1. $\Delta\sigma \equiv \Delta\sigma_f \propto \Delta C$, 2. $\Delta C = \Delta C_{\max}\{1 - \exp[-(t_w/t_c)^{2/3}]\}$ (Harper's equation) $\Delta C_{\max} = c \exp(W/kT)$, $t_c \propto (\Delta C_{\max}/c)^{3/2}/D$. Result: $\Delta\sigma = \Delta\sigma_{\max}\{1 - \exp[-(t_w/t_c)^{2/3}]\}$, where $\Delta\sigma_{\max} \approx \Delta C_{\max}W/b^3$	Determined by the dependence of the bulk diffusion coefficient on ε , $D \propto \varepsilon^m$. Result: $t_c \propto \varepsilon^{-m}$, $\Delta\sigma_{\max}$ is independent of ε
1.3	Neuhäuser, Flor (1978) 9	Clusters of several (~10) impurity atoms	Effective strength of the obstacles increases on account of a rearrangement of their atomic structure near the dislocation core	Initial assumptions: 1. $\delta\Delta G_0 \propto \Delta C^\alpha$, 2. $\Delta\sigma \propto \delta\Delta G_{0r} - \delta\Delta G_{0a}$, 3. $\Delta C \propto c(D_d t_w)^\beta$. Result: $\Delta\sigma \propto cD_d^\gamma [(\dot{\sigma}_{\text{dyn}}/\dot{\sigma})^\gamma - 1]$	Determined by the dependence of the pipe diffusion coefficient on ε
1.4	Schwarz (1982) 18	Isolated impurity atoms or groups of them	Strength of the obstacles increases at a fixed distance between them	Empirical expression inferred from measurements of the internal friction: $\Delta\sigma = \Delta\sigma_{\max}[1 - \exp(-t_w/t_c)]$, where $t_c = \nu_S \exp(-\Delta H/kT)$	t_c is independent of ε (in the case of pipe diffusion), $\Delta\sigma_{\max}$ is independent of ε
2.1	Sleeswyk (1958) 3; Mulford, Kocks (1979) 6; Wycliffe, Kocks, Embury (1980) 7	Forest dislocations	Strength of the obstacles increases owing to a redistribution (by pipe diffusion) of impurities near the points of intersection of mobile dislocations with forest dislocations	Initial assumptions: 1. $\Delta \ln K_d \propto \Delta C$, 2. $\Delta\sigma \equiv \Delta\sigma_d \propto \sigma_d \Delta C$, 3. $\Delta C \propto c(D_d t_w)^{2/3}$ (Cottrell–Bilby equation). Result: $\Delta\sigma \propto \sigma_d c(D_d t_w)^{2/3}$	$\Delta\sigma \propto \sigma_d \propto \sigma$ The relation is a consequence of the dependence of the dislocation flow stress σ_d on the density of the forest dislocations: $\sigma_d \propto \rho^{1/2}$
2.2	Springer, Schwink (1991) 19; Kalk, Schwink (1995) 20; Schwink, Nortmann (1997) 21	Forest dislocations	See model 2.1 (the one-dimensionality of the pipe diffusion is taken into account)	Initial assumptions: 1. $\Delta \ln K_d \propto \Delta C$, 2. $\Delta\sigma \equiv \Delta\sigma_d \propto \sigma_d \Delta C$, 3. $\Delta C \propto c(D_d t_w)^{1/3}$ (equation for two-dimensional diffusion). Result: $\Delta\sigma \propto \sigma_d c(D_d t_w)^{1/3}$	$\Delta\sigma \propto \sigma_d \propto \sigma$ The relation is a consequence of the dependence of the dislocation flow stress σ_d on the density of the forest dislocations: $\sigma_d \propto \rho^{1/2}$

Notes: σ is the flow stress; $\Delta\sigma$ is the DSA contribution to the flow stress; σ_f is the frictional stress (the contribution to the frictional stress due to the interaction of the dislocations with impurity atoms); $\Delta\sigma_f$ is the DSA contribution to the frictional stress; σ_d is the dislocation flow stress (the contribution to the flow stress due to the interaction of mobile and forest dislocations); $\Delta\sigma_d$ is the DSA contribution to the dislocation flow stress; t_w is the waiting time of a dislocation for thermal activation at an obstacle; ΔC is the change in concentration of the impurity atoms along the dislocation line; c is the atomic concentration of the solution; D is the bulk diffusion coefficient; D_d is the pipe diffusion coefficient; ε is the deformation; W is the binding energy of a dislocation and an impurity atom; $\delta\Delta G_0$ is the DSA-related change in the free enthalpy of activation; $\delta\Delta G_{0r}$ and $\delta\Delta G_{0a}$ are the DSA-related changes in the free enthalpy of activation in the stress relaxation regime and in the regime of active deformation, respectively; $(-\dot{\sigma}_{\text{dyn}})$ and $(-\dot{\sigma}_r)$ are the rates of change of the flow stress at the beginning and end of the stress relaxation; α , β , and γ are constants, with $\gamma = \alpha\beta \approx 0.5$, according to the data of Ref. 9; ΔH is the activation energy for pipe diffusion; ν_S is the attempt frequency; K_d is the effective strength of an obstacle.

nature.¹³ In that case the kinetics of the process can be described by Eqs. (1) and (2) with $n = 1/3$. The kinetic behavior of the value of the post-relaxation hardening found in this study may be an indication that pipe diffusion of impurity atoms is realized in In–Pb alloys.

The main parameter that determines the temperature region in which the DSA effect is manifested and the rate at which it occurs is the activation energy of the process. For

the alloys studied here the experimentally determined activation energy (0.3–0.34 eV) turned out to be a factor of 2 lower than the activation energy for the diffusion of Pb impurity atoms in In (~0.59 eV),²⁴ apparently because of the occurrence of DSA in the region of the dislocation core. This conjecture agrees with the established kinetics of post-relaxation hardening. The twofold decrease of the activation energy and the twofold lowering of the exponent in the

power law (1) as a result of the pipe diffusion make for a low temperature for the onset of DSA in In–Pb alloys ($\sim 0.17 T_m$).

Analysis of the regularities of the DSA effect on the basis of the modern models presented in Table I shows that the most probable mechanism for the DSA in In–Pb alloys is a local rearrangement of the structure of the obstacles in the stress field of the dislocations stopped in front of them. The obstacles for the moving dislocations are apparently complexes of impurity atoms. A rearrangement of the structure of the impurity complexes leading to an increase in their strength is facilitated by pipe diffusion along the dislocations. These ideas correspond to models 1.3 and 1.4 in Table I. However, there are important disagreements between our results and these models. For example, the kinetics of the DSA in In–Pb alloys differs from the first-order kinetics used in model 1.4. It also differs from the DSA kinetics observed in crystals of brasses,⁹ for which the exponent in the power law (2) is close to 0.5; the kinetics in the region of long relaxation times was not investigated in Ref. 9.

The temperature dependence of the maximum hardening obtained in the present study cannot be explained in the framework of the existing theoretical ideas. The $\Delta\sigma_{\max}(T)$ curve is only qualitatively described by the equations¹⁷

$$\Delta\sigma_{\max} = (W/b^3)\Delta C_{\max}, \quad (9)$$

$$\Delta C_{\max} = c \exp(W/kT), \quad (10)$$

where W is the binding energy of the dislocation to an impurity atom, and ΔC_{\max} is the maximum concentration of impurities on a dislocation. The quantitative discrepancy lies in the fact that when the value of the lead concentration in the alloy under consideration (e.g., $c = 0.08$) and the experimentally determined value of the binding energy of a dislocation with an impurity atom ($W = 0.057$ eV) are substituted into (10), one obtains $\Delta C_{\max} \gg 1$, which is absurd. If the one solves the inverse problem, i.e., that of determining the concentration of impurity atoms by starting from the experimental dependence $\Delta\sigma_{\max}(T)$ and Eqs. (8) and (9), then it comes out to be equal to 2.6×10^{-5} , which is about three orders of magnitude lower than the impurity concentration in the alloys studied.

The behavior of the characteristic time in the region of small and large degrees of deformation and at temperatures above 140 K remains unclear (Fig. 4). It is possible that the deviation of the experimental data from relation (5) is due to an intensification of DSA already in the stage of constant-rate deformation. There may be an effect due to annealing of nonequilibrium vacancies, as a result of which their concentration is lower than it should be at the degree of deformation achieved.¹¹ As the temperature is raised there is an increasing contribution to the DSA from bulk diffusion, which as a result of the higher activation energy occurs at a much slower rate than the pipe diffusion. On the whole, under conditions of a superposition of two DSA mechanisms, one of which is governed by pipe diffusion and the other by bulk diffusion^{5,18} (see also models 1.1 and 1.4 in Table I), the kinetics of the DSA will be governed by the slower process if the two processes give an additive contribution to the hardening of the crystal¹⁸ and the fast process is relatively rapidly exhausted.

Finally, the question of the physical meaning that can be attached to the activation energy ΔH determined from the $t_c(T)$ curve [see Eq. (5)]. According to model 1.4 and the ideas set forth above and in the author's previous paper,¹³ the characteristic time is uniquely determined by the diffusion coefficient, so that ΔH has the meaning of the activation energy for pipe diffusion. At the same time, according to other models (see model 1.2), the characteristic time depends not only on the diffusion coefficient but also on the maximum concentration of impurities on the dislocation. In that case, for calculating the activation energy for diffusion, one must use the relation $A(T)$. For In–Pb alloys the activation energy determined in this way is approximately equal to 0.1 eV in the temperature interval 115–130 K, which is too small for the energy of migration of the impurity atoms. A final clarification of all the questions touched on here will require further investigation. Apparently, both the current theoretical ideas and the DSA model are in need of further development.

CONCLUSIONS

1. The dependence of the post-relaxation hardening on the duration of the stress relaxation, rate of change of the stress at the end of the relaxation, temperature, impurity concentration, degree of deformation, and the value of the flow stress has been obtained for In–Pb alloys with 6 and 8 at. % Pb in the temperature interval 77–205 K.

2. It has been shown that the dependence of the post-relaxation hardening on the duration of the stress relaxation is described by an equation of the Harper type, which at short relaxation times goes over to an equation of the Cottrell–Bilby type. The exponent in the power law in these equations is equal to 1/3, which indicates that the diffusion of impurity atoms along the dislocations is of a pipe character.

3. For $T = 115$ – 125 K and deformations in the interval 5–15% the characteristic time is independent of the degree of deformation and lead concentration. The activation energy of the DSA process is estimated to be 0.34 eV. This quantity can be interpreted as the activation energy for pipe diffusion.

4. The maximum post-relaxation hardening is proportional to the lead concentration and reaches approximately an order of magnitude as the temperature is lowered from 205 to 115 K.

5. A comparison with the modern theories of the DSA suggests that in In–Pb alloys the main obstacles to the motion of dislocations with an interaction that varies in the course of the DSA are complexes of impurity atoms, and the DSA process itself reduces to a local rearrangement of the structure of the obstacles in the stress field of the dislocations stopped in front of them.

The author is grateful to S. V. Lubenets, V. D. Natsik, S. N. Smirnov, and L. V. Skibina for a discussion of the results of this study and for constructive criticism. This study was supported in part by the Swiss National Science Foundation.

*E-mail: fomenko@ilt.kharkov.ua

¹Single crystals of highly concentrated In–Pb alloys with an axis along the [100] direction cannot be grown by the Bridgman method in knock-down

graphite forms. As a result of twinning of the alloy at the neck between the seed and sample a reorientation of the [100] axis of the seed to the [001] axis of the sample occurs.

-
- ¹A. H. Cottrell, *Dislocations and Plastic Flow in Crystals* [Clarendon Press, Oxford (1953); Metallurgizdat, Moscow (1958)].
- ²J. Friedel, *Dislocations* [Pergamon Press, Oxford (1964); Mir, Moscow (1967)].
- ³A. W. Sleeswyk, *Acta Metall.* **6**, 598 (1958).
- ⁴P. G. McCormick, *Acta Metall.* **20**, 351 (1972).
- ⁵A. van den Beukel, *Phys. Status Solidi* **30**, 197 (1975).
- ⁶R. A. Mulford and U. F. Kocks, *Acta Metall.* **27**, 1125 (1979).
- ⁷P. Wycliffe, U. F. Kocks, and J. D. Embury, *Scr. Metall.* **14**, 1349 (1980).
- ⁸A. van den Beukel and U. F. Kocks, *Acta Metall.* **30**, 1027 (1982).
- ⁹H. Neuhäuser and H. Flor, *Scr. Metall.* **12**, 443 (1978); *Acta Metall.* **28**, 939 (1980).
- ¹⁰N. Zarubova, *Czech. J. Phys., Sect. A* **31**, 157 (1981).
- ¹¹A. van den Beukel, J. Blonk, and G. H. van Haastert, *Acta Metall.* **31**, 69 (1983).
- ¹²S. V. Lubenets and L. S. Fomenko, *Fiz. Met. Metalloved.* **61**, 971 (1986).
- ¹³S. V. Lubenets and L. S. Fomenko, *Fiz. Met. Metalloved.* **62**, 377 (1986).
- ¹⁴S. V. Lubenets, V. I. Startsev, and L. S. Fomenko, *Fiz. Met. Metalloved.* **39**, 410 (1975).
- ¹⁵V. Z. Bengus and S. N. Smirnov, *Mater. Sci. Eng.* **27**, 73 (1977).
- ¹⁶R. Bullough and R. Newman, *Rep. Prog. Phys.* **33**(2), 101 (1970).
- ¹⁷G. A. Malygin, *Phys. Status Solidi A* **72**, 493 (1982).
- ¹⁸R. B. Schwarz, *Scr. Metall.* **16**, 385 (1982).
- ¹⁹F. Springer and Ch. Schwink, *Scr. Metall.* **25**, 2739 (1991).
- ²⁰A. Kalk and Ch. Schwink, *Philos. Mag. A* **72**, 315 (1995).
- ²¹Ch. Schwink and A. Nortmann, *Mater. Sci. Eng., A* **234–236**, 1 (1997).
- ²²C. P. Ling and P. G. McCormick, *Acta Metall. Mater.* **41**, 3127 (1993).
- ²³S.-Y. Lee, Thesis, RWTH, Aachen (1993).
- ²⁴L. S. Fomenko, S. V. Lubenets, and V. I. Startsev, *Scr. Metall.* **18**, 535 (1984).

Translated by Steve Torstveit

LETTERS TO THE EDITOR

On the features of the polarization of the bielectronic absorption spectra of the cryocrystal δ -O₂

V. M. Loktev*

*N. N. Bogolyubov Institute of Theoretical Physics, National Academy of Sciences of Ukraine,
ul. Metrologicheskaya 14-b, 03143 Kiev, Ukraine*
(Submitted August 11, 2000)

Fiz. Nizk. Temp. **26**, 1256–1259 (December 2000)

The possible form of the absorption spectrum of the δ phase of oxygen in polarized light is analyzed by proceeding from the known crystal structure of this phase. © 2000 American Institute of Physics. [S1063-777X(00)01212-3]

1. The optical spectra of the equilibrium low-temperature α , β , and γ phases of solid oxygen have been studied long and presumably well both experimentally^{1–3} and theoretically^{4,5} (see also the collective monograph of Ref. 6). The most unusual and interesting of these have been the bimolecular electronic spectra of the antiferromagnetic α phase (having a monoclinic structure $C2/m$ and existing below $T_{\alpha\beta}=23.8$ K), which have revealed a rich polarized fine structure. This fine structure has been described qualitatively and quantitatively by proceeding from the concepts of Frenkel biexcitons — bound states of two molecular excitons or small-radius excitons. In α -O₂ the optical absorption lines corresponding to biexcitons are doublets and are polarized in its basal (i.e., ab) plane. Further development of the theory has shown that the characteristic doublet splitting also accompanies exciton–magnon absorption in α -O₂, even though it does not contain bound states of excitons and magnons.

In recent years spectroscopic technique has come to be used intensively (see Refs. 7–9) for studying the comparatively recently discovered high-pressure phases denoted by δ and ε , a description of which can be found in the review article by Freĭman.¹⁰ It is therefore of interest to examine the distinctive features of their optical spectrum. In this communication we examine the polarized properties of the δ phase, the structure of which has been reliably established.¹⁾

2. As was shown in Ref. 11 (see also Refs. 8 and 10), the application of pressure to α -O₂ affects mainly the intermolecular distances in the ab planes and causes an interplanar shear deformation. The growth of the latter as the pressure is increased leads to a structural transition from the monoclinic to the orthorhombic system $Fmmm$, which is a natural structure that is just the δ phase. Since the α phase is a two-sublattice collinear antiferromagnetic insulator with a finite interplane interaction of exchange origin, and this interaction is small because of the weakness of the monoclinic distortion in this phase,²⁾ it would seem that this interaction could only increase as the δ phase is approached. In such a case there is no need to assume *a priori* that the magnetic properties of the orthorhombic δ phase are quasi-two-dimensional, although the actual exchange parameters [in the basal planes

— for the nearest and next-nearest neighbors, and between the planes — for the nearest neighbors (see Fig. 1)] should undoubtedly reflect the existing spatial anisotropy of the lattice in this phase. Here, however, one can see no reason for the α -phase magnetic structure to change,³⁾ and it should be conserved, as is confirmed by experiment.⁸ In other words, we shall assume that the spins of the molecules are directed along the “former” monoclinic axis (without loss of generality, we denote this as the \mathbf{b} axis in δ -O₂, by analogy with the α phase).

3. Since the lowest ${}^1\Delta_g$ and ${}^1\Sigma_g^+$ states of the O₂ molecule are dipole and intercombination forbidden (and the first of these is also forbidden in the magnetic dipole approximation), the intensity of the absorption of all the condensed phases of oxygen is governed by bimolecular transitions, the effective dipole moment of which is given by the expression^{6,14}

$$\mathbf{P}_{\text{eff}}^{fg} = \frac{1}{2} \sum_{\mathbf{n}_\alpha, \mathbf{m}_\beta} \pi_{\mathbf{n}_\alpha \mathbf{m}_\beta}^{fg} B_{\mathbf{n}_\alpha}^+(f) B_{\mathbf{m}_\beta}^+(g) (1 - \delta_{\alpha\beta}), \quad (1)$$

where $\pi_{\mathbf{n}_\alpha \mathbf{m}_\beta}^{fg}$ is the effective dipole moment of the two-particle transition of molecules located at sites \mathbf{n} and \mathbf{m} and belonging to magnetic sublattices α and β , $B_{\mathbf{n}_\alpha}^+(f)$ is the creation operator for an electronic excitation f ($= {}^1\Delta_g, {}^1\Sigma_g^+$) on molecule \mathbf{n}_α (if $f=g$, then the dipole moment of the pair is nonzero only when the intramolecular vibration is taken into account⁶⁾). The presence of the Kronecker delta in Eq. (1) provides for the lifting (at $T=0$) of the intercombination forbiddenness for pairs of molecules from different magnetic sublattices.

In calculating the absorption spectra of α -O₂, in the sum (1) we previously took into account only the nearest neighbors from one ab plane, since for a light wave with polarization $\mathbf{E} \parallel [\mathbf{a} \times \mathbf{b}]$ the spectrum did not possess any polarization properties and was therefore insufficiently informative. The properties of the orthorhombic δ phase specifically require taking interplane pairs of molecules (including from different magnetic sublattices) into account in (1) in addition to the intraplane pairs. This, in turn, entails the appearance of two types of interacting molecules and, consequently, the

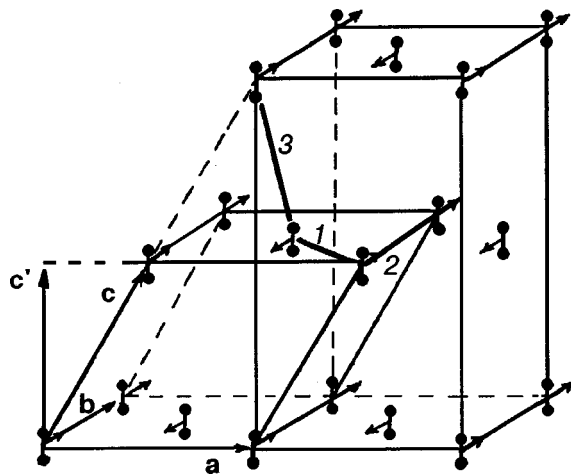


FIG. 1. Unit cells: the monoclinic cell with two molecules and the orthorhombic with four molecules — the magnetically ordered δ -O₂. The numbers label the neighbors from the same (1 and 2) and nearest (3) basal planes; the arrows indicate the direction of the spins of the O₂ molecules. Neighbors of the types 1 and 3, as representatives of the dipole active pairs (including the nearest molecules from different magnetic sublattices) are connected by heavy lines. In the monoclinic cell of δ -O₂ (unlike α -O₂) the relation $|c'| = (c^2 - a^2/4)^{1/2}$ holds.

possibility of the appearance of two bimolecular bound states, differing by the binding energy in the pair. The excitonic character of the “partial” single-particle excitations leads to an additional — biexcitonic^{4,15} — splitting of the two-particle absorption lines, which become polarized along the principal axes of the lattice. The value of the splitting for both bound and dissociated (e.g., exciton–magnon) states is determined completely by the widths of the exciton bands (and by the anisotropy of the magnon bands); see Ref. 6. We recall that in magnetic antiferroelectrics the electronic excitation moves in such a way that it does not leave the sublattice in which it arose.^{6,14}

4. Because there are three principal axes (**a**, **b**, and **c'**) in the δ phase, it would seem that there should also be three absorption lines, as is observed in body-centered lattices.¹⁵ However, δ -O₂ is a face-centered structure, and therefore it is clear even without a calculation that the number of biexcitonic lines should in principle equal four — two each for the *ab* and *ac'* planes (see Fig. 1). In fact, one can easily see that in the polarization $\mathbf{E} \parallel \mathbf{a}$ there will be one (intraplane) biexciton excited, with wave vector $\mathbf{Q} \approx 0$, in the polarization $\mathbf{E} \parallel \mathbf{c}'$ there will be a different one (interplane), and in the polarization $\mathbf{E} \parallel \mathbf{b}$ there will be both of these (see Fig. 2). The total energy of each of the doublets will, of course, be different, for it is determined by the relative values of the vectors $\pi_{n\alpha m\beta}^{fg}$ for the neighbors from the same and different planes, while the component in each doublet will be determined by the ratios $(\mathbf{a} + \mathbf{b})^2 / (\mathbf{a} - \mathbf{b})^2$ and $(\mathbf{b} + \mathbf{c}')^2 / (\mathbf{b} - \mathbf{c}')^2$, if $|c'|$ is understood to mean the interplane distance (see Fig. 1). As to the biexcitonic splitting, it should, generally speaking, be the same, since for both biexcitonic doublets it is determined by the widths of the one-exciton bands. This does not apply to the dissociated states, the doublet splitting of the polarized bands of which, as we have said, includes anisotropy of the magnon bands and, hence, can be somewhat different in the doublets. A systematic examination of

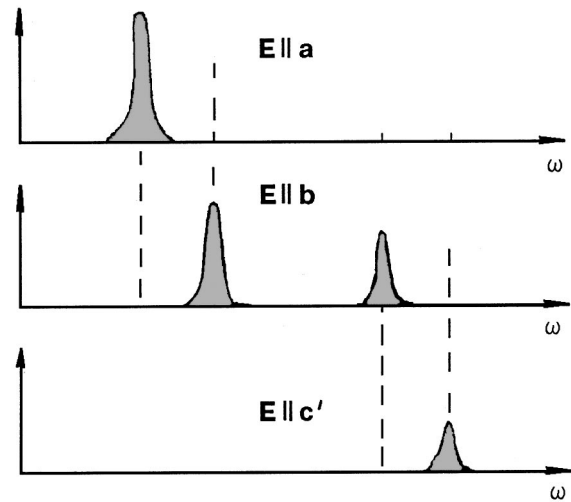


FIG. 2. Qualitative form of the biexcitonic absorption spectrum of the δ phase in the field \mathbf{E} of a light wave of frequency ω .

the form of the single- and biexcitonic absorption spectra of δ -O₂ will be done in a separate paper. We note only that the experimental study of single crystals of the δ phase of oxygen in polarized light would make it possible not only to check the concepts stated above but, more importantly, to determine the parameters of the exchange and resonant interactions for this phase and to refine the spectrum of the α phase in the polarization $\mathbf{E} \parallel [\mathbf{a} \times \mathbf{b}]$.

The author expresses his sincere gratitude to H-J. Jodl for calling his attention to this problem and to A. P. Brodyanskiĭ, L. Ulivi, M. Santoro, and Yu. A. Freĭman for a helpful discussion of the structure of the crystalline phases of oxygen and the transformation of its optical absorption spectra under external pressure. The author would also like to thank Prof. A. Jezowski for the financial support that enabled him to participate in the CC-2000 Conference, where the spectra of the δ phase in unpolarized light were presented.

*E-mail: vloktev@bitp.kiev.ua

¹For ε -O₂ the situation is not yet completely clear. Its structure is considered to be monoclinic (*A2/m*), but the point symmetry and orientation of the molecules has not yet been established. In this regard it can be noted that there has as yet been no investigation of the possibility that the role of the quadrupole component of the intermolecular interaction $\sim Q^2/r^5$ (Q is the wave vector, and a is the interatomic distance) in solid O₂ increases on compression. At small distances r it can be comparable to or even greater than the exchange interaction $\sim J \exp(r/a)/r$, and that would inevitably cause rotations of the molecules. Of course, we are talking only about a tendency, since the approach of the molecules due to the external pressure degrades the applicability of the multipole expansion for describing the intermolecular interaction. Even when this is taken into account, however, the very old hypothesis of Ellis and Kneser (see Ref. 6; this hypothesis has been newly resurrected in Ref. 8) that stable O₄ complexes are formed does not yet seem convincing and sufficiently well founded. Moreover, in a crystal one should speak of a spin–Peierls transition.

²Here it is appropos to note that as one follows the line of transitions $\beta \rightarrow \alpha \rightarrow \delta$, the rhombohedral β phase is actually quasi-two-dimensional, but not so much because of the relative smallness of the interplane exchange between O₂ molecules as because of the crystalline and magnetic structure of β -O₂, which is such that the main contributions to the interplane interaction (i.e., the exchange field) from different molecules completely compensate one another. Thus on average the planes are exchange “free,” or frustrated.¹² The frustration is lifted only by weak interactions.¹³ In the α phases a two-sublattice structure arises on account of the decompensation of the exchanges from different neighbors, which in

the monoclinic structure become inequivalent. The formation of three sublattices in β -O₂ is in essence a trivial solution of the “frustration problem” for each of the ab planes. However, for the Ising model on a planar triangular lattice, for example, this can no longer happen.

³⁾At the same time, because of the higher symmetry of the lattice in the orthorhombic phase as compared to the monoclinic phase, one of the spin invariants becomes forbidden ($S^x S^y$ for the choice of axes $X||\mathbf{a}$, $Z||\mathbf{b}$); in the α phase this can easily be taken into account by a simple rotation of the coordinate system or, equivalently, a renormalization of the one-molecule (and intermolecule) anisotropy constants.

¹A. F. Prikhot'ko, T. P. Ptukha, and L. I. Shanskiĭ, *Ukr. Fiz. Zh.* **12**, 1166 (1966).

²V. V. Eremenko, Yu. G. Litvinenko, and T. I. Garber, *Phys. Status Solidi B* **30**, 49 (1968).

³Yu. G. Litvinenko, V. V. Eremenko, and T. I. Garber, *Ukr. Fiz. Zh.* **14**, 326 (1969).

⁴Yu. B. Gaididei and V. M. Loktev, *Phys. Lett. A* **44**, 409 (1975).

⁵Yu. B. Gaididei, V. M. Loktev, A. F. Prikhotko, and L. I. Shanskiĭ, *Phys. Status Solidi B* **72**, 795 (1975); *ibid.* **73**, 415 (1976).

⁶V. I. Verkin, and A. F. Prikhot'ko (Eds.), *Cryocrystals* [in Russian], Naukova Dumka, Kiev (1983).

⁷H.-J. Jodl, *Abstracts of Third International Conference on Cryocrystals and Quantum Crystals*, Szklarska Poreba, Poland, July 28-August 4, 2000, p. 30.

⁸F. A. Gorelli, N. Santoro, L. Ulivi, and R. Bini, *Phys. Rev. B* **60**, 6179 (1999); *Phys. Rev. Lett.* **83**, 4093 (1999).

⁹S. Medvedev, A. P. Brodyanski, Y.-J. Jodl, M. Santoro, and F. A. Gorelli, *Abstracts of Third International Conference on Cryocrystals and Quantum Crystals*, Szklarska Poreba, Poland, July 28–August 4, 2000, p. 113.

¹⁰Yu. A. Freĭman, *Fiz. Nizk. Temp.* **16**, 955 (1990) [*Sov. J. Low Temp. Phys.* **16**, 559 (1990)].

¹¹S. Desgreniers, Y. K. Vhora, and A. L. Ruoff, *J. Chem. Phys.* **94**, 1117 (1990).

¹²V. M. Loktev, *Fiz. Nizk. Temp.* **5**, 295 (1979) [*Sov. J. Low Temp. Phys.* **5**, 142 (1979)].

¹³I. M. Vitebskiĭ, V. M. Loktev, V. L. Sobolev, and A. A. Chabanov, *Fiz. Nizk. Temp.* **18**, 1044 (1992) [*Low Temp. Phys.* **18**, 733 (1992)]; *Fiz. Nizk. Temp.* **19**, 151 (1993) [*Low Temp. Phys.* **19**, 107 (1993)].

¹⁴É. G. Petrov, *Theory of Magnetic Excitons* [in Russian], Naukova Dumka, Kiev (1976).

¹⁵Yu. B. Gaididei and V. M. Loktev, *Phys. Status Solidi B* **62**, 709 (1974).

Translated by Steve Torstveit